1-1-2015

Mechanisms Controlling Friction and Adhesion at the Atomic Length-Scale

Xin Zhou Liu
University of Pennsylvania, xinzliu@seas.upenn.edu

Mechanisms Controlling Friction and Adhesion at the Atomic Length-Scale

Abstract
A lack of understanding of the fundamental mechanisms governing atomic-scale adhesion and friction creates ongoing challenges as technologically-relevant devices are miniaturized. One major class of failure mechanisms of such devices results from high friction, adhesion, and wear. This thesis presents investigations into methods by which atomic-scale friction and adhesion can be controlled. Using atomic force microscopy (AFM), friction and adhesion properties of graphene were examined. While friction between the tip and graphene depends on thickness, as explained by the â??puckering effectâ??, adhesion is independent of the thickness when measured conventionally. However, adhesion is transiently higher when measured after the tip has slid over the graphene. This effect is caused by increased adhesiveness between graphene and tip due to aging. Second, chemical modification of graphene, specifically fluorination, affects friction strongly, with friction monotonically increases with increasing degree of fluorination. As supported by molecular dynamics (MD) simulations, this dependence is attributed to the fact that attachment of fluorine to graphene greatly enhances the local energy barrier for sliding, thereby significantly altering the energy landscape experienced by the tip. Finally, through matched AFM and MD, the speed dependence of atomic friction was explored within the framework of the Prandtl-Tomlinson model with thermal activation (PTT). For the first time, experiments and simulations are performed at overlapping scanning speeds. While friction was found to increase with the log of speed in both AFM and MD, consistent with the PTT model, friction in experiments was larger than in MD. Analysis revealed that the discrepancy was largely attributable to the differences in contact area and tip masses used in experiments vs. in simulation. Accounting for the overall influence of the two with the presence of instrument noise fully resolves the discrepancy. Through those novel studies and findings, it has been demonstrated that atomic-scale friction and adhesion can be controlled and understood, assisting the development of applications where variable or constant friction and adhesion are desired.

Degree Type
Dissertation

Degree Name
Doctor of Philosophy (PhD)

Graduate Group
Mechanical Engineering & Applied Mechanics

First Advisor
Robert W. Carpick

Keywords
adhesion, contact mechanics, friction, graphene, speed dependence, two-dimensional materials

Subject Categories
Mechanical Engineering | Nanoscience and Nanotechnology

MECHANISMS CONTROLLING FRICTION AND ADHESION AT THE ATOMIC LENGTH-SCALE

Xin Zhou Liu

A DISSERTATION

in

Mechanical Engineering and Applied Mechanics

Presented to the Faculties of the University of Pennsylvania

in

Partial Fulfillment of the Requirements for the

Degree of Doctor of Philosophy

2015

Supervisor of Dissertation

_____

Robert W. Carpick

Professor and Chair, Mechanical Engineering and Applied Mechanics

Graduate Group Chairperson

_____

Prashant Purohit, Associate Professor, Mechanical Engineering and Applied Mechanics

Dissertation Committee

Kevin T. Turner, Associate Professor, Mechanical Engineering and Applied Mechanics

Robert W. Carpick, Professor and Chair, Mechanical Engineering and Applied Mechanics

Vivek B. Shenoy, Professor, Materials Science and Engineering

MECHANISMS CONTROLLING FRICTION AND ADHESION AT THE ATOMIC LENGTH-SCALE

To my beloved wife, my parents, and my grandmother.

ACKNOWLEDGMENTS

This thesis represents the work I performed in my more than five years at Penn. In that time I have learned from and worked with many memorable individuals. I have spent long hours and days in the laboratory, which was more than just a second home for me. And I enjoyed it. With the completion of the thesis, I am glad to take this opportunity to acknowledge people who have made the thesis and my research possible.

First and foremost I must thank my advisor, Professor Rob Carpick, for his tremendous support, guidance, and mentorship for my research and during my graduate studies. His positivity and words of encouragement kept me motivated in difficult times; and his enthusiasm and curiosity for science made my times of success more joyful.

I would also like to thank Professor Kevin Turner and Professor Vivek Shenoy for serving on my PhD dissertation committee, and for challenging me during the PhD proposal exam and the final PhD defense. I would also like to thank my qualifying exam committee members, Professor Paulo Arratia and Professor Pedro Ponte Castañeda, for their time and help during my qualifying exam.

I am grateful to my collaborators for their useful discussions, Dr. Jeremy Robinson and Dr. Paul Sheehan at the U.S. Naval Research Laboratory; Dr. Sang-Pil Kim and Professor Vivek Shenoy at Penn and Brown University; Justin Ye and Professor Ashlie Martini at the University of California Merced; and Professor Yalin Dong at the University of Akron.

Many former and current group members have contributed to the work described in this thesis. Particularly, I thank Professor Philip Egberts, Professor Qunyang Li, Dr.

Prathima Nalam, Dr. Nitya Gosvami, Dr. Vahid Vahdat, Professor Tevis Jacobs, and Dr. Graham Wabiszewski for helpful, useful, and interesting discussions. I would also like to specially thank Professor Philip Egberts for his help with editing my thesis, and Dr. Prathima Nalam and Dr. Rodrigo Bernal for their valuable comments on my scientific presentations. I thank Zac Milne and Joel Lefever for his help with using the TEM. I thank Qizhan Tam and James Hilbert for their help with MATLAB coding. I also specially thank Qizhan Tam for his help with LabVIEW coding and machining of the D-LFC fixture. I thank Kaiwen Tian for his interesting scientific discussions.

I would like to take the opportunity to thank the technical staff in the Department of Mechanical Engineering and Applied Mechanics for their help of machining hardware pieces for our instrument, Peter Szczesniak, Peter Rockett, Joe Valdez, and Terry Kientz. I would also like to specially thank Peter Rockett for his great insights and promptness in helping me.

I would also like to take the opportunity to thank the administrative staff in the Department of Mechanical Engineering and Applied Mechanics for their help with administrative requirements during my graduate studies, including Maryeileen Banford Griffith, Sue Waddington-Pilder, Olivia Brubaker, Desirae Cesar, Nora Powell, and Peter Litt. I would also like to thank Betty Gentner, Coordinator for Academic Affairs in the School of Engineering and Applied Science, for her help my paperwork.

Use of the University of Pennsylvania Nano/Bio Interface instrumentation is acknowledged. Use of the facilities of the Pennsylvania Regional Nanotechnology Facility is acknowledged.

Finally, funding from the U.S. National Science Foundation under NSF/MRSEC DMR-1120901, NSF/ENG CMMI-1068741, and CMMI-1401164 is gratefully acknowledged.

ABSTRACT

MECHANISMS CONTROLLING FRICTION AND ADHESION AT THE ATOMIC LENGTH-SCALE

Xin Z. Liu

Professor Robert W. Carpick

A lack of understanding of the fundamental mechanisms governing atomic-scale adhesion and friction creates ongoing challenges as technologically-relevant devices are miniaturized. One major class of failure mechanisms of such devices results from high friction, adhesion, and wear. This thesis presents investigations into methods by which atomic-scale friction and adhesion can be controlled. Using atomic force microscopy (AFM), friction and adhesion properties of graphene were examined. While friction between the tip and graphene depends on thickness, as explained by the "puckering effect", adhesion is independent of the thickness when measured conventionally. However, adhesion is transiently higher when measured after the tip has slid over the graphene. This effect is caused by increased adhesiveness between graphene and tip due to aging. Second, chemical modification of graphene, specifically fluorination, affects friction strongly, with friction monotonically increases with increasing degree of fluorination. As supported by molecular dynamics (MD) simulations, this dependence is attributed to the fact that attachment of fluorine to graphene greatly enhances the local energy barrier for sliding, thereby significantly altering the energy landscape experienced by the tip. Finally, through matched AFM and MD, the speed dependence of atomic

friction was explored within the framework of the Prandtl-Tomlinson model with thermal activation (PTT). For the first time, experiments and simulations are performed at overlapping scanning speeds. While friction was found to increase with the log of speed in both AFM and MD, consistent with the PTT model, friction in experiments was larger than in MD. Analysis revealed that the discrepancy was largely attributable to the differences in contact area and tip masses used in experiments *vs.* in simulation. Accounting for the overall influence of the two with the presence of instrument noise fully resolves the discrepancy. Through those novel studies and findings, it has been demonstrated that atomic-scale friction and adhesion can be controlled and understood, assisting the development of applications where variable or constant friction and adhesion are desired.

TABLE OF CONTENTS

ACKNOWLEDGMENTS ..... **IV**

ABSTRACT ..... **VII**

LIST OF ILLUSTRATIONS ..... **XII**

CHAPTER 1: INTRODUCTION AND IMPORTANT OF TRIBOLOGY **1**

References **5**

CHAPTER 2: FRICTION AND ADHESION: A REVIEW **7**

2.1.1: Introduction to Friction **7**
2.1.2: Microscopic Single-Asperity Friction 9
2.1.3: Atomic-Scale Stick-Slip Friction 11

2.2: Review of Adhesion Phenomena **16**

2.3: Brief Discussion on Computer Simulations in Tribology **18**

2.4: References **21**

CHAPTER 3: EXPERIMENTAL TECHNIQUES AND SETUP **25**
3.1.1: Atomic Force Microscopy 25
3.1.2: AFM Friction Force Microscopy: Atomic Stick-Slip and Contact Stiffness 28
3.1.3: Brief Overview of AFM Instrumentation Used 32

3.2: Force Distance Spectroscopy **35**

3.3: Force Calibration of AFM Cantilevers **39**
3.3.1: Normal Force Calibration 40
3.3.2: Lateral Force Calibration 42

3.4: Raman Spectroscopy **46**

3.5: TEM for Examining the AFM Tip Shape and Tip Radius **49**

3.6: References **52**

CHAPTER 4: ADHESION PROPERTIES OF FEW-LAYER GRAPHENE: THE EFFECT OF SLIDING HISTORY ON ADHESION **55**

4.1: Introduction and Prior Studies on Graphene Surface Energy and Adhesion 55

4.2: Experimental Details.....59
4.2.1: Sample Preparation 59
4.2.2: Experimental Protocol 61

4.3: FEM Simulations.....63

4.4: Results 64
4.4.1: Direct Pull-Off Measurements 64
4.4.2: Pre-sliding Pull-Off Measurements 68
4.4.3: FEM Simulations 73

4.5: Discussion.....75

4.6: Summary.....82

4.7: References.....84

CHAPTER 5: FLUORINATION OF GRAPHENE ENHANCES FRICTION DUE TO INCREASED CORRUGATION 88

5.1: Introduction to Graphene and Fluorinated Graphene 88

5.2 Experimental Details.....92
5.2.2: Sample Preparation 92
5.2.1: Experimental Protocol 93

5.3: MD Simulation Protocol.....94

5.4: Results.....95
5.4.1: Optical Properties 95
5.4.2: Raman Spectroscopic Properties on Graphene and FG.....96
5.4.3: Frictional Properties on Graphene and FG.....97
5.4.3: MD Simulation Results.....100

5.5: Discussion.....101

5.6: Summary.....106

5.7: References.....106

CHAPTER 6: THERMALLY-ACTIVATED ATOMIC-SCALE FRICTION 111

6.1: Introduction.....111

6.2: Speed Dependence of Friction.....114
6.2.1: Experimental Details.....116
6.2.2: MD Simulations Protocol 125
6.2.3: Experimental Results 127
6.2.4: MD Simulations Results 134

6.2.5: Discussion 136

6.3: Temperature Dependence of Friction 144
6.3.1: Experimental Details 145
6.3.2: MD Simulations Protocol 147
6.3.3: Results and Discussion 147

6.4: Summary 153

6.5: References 156

CHAPTER 7: CONCLUDING REMARKS AND FUTURE WORK 161

7.1: Adhesion Properties of Graphene and Other 2-D Films 161

7.2: Friction Properties of Fluorinated Graphene and the Influence of Other Chemical Functionalization 165

7.3: Thermally-Activated of Atomic-Scale Friction 167

7.4: Overall Outlook 172

7.5: References 173

LIST OF ILLUSTRATIONS

Figure 2.1: Schematics of sliding contacts at three different length scales: macro-, micro-, and nanoscale. At the macroscale, two surfaces are seemingly flat; at the microscale, the contact consists of multi-asperities; at the nanoscale, single-asperity contact can be revealed. A_r denotes the real contact area.

Figure 2.2: First atomic stick-slip friction data acquired with a tungsten tip on a graphite surface. (a) A characteristic saw-tooth pattern can be resolved, where the period of the pattern corresponds to the graphite lattice. (b) A regular pattern indicating the graphite lattice can be resolved.

Figure 2.3: Cartoon showing atomic stick-slip motion for an AFM tip with an amorphous tip apex sliding across a crystalline surface. Red arrows indicate the sliding direction. From (a) to (c), the torsion of the cantilever is increasing while the tip apex is stuck at one position corresponding to the potential minimum. When the elastic strain in the cantilever reaches a critical magnitude, the tip apex will overcome the potential minimum, and thus the strain is quickly released by slipping quickly to the next position, as drawn in (d). This process repeats itself and the recorded lateral signal will produce a regular saw-tooth pattern, where the period of the pattern corresponds to the lattice spacing of the crystal.

Figure 2.4: A 1-D representation of Tomlinson model. A monatomic tip (blue) scans over a fixed chain of atoms (grey). The tip is attached to a slider support (black rectangle) through an elastic spring having a stiffness k. The forces on the tip atom are $F_{\text{tip-sample}}$, arising from the interaction of the tip and sample and F_{elastic}, arising from the movement of the base.

Figure 2.5: 1-D schematic of the FK model in which the tip atoms are connected by springs, having a force constant k, with their direct neighbors. They interact with each other while experiencing the surface potential. Pulling on the chain will build an elastic stress in the springs (sticking) and eventually cause the atoms to move up the side of the potential well and quickly slide down to the next bottom simultaneously (slipping).

Figure 3.1: (a) Schematic setup of an AFM. A rectangular microfabricated cantilever scans across the sample surface; the cantilever deflection is recorded by a laser beam that is reflected from the backside of the cantilever to the four-quadrant photo-sensitive diode (PSD). (b) A representative TEM image of an unused contact-mode silicon tip. In the center, the silicon lattice is resolved, revealing the crystalline structure which is covered by a native, amorphous silicon oxide layer of a few nanometers thickness. The red dash circle was fit to estimate the tip radius of ~4-5 nm in this case. (c) A PSD is used to simultaneously monitor the normal and torsional motion of the cantilever. Detection of forces is through the laser displacement: normal displacement of the laser corresponds to the cantilever bending normal to the surface due to normal forces; lateral displacement of the laser is due the cantilever twisting in response to lateral/friction forces.

Figure 3.2: (a) A typical friction force image from a Si tip scanned over an area consisting of two materials, graphene on A and SiO_2 on B, which exhibit distinct frictional behaviors. The image is constructed from a 512×512 matrix of sampled points. Lower brightness corresponds to lower friction. (b) A typical friction loop taken from the red dash line in (a). Black arrows indicate the scan direction. Due to hysteresis, the forward and backward scans form a friction loop. Clearly, the gap of the loop at A is smaller than that at B. (c) A friction force image of a Si tip on clean muscovite mica surface, resolving an atomic stick-slip pattern. Three-fold symmetry can be observed from the image, which matches the symmetry and spacing of the sample's lattice. (d) A representative friction loop, where stick-slip pattern can be seen. The slope of the sticking phase corresponds to the total lateral stiffness k_{tot}.

Figure 3.3: The work presented in this thesis is performed with four different AFM's. (a) Veeco Multimode AFM, (b) Asylum MFP-3D, (c) RHK 350 AFM, and (d) RHK 750 AFM.
Figure 3.4: A typical force distance (FD) curve. Dark blue arrows indicate the direction of the AFM tip motion. The tip approaches the sample surface from a large tip-sample separation distance (out-of-contact state, curve part 1), and after the snap-in, the tip presses on the sample (in-contact state) while it pushes on the sample (curve part 2). This completes the approach part of the curve, plotted in green. After the approach, the tip retracts from the surface (curve part 3), and the tip remains in contact with the surface until the pull-off event occurs (curve part 4), and separates from the sample (curve part 5), plotted in black.
Figure 3.5: A typical FD curve measured in a direct pull-off measurement on graphite. The blue arrow indicates the magnitude of the pull-off force; the green arrow indicates the pull-off event. The pull-off force measured in this graph corresponds to ~18 nN.
Figure 3.6: Schematic view of the D-LFC setup. Note here the design of the AFM. During the calibration, the AFM tip and the PG sheet are moving together with respect to the magnets.
Figure 3.7: Left: Schematic view of the holder for the D-LFC setup specially designed to ensure compatibility with the RHK AFM's. Right: Optical image of the setup mounted into a RHK specimen holder inside the RHK AFM.
Figure 3.8: Two types of inelastic electron scattering. Left: the final scattered state has a higher energy than the initial state (Stokes scattering); Right: the final state has a lower energy state (anti-Stokes scattering).
Figure 3.9: (a) Vibrational modes of carbon atoms (black spheres) in a graphene/graphite network. The case on the left corresponds to E_{2g} mode, or the 'stretching mode'; and the right case represents the A_{1g} mode, or the 'breathing mode'. (b) A typical Raman spectrum on a single-layer graphene, with the G and 2D peaks at ~1580 cm^{-1} and ~2700 cm^{-1}.
Figure 3.10: Results from Raman spectroscopy presented in the thesis are acquired with a NT-MDT Integra Raman spectrometer. The key components of the spectrometer are indicated, from left to right: upright microscope, inverted microscope allowing for bottom illumination of the Raman laser, and finally the spectrum analyzer. The entire spectrometer is resting on an air table to reduce mechanical noise when the sample is moved with respect to the laser beam for recording a Raman map.
Figure 3.11: (a) Tip profile of a Si AFM tip; the probe chip (not shown) is located beyond the far left of the image. (b) A zoomed-in image of the tip shank. The typical fringes are due to the variation in the thickness of the shank. (c) A high-resolution TEM image of the tip apex where Si crystal lattice can be resolved. The tip is terminated by a thin amorphous silicon oxide layer.
Figure 3.12: The JEOL 2100 high-resolution TEM that was employed to investigate AFM tips.
Figure 4.1: (a) Graphene friction *vs.* layer numbers. The magnitude of the forces is normalized to the value for the thinnest layer. (b) and (c) The proposed puckering effect. As the AFM tip slides over the graphene membrane (direction indicated by the green arrows), due to the low bending stiffness of thin graphene (b), the graphene deforms elastically in the out-of-plane due to shear and adhesion forces, resulting in an increased contact area in front of the tip (indicated by the color scale, red being the highest deflection height and blue the lowest).
Figure 4.2: Mechanical exfoliation method is used to prepare graphene samples. (a) Optical image of a typical graphene flake prepared this way. (b) A typical Raman map of the G band, and (c) AFM topography image of the same flake. Layer numbers are determined based on AFM topography and Raman topography images, and are indicated here by 1L, 2L etc. Single-layer graphene has a thickness of ~0.34 nm.
Figure 4.3: Normalized pull-off forces plotted versus measurement number on FLG with 1 to 5 layers, acquired using direct pull-off measurements. The measured pull-off forces have been normalized to their mean values in each set of connected data points. Normalized pull-off forces

plotted versus FD curve measurement number for (b) freshly-cleaved and (c) aged graphite, respectively. In (b) and (c) the same tip was used. However, each "set" refers to pull-off forces measured in different regions of interest on the same sample. A gray dashed line indicates the mean value in each case.

Figure 4.4: (a) Normalized pull-off forces versus number of layers of graphene. The same tip was used within one test, and a single area investigated for each bar plotted. The number of layers was varied with a random order. Different tips and FLG samples were used in the three tests. Each test on graphite was performed on an N_2-aged sample, using the same tip used for the other FLG samples indicated for that test. Error bars represent the standard deviation in the mean value of the normalized pull-off force for each FLG or graphite sample (a few tens of measurements acquired for each). (b) Normalized pull-off forces versus number of layers of graphene, measured in ambient air. The same tip was throughout the entire measurement. The number of layers was varied in random order. Error bars represent the standard deviation in the mean value of the normalized pull-off force for each FLG (~100 measurements acquired for each).

Figure 4.5: (a) Normalized pull-off forces *vs*. measurement number on FLG with 1 to 5 layers, acquired using the pre-sliding methodology. The pull-off forces of the each set (connected with a solid line) have been normalized to the mean values of that particular set (represented by a grey dashed line). The measurements on graphene come from a single sample and have all been conducted using the same tip. The same pre-sliding measurement carried out on (b) freshly-cleaved graphite and (c) aged graphite. In (b) and (c) the same tip has been used in both "sets", but measurements have been performed on different regions of interest that are far away from each other. The pull-off forces have been normalized to the mean value of the dataset (black dashed line).

Figure 4.6: Mean pull-off forces of the first data point of all dataset of pull-off force measurements collected, normalized beforehand in a manner described earlier. The mean values for each FLG layer number and for aged graphite was calculated from over 100 measurements of an increased pull-off force during pre-sliding measurements. Error bars represent the standard deviation obtained from averaging the first data points for each layer number.

Figure 4.7: (a) Normalized pre-sliding pull-off forces measured on graphene on muscovite mica. Clearly, overall the pull-off force stays rather constant and no sliding-history dependence is observed due to the stronger graphene-mica adhesion. Notice the 1 layer graphene shows an extremely low variation. (b) Normalized pre-sliding pull-off forces measured on a bare muscovite mica substrate. No sliding-history dependence is observed in any of these cases.

Figure 4.8: (a) FEM simulation results for normalized pull-off forces for interaction rations of w_{tip-gr}/w_{gr-sub} =1.2 (green) and 2.0 (red) using direct pull-off measurements and with pre-sliding. The direct pull-off force is the same as that with pre-sliding for an interaction ratio of 1.2, whereas an interaction ratio of 2.0 results in an increase of ~9% compared to direct pull-off. (b) and (c) show excerpts from simulations with interaction ratio 1.2 for direct pull-off and with pre-sliding, respectively. The same for (d) and (e) is shown but with interaction ratio 2.0.

Figure 4.9: A schematic view of the pre-sliding pull-off measurement. The bold, green arrows indicate the direction of the tip motion. The red line represents the top graphene layer that is aged and thus can delaminate due to its enhanced interaction with the tip. (a) The AFM tip makes initial contact with the graphene sheet prior to reciprocating over that local area. (b) While scanning in a reciprocating motion, a small, asymmetric pucker gradually develops due to adhesion and friction between the sample and the tip. (c) At the end of the sliding cycles, the tip retracts. Due to the strengthened tip-graphene interaction, the interfacial configuration has changed such that the top layer locally delaminates. This enhances the pull-off force. (d) After retraction, the graphene sheet relaxes and returns to the undeformed state.

Figure 5.1: Atomic structures of (a) graphene, (b) partially fluorinated graphene, and (c) fully fluorinated graphene. Black spheres represent carbon atoms and green spheres represent fluorine atoms. Note the hexagonal structure of graphene is retained after fluorination, although the perfectly planar structure is lost due to the different bonding properties between C-C bonds and C-F bonds, resulting in out-of-plane deformation. Note that the structures illustrated here only represent ordered fluorination.

Figure 5.2: Sample preparation steps: (a)-(c) CVD graphene grown on Cu foil and transferred onto SiO_2/Si substrate. (d) PMMA mask was locally patterned. (e) Graphene on SiO_2/Si was selectively etched by XeF_2 gas; (f) after lift-off, pristine and fluorinated graphene were obtained side-by-side on substrate.

Figure 5.3: Two snapshots of MD simulations during tip sliding from left to right. The red arrows indicate the scan direction. The black arrows indicate the direction of the normal load. (a) C_4F and (b) pristine graphene.

Figure 5.4: (a) Optical image of graphene and FG after 10 minute XeF_2 exposure. Small purplish islands are multi-layer fluorinated graphene regions. (b) Optical image of graphene and FG after 1 minute XeF_2 exposure. Blue boxes are drawn to better indicate the graphene-FG boundary.

Figure 5.5: (a) Raman D peak map of the area indicated with red box (iii) in Figure 5.3 (b). (b) Raman spectra of graphene with various degrees of fluorination. For pristine graphene (black spectrum), the ratio between the 2D and G peak intensities indicates that the region consists of a single layer graphene. As soon as the fluorination begins, a clear D peak appears, signifying the presence of defects due to fluorination. As the exposure time further increases, the intensity of 2D peak is suppressed and the D peak emerges, indicating that graphene is becoming more fluorinated.

Figure 5.6: AFM topography and AFM friction map scanned on the area indicated with the red box (i) in Figure 5.4 (a). (a) Topography image from which it is clear that fluorination does not modify the roughness or topography of the area, (b) The corresponding friction signal taken at the same area. Darker region corresponds to lower friction forces. (c) Friction image collected on a different area. (d) High-resolution lateral force image acquired on the pristine graphene in (c), atomic stick-slip friction can be resolved with a periodic lattice, indicating the surface is highly ordered. (e) High-resolution lateral force image taken on FG. The absence of stick-slip friction on FG suggests that fluorination has destroyed the regularity of the graphene surface.

Figure 5.7: Friction *vs.* load data acquired across the graphene-FG boundary. Comparison of friction *vs.* normal load data sets plotted obtained by AFM experimental data. The slope of the two data sets are fit by a linear function, revealing a 6× difference for friction coefficients between FG and pristine graphene. (b) Ratio of measured coefficient of friction (from linear fits to respective friction *vs*. normal load plots) between fluorinated graphene and graphene, as a function of fluorination time. Labeled vertical lines indicate specific stoichiometries determined from X-ray photoelectron spectroscopy (XPS) for corresponding fluorination times.

Figure 5.8: Results from MD simulations. (a) Friction as a function of normal load for pristine graphene, C_8F, C_4F, and C_2F. A strong increase in friction occurs once the graphene is fluorinated. Additional fluorination does not affect the friction further. Overall $\mu_{FG}/\mu_{graphene}$ ratio ranges between 7.3-8.0. (b) Corrugation amplitude of the potential energy as a function of atomic content of fluorine on graphene from the simulations in (a), calculations performed at 3 different loads: 0, 10, and 20 nN. (c)-(f) Contour maps of the tip-sample potential energy for the same

samples. Each map is shown for an area of ~0.7×1.0 nm^2. The color scale for all three maps covers the range 0-0.9 eV.

Figure 5.9: Simulation results for C_4F. (a) Friction traces obtained in MD simulations of sliding on ordered FG and graphene. Consistent with the experimental observations, the simulation results indicate that friction on FG samples is much higher than that on pristine graphene. Because of the regular distribution of F atoms on graphene, the friction profile shows ordered pattern for FG samples that is different from the experiments. (b) The line profiles of the friction force for disordered C_4F as a function of normal load.
Figure 6.1: Gold samples prepared through thermal evaporation onto freshly-cleaved muscovite mica. The nominal thickness of the gold layer is 300 nm. (a) Optical camera image of the as-deposited sample; (b) AFM topography image, as-deposited; grains with an average size of ~100 nm are visible. (c) AFM topography, after annealing, showing many atomically flat terraces.
Figure 6.2: NI USB-BNS 6125, with a data sampling rate of 1.25 MHz. Only one analogue input channel is connected to the lateral signal channel output from the AFM controller.

Figure 6.3: (a): Photographs of the newly designed sample holder. The green arrow indicates the flat top assembly of the new sample holder. (b) A close-up photograph shows the shear piezo mounted on a ramp. The blue arrow indicates the direction of shearing. The green arrows indicate the lead wires supplying voltage to the shear piezo. (c) Schematic cross-sectional view of the sample when mounted onto the shear piezo and a steel wedge. The steel wedge is has an angle of 5° to compensate the intrinsic tilt angle of the AFM yet allowing the tip to approach. (d) The new sample holder mounted into the AFM chamber. (e) AFM cantilever and a gold sample. Due to the steel wedge, the tip can be brought into contact by walking the AFM scanner laterally to the left.

Figure 6.4: MD model of the SiO_2 tip scanning across the Au(111) substrate. Gold-colored spheres represent gold atoms. Black-grey particles represent SiO_2. The red arrows indicate the direction of the normal load.
Figure 6.5: (a) Topographic image shows large terraces (> 100 nm^2) are observed on the Au(111) surface. The quality of the surface preparation was verified by the presence of herringbone surface reconstruction (shown in (b)) and the stick-slip pattern in the friction signal (shown in (c)).
Figure 6.6: *Pre-mortem* TEM images of Tips 1 and 2 used for data acquisition. The initial tip radius for Tip 1 is 4.9 nm and 3.6 nm for Tip 2.

Figure 6.7: Step-by-step schematic illustration of the analysis method using custom-written MATLAB script. The algorithm is used to extract individual friction loops in the string of data collected at each frequency. (a) A representative friction *vs.* time data acquired at 300 Hz with Tip 1. At sliding time ~150 ms the shear piezo was actuated for 10 cycles and stopped immediately, at sliding time ~175 ms; given the frequency, 10 cycles lasted for ~33.3 ms. (b) A zoomed-in plot of the individual sliding cycles at the red dashed box in (a). MATLAB script is then used to identify forward and reverse scan directions, and plotted *vs*. sliding distance in (d). From (d), fiction force is calculated.
Figure 6.8: Friction force *vs*. scanning speed for Tip 1 (black squares) and 2 (red circles). The solid line (Tip 1) and dashed line (Tip 2) are fits of the PTT model to the data, which yield, for Tip 1: F_c= 1.5±0.2 nN, β = (4.8 ± 2.0)×10^5 $N^{3/2}$/J, and f_0 = 108±42 kHz; and for Tip 2: F_c = 0.9±0.2 nN, β = (2.5±0.3)×10^5 $N^{3/2}$/J, and f_0 = 700±200 kHz. The normal applied force is 0.0±0.2 nN in both data sets. Error bars represent the standard deviation in the calculated mean friction

force. Top-left inset shows a friction loop acquired with Tip 1 at ~5.8 μm/s; an atomic stick-slip pattern can be clearly resolved corresponding to scanning along the [110] direction.

Figure 6.9: Friction force as a function of scanning speed from MD at 300 K (cyan diamonds) and 0.5 K (purple triangles), and PRD (blue circles) at 300 K. Dashed lines indicate fits of the PRD data to the PTT model using a value of F_c of 2.56±0.02 nN from the simulations run at 0.5 K, yielding β=(2.9±0.2)×105 $N^{3/2}$/J and f_0=120±30 GHz.

Figure 6.10: MD (cyan and red solid diamonds), PRD (blue solid circles), and experimental results from Tip 1 (black squares) and Tip 2 (red solid circles) plotted together. MD predictions are reported for 1.0 nm (cyan diamonds) and 2.2 nm (red diamonds) contact radii, r_c, where the latter is consistent with an extrapolation of the low-speed friction trend observed for Tip 1. The relationship between F_c and contact size is also used to extrapolate the PRD data to a 2.2 nm contact radius (blue hollow circles).

Figure 6.11: Master equation method (two-noise model) fit to experimental data. One can observe that due to the instrument noise, it is possible to reproduce two transitions in friction *vs.* speed data.

Figure 6.12: Pull-off force acquired as a function of sample temperature, ranging from ~115 – 300 K. No systematic variation of the pull-off force with temperature was not observed. The blue dash line represents the mean value (~7.3 nN) of the data set and the red box indicates the range of the standard deviation of the mean.

Figure 6.13: Stick-slip friction is clearly observed for scans performed near RT (a), however, as the temperatures increases (b), the pattern significantly decreased compared the one obtained at RT shown in (a). These images were used for calculating friction forces. (c) Friction *vs.* sample temperature varied from ~115 – 480 K, a strong decrease in friction was observed, data acquired at a 17 nm/s scan speed.

Figure 6.14: (a) Friction *vs.* temperature data acquired at three different speeds. For all three speeds, friction drops rapidly as a function of temperature up to RT, at which point friction remains fairly insensitive to temperature. Inset: At cryogenic temperatures, a trend of speed-dependent friction at a particular temperature is visible, indicating that at those temperatures, friction is more sensitive to speeds than above ~180 K. Straight lines are drawn simply to indicate the trend. (b) MD simulation results from studies at a comparable temperature range after closely matching the test parameters, plotted for the same axis ranges as (a). Similar friction behavior is observed, although the dependence is far less strong compared to the experiments. The inset shows that the friction forces are also slightly affected by the scanning speed, with higher scanning speeds leading to higher friction, as seen previously for studies at room temperature.

LIST OF SYMBOLS

Latin symbols

a	lattice spacing
a_r	real contact radius
A_r	real contact area
b	width of the cantilever
E	Young's modulus
E_0	potential energy barrier height
E_c	composite Young's modulus
f_0	attempt frequency
$f_{0,n}$	cantilever normal resonance frequency
$f_{0,t}$	cantilever torsional resonance frequency
F_{adh}	adhesion force
$F_{adh,\ DMT}$	adhesion force in the DMT model
$F_{adh,\ JKR}$	adhesion force in the JKR model
F_c	mean friction force at zero Kelvin
F_f	friction force
F_L	lateral force
$F_{L,fwd}$	lateral force forward direction
$F_{L,bwd}$	lateral force backward direction
F_n	normal force
F_{po}	pull-off force
G	shear modulus
G^*	reduced shear modulus
h	tip height
k	spring stiffness
k_B	Boltzmann constant
$k_{contact}$	lateral contact stiffness
k_L	cantilever lateral stiffness
k_{tip}	lateral stiffness of the tip
k_{tot}	total lateral stiffness
k_φ	torsional stiffness
l	cantilever length
m	mass
Q_n	normal resonance quality factor
Q_t	torsional resonance quality factor
r_c	contact radius
R	tip radius

S	sensitivity of photosensitive detector
t	cantilever thickness
T	temperature
v	scanning speed
v_0	characteristic speed
$V_{\text{a-b}}$	normal photo detector signal
$V_{\text{c-d}}$	lateral photo detector signal
w	cantilever width
$w_{gr\text{-}sub}$	graphene-substrate interaction strength
$w_{tip\text{-}gr}$	tip-graphene interaction strength
W_{12}	work of adhesion
z_0	equilibrium separation between two bodies

Greek symbols

β	parameter related to the lateral potential profile
ε	depth of the potential well in the Lennar-Jones potential
δ	elastic deformation
ΔE	energy corrugation amplitude
Γ_i^n	imaginary part of the normal hydrodynamic damping function for a rectangular cantilever
Γ_i^t	imaginary part of the torsional hydrodynamic damping function for a rectangular cantilever
λ	Maugis transition parameter
η	viscosity of the medium
ρ	material density
ρ_f	fluid density
σ	equilibrium distance in the Lennar-Jones potential
τ	interfacial shear strength
μ	friction coefficient
μ_{FG}	friction coefficient on fluorinated graphene
μ_{graphene}	friction coefficient on graphene
μ_T	Tabor's parameter
ν	Poisson's ratio

Chapter 1: Introduction and Important of Tribology

Tribology, a field whose name was coined in the 1960s and derived from the Greek word ‘tribos’ for ‘rubbing’, is the multi-disciplinary study of friction, adhesion, lubrication, and wear [1]. Although this name is relatively new, the founding ideas have been known for centuries. As any pair of contacting bodies with relative motion experiences frictional dissipation, it is therefore one of the oldest physical phenomena that we know. While humankind has dealt with friction phenomena already since the ancient times, as illustrated by wall paintings found in an ancient Egyptian tomb dating from the 18^{th} century BC [2], the first recorded scientific study on friction was not carried out until the 15^{th} century AD by Leonardo da Vinci, and further developed by Guillaume Amontons and Charles-Augustin de Coulomb in the 17^{th} century [3].

The multi-disciplinary nature of tribological phenomena is well demonstrated in the fact that tribology is relevant across a tremendous range of length scales. For example, starting from the kilometer scale, geoscientists study tribology in order to better understand the behavior of tectonic plates and thus to better predict earthquakes [4, 5]. At the meter scale, mechanical engineers and material scientists study tribology to improve the fuel efficiency of automobiles [6, 7]. Thanks to the continued development of tribological sciences, automobiles have become more efficient, safer, and more reliable [8]. At the micrometer scale, tribology is relevant for the performance of hard disk drives and other microscale devices which are commonly found in modern Digital Light Processing (DLP) projectors [8]. In particular, hard disk drive technology poses a great challenge for tribology given the ongoing demands for increase in data storage capacity

and reduction in size [9]. From 1956, with the introduction of the first computer hard disk drive, to today, the storage density has increased by a factor of ~10^9 [8, 9]. Finally, at the nanometer scale, tribology is relevant in studying fundamental physical phenomena, including atomic-scale vibrations, sliding, and wear [10-14].

Despite its long history, the importance of tribology was first pointed out only a half century ago by H. P. Jost to the government of the United Kingdom in his seminal 'Jost Report' in 1966 [1]. This report then triggered a significant investment in tribology research. Jost recognized that 1.3%-1.6% of the gross national product of an industrialized country could potentially be saved through proper understanding and control of tribology [15]. This percentage equates to hundreds of billions of dollars annually in the United States alone. Knowing that undesired friction, adhesion, and wear are pathways of energy loss and material waste, tremendous gains can potentially be attained in energy efficiency and reduced material consumption if friction, adhesion, and wear could be better understood and controlled. In the light of the increasing need for energy and the decreasing available energy resources, it is vital to humanity to learn how to deal with friction, lubrication, and wear, making the field of tribology a highly relevant area of fundamental and application-oriented research. Another industrial and societal aspect that continually requires better knowledge of tribology is the rapidly growing field of nanotechnology, namely the link between the atomic and nanometer structure of materials and their respective tribological properties. This field also includes the study of device miniaturization, such as the design and fabrication of micro- and nanoelectromechanical systems (M-/NEMS). Specifically, as devices shrink in size, the

increased surface-to-volume ratio ensures that friction and other interfacial forces such as adhesion become a critical concern, compared to larger-scale machines.

Despite the long history of friction, our current understanding of the fundamental principles that govern friction remains incomplete. Fundamentally, this fact is best demonstrated by the fact that there is no fundamental theory available yet to predict friction. Before the advent of microscale/nanoscale tribology, due to the complexity of tribological interactions, much of the insight made was largely empirical or was gained through trial-and-error. Indeed, interactions between two surfaces in contact and/or relative motion, either through rolling or sliding, are governed by a large number of physical parameters, including material properties, the shape of the contacting bodies, their topography, and chemical and physical compositions, as well as the interaction conditions, such as the speed of the relative motion, temperature, direction of scanning, applied load, presence of lubricant, air or vacuum etc. Additionally, the fact that the contact is constantly evolving makes studying it even more challenging. For example, during the motion, the contact interface can evolve as a result of frictional heating, material transfer or loss, elastic and/or plastic deformation, bond formation and breakage between the two surfaces, or the occurrence of other chemical reactions, such as protective layers.

Owing to the advancement of instrumentation tools (and complemented by simulation techniques), it is now possible to better understand the fundamental mechanisms as we can examine sub-microscale, single-point contacts (known as asperities) with extremely high force and displacement resolution [16]. Therefore, one highly successful approach of studying tribology is to reduce the interacting interface to

small scales, where one can more easily isolate the interaction parameters and identify their influences. This approach defines the relatively recently identified field of *nanotribology*, which has become increasingly relevant since 1990s. Using the knowledge gained at the small-scale single-asperity contacts, fundamental physical mechanisms of friction can be identified and subsequently bridged and applied to larger-scale multi-asperity contacts. This thesis, however, will not cover all friction-related disciplines; instead, its main focus will be studying the mechanisms controlling friction and adhesion at dry, nearly wearless, elastic contacts at the atomic length-scale by examining interfaces between materials that are simple and well-defined, but also scientifically and technologically relevant, including contacts between silicon AFM tips and two-dimensional (2-D) solid lubricants, and between silicon AFM tips and gold surfaces. The overall objective of this thesis will be to contribute to a deeper understanding of the origins of friction and adhesion, which will benefit scientists and engineers in both nanoscopic and macroscopic research communities. Indeed, achieving those goals has the potential to produce highly useful insights into larger-scale contact phenomena, which will certainly be applicable to many different length scales, including M-/NEMS devices, the automobile industry, or even systems as large as tectonic plates in geosciences.

This thesis has been structured as follows. Following the Introduction (Chapter 1), a literature review of the published literature on friction and adhesion at the nanoscale will be presented in Chapter 2. Chapter 3 will discuss the experimental tools and analysis techniques used in the studies presented in this thesis. Chapters 4 through 6 will discuss the experimental results collected and analyzed within this thesis. Specifically, Chapter 4

will present work on adhesion studies on graphene, one of the most promising 2-D materials, partially based on the work published in Ref. [17]. In Chapter 5, friction studies on graphene and fluorinated graphene, partially based on the work in Ref. [18] will be presented. Chapter 6 will cover novel results obtained during this PhD on thermally-activated friction processes during sliding, including the speed-dependence friction on gold thin films, already published in Ref. [19], as well as studies of temperature dependence of friction for contacts with bulk molybdenum disulfide (MoS_2). Finally, in Chapter 7, I will draw conclusions from the previous chapters and point out the future plans.

References

1. H.P. Jost, *Lubrication: Tribology; Education and Research; Report on the Present Position and Industry's Needs (submitted to the Department of Education and Science by the Lubrication Engineering and Research) Working Group*; HM Stationery Office: 1966.
2. B. Bhushan, *Tribology and Mechanics of Magnetic Storage Devices*; Springer-Verlag: New York, 1996.
3. D. Dowson, *History of Tribology*; Professional Engineering Publishing Limited: London, UK, 1998.
4. C. Marone, Laboratory-derived friction laws and their application to seismic faulting. *Annual Review of Earth and Planetary Sciences* **1998**, 26(1), 643-696.
5. Q. Li, T.E. Tullis, D. Goldsby, and R.W. Carpick, Frictional ageing from interfacial bonding and the origins of rate and state friction. *Nature* **2011**, 480(7376), 233-236.
6. C. Taylor, Automobile engine tribology—design considerations for efficiency and durability. *Wear* **1998**, 221(1), 1-8.
7. K. Holmberg, P. Andersson, and A. Erdemir, Global energy consumption due to friction in passenger cars. *Tribology International* **2012**, 47, 221-234.
8. C.M. Mate, *Tribology on the Small Scale: A Bottom Up Approach to Friction, Lubrication, and Wear*; Oxford University Press: Oxford, UK, 2008.

9. B. Marchon, T. Pitchford, Y.-T. Hsia, and S. Gangopadhyay, The head-disk interface roadmap to an areal density of Tbit/in 2. *Advances in Tribology* **2013**, 2013, 8.
10. A. Socoliuc, E. Gnecco, S. Maier, O. Pfeiffer, A. Baratoff, R. Bennewitz, and E. Meyer, Atomic-scale control of friction by actuation of nanometer-sized contacts. *Science* **2006**, 313(5784), 207-10.
11. J.Y. Park, D. Ogletree, P. Thiel, and M. Salmeron, Electronic control of friction in silicon pn junctions. *Science* **2006**, 313(5784), 186.
12. R.J. Cannara, M.J. Brukman, K. Cimatu, A.V. Sumant, S. Baldelli, and R.W. Carpick, Nanoscale friction varied by isotopic shifting of surface vibrational frequencies. *Science* **2007**, 318(5851), 780-3.
13. C. Lee, Q. Li, W. Kalb, X.-Z. Liu, H. Berger, R.W. Carpick, and J. Hone, Frictional characteristics of atomically thin sheets. *Science* **2010**, 328(5974), 76.
14. T.D.B. Jacobs and R.W. Carpick, Nanoscale wear as a stress-assisted chemical reaction. *Nature Nanotechnology* **2013**, 8(2), 108-112.
15. H.P. Jost, Tribology—origin and future. *Wear* **1990**, 136(1), 1-17.
16. I. Szlufarska, M. Chandross, and R.W. Carpick, Recent advances in single-asperity nanotribology. *Journal of Physics D: Applied Physics* **2008**, 41(12), 123001.
17. X.-Z. Liu, Q. Li, P. Egberts, and R.W. Carpick, Nanoscale adhesive properties of graphene: The effect of sliding history. *Advanced Materials Interfaces* **2014**, 1-9.
18. Q. Li, X.-Z. Liu, S.-P. Kim, V.B. Shenoy, P.E. Sheehan, J.T. Robinson, and R.W. Carpick, Fluorination of graphene enhances friction due to increased corrugation. *Nano Letters* **2014**, 5212–5217.
19. X.-Z. Liu, Z. Ye, Y. Dong, P. Egberts, R.W. Carpick, and A. Martini, Dynamics of atomic stick-slip friction examined with atomic force microscopy and atomistic simulations at overlapping speeds. *Physical Review Letters* **2015**, 114(14), 146102.

Chapter 2: Friction and Adhesion: A Review

2.1.1: Introduction to Friction

The *classical* friction laws we know today were largely the results initiated by da Vinci, Amontons, and Coulomb. From his experiments with sliding blocks and rolling weights, da Vinci empirically found that friction is doubled when the block's weight is doubled, and it is independent of the planar dimensions of the object, as long as the weight is not changed [1]. About two hundred years after da Vinci, Amontons published the first scientific report on macroscopic friction laws by reformulating da Vinci's findings in a mathematical way:

(1) The friction force F_f is directly proportional to load (normal force) F_n:

$$F_f = \mu F_n , \tag{2.1}$$

with μ being a proportional factor that is known as the frictional coefficient and is a property of the pair of surfaces in contact.

(2) The friction force is independent of the apparent contact area between the sliding surfaces [1]. About a century later, Coulomb built further on this and developed the understanding of friction by uncovering the difference between static and kinetic friction, and added an observation that the friction force is almost independent of the scanning speed within a practical speed range. Those classical laws of friction still hold for a wide range, macroscopic sliding interfaces and remain extensively used currently.

During the first part of the twentieth century, along with the advancement of modern physics, including the invention of the theory of relativity and quantum mechanics, Bowden and Tabor realized that virtually all surfaces are rough, and that for a

contacting interface, the true contact area is actually a very small percentage of the apparent contact area (which Amontons had considered in his formulation) [2]. The true contact area, rather, consists of a number of smaller individual asperities, which are created when two macroscopic surfaces are brought together. This hierarchy is demonstrated in Figure 2.1. Given that friction is governed by these asperities, Bowden and Tabor then re-formulated the friction law by including the observation that F_f is proportional to the true contact area, as given by

$$F_f = \tau A_r, \tag{2.2}$$

where τ is the average interfacial shear strength of the contact and A_r the real contact area. Later on, Greenwood and Williamson found that for surfaces with randomly roughness, A_r is nearly linearly proportional to the load F_n [3], in which case, the classical friction law in Equation 2.1 is recovered. In more modern approaches, the real contact area was observed to be linearly proportional to the load at low loads for self-affine surfaces [4, 5].

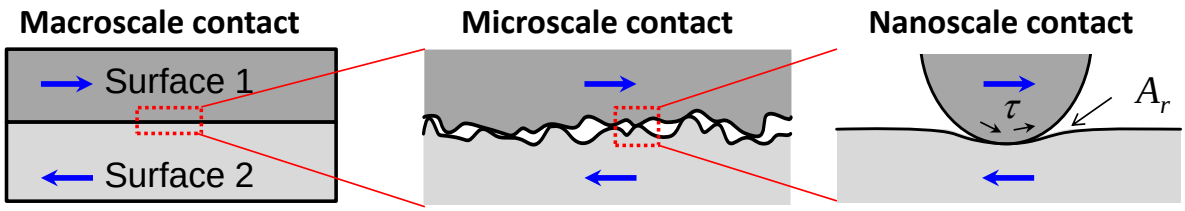

Figure 2.1: Schematics of sliding contacts at three different length scales: macro-, micro-, and nanoscale. At the macroscale, two surfaces are seemingly flat; at the microscale, the contact consists of multi-asperities; at the nanoscale, single-asperity contact can be revealed. A_r denotes the real contact area.

2.1.2: Microscopic Single-Asperity Friction

For microscopic single-asperity contacts, one often applies the contact mechanics models of a single asperity being pressed into contact with a flat surface under some applied load to interpret experimental friction results within the context of the previously discussed theories of friction. This 'asperity-on-flat' problem is approximated such that the model of sphere on a flat can be applied. This approximation lets us gain insight into the nature of single-asperity contact. A commonly used model that works extremely well is the Hertz model [6], as formulated by Heinrich Hertz, who was considered to be the first to set the foundation for the field of modern contact mechanics [6] when he analyzed the elastic deformation for an elliptical contact area. According to the Hertz model, the real contact area A_r, and elastic deformation δ for circular contact between a spherical lens and a flat plane under an applied normal force F_n can be described by the equation:

$$A_r = \pi \left(\frac{3F_n R}{4E_c}\right)^{\frac{2}{3}} \tag{2.3}$$

and

$$\delta = \pi \left(\frac{9F_n^2}{16RE_c^2}\right)^{\frac{1}{3}}, \tag{2.4}$$

where R is the radius of the sphere, E_c is the so-called composite elastic modulus of the contacting materials and defined as $\frac{1}{E_c} = \frac{1-\nu_1^2}{E_1} + \frac{1-\nu_2^2}{E_2}$. Here, E_1 and E_2 represent the Young's moduli of the sphere and plane; ν_1 and ν_2 are the Poisson's ratio of the sphere and plane. The Hertz model considers the area of a smooth macroscopic contact between two homogeneous, isotropic, linear elastic materials and does not consider any attractive forces acting between the bodies. Moreover, Hertz model also assumes that the radius of

the sphere is much greater than the radius of the true contact, strains are small, and finally that no friction exists between the sphere and the flat [6].

When the shear strength τ is taken as a constant, friction is then calculated by

$$F_f = \tau\,\pi\left(\frac{3F_nR}{4E_c}\right)^{\frac{2}{3}}, \tag{2.5}$$

or more simply $F_f \propto F_n^{2/3}$. Although this dependence has been shown to be reasonably accurate, it turns out that particularly at the microscale and nanoscale, contacts *are* adhesive, and more challenging is that the effect of adhesion is rather crucial and thus cannot be neglected. Following this, two important models were introduced. The first is the Johnson-Kendall-Roberts (JKR) model, which considered that due to the surface energies of the contacting solids, the adhesive force will result in a tensile stress at the outer edge of the contact and cause elastic deformation [7]. This model included the adhesion force and formulated a new equation for the contact radius and deformation δ that is greater than the non-adhesive Hertz contact. Another important contact mechanics is the Derjaguin–Müller–Toporov (DMT) model [8], which provides the other limit of infinite range adhesion interaction, as is more applicable for perfectly rigid solids [8, 9]. The DMT model also adds an extra term representing the adhesion force to the total contact area. In short, the JKR and DMT models provide two limiting cases: JKR is valid where the elastic deformation induced by adhesion greatly exceeds the range of the adhesive interactions, which is the case for contacts of low stiffness, large radius of the sphere and work of adhesion, and small interaction range. In contrary, DMT is valid in the case when the contacting bodies are highly stiff, and have a weak, long-range adhesion interaction.

All three models predict a non-linear dependence of contact area *vs.* load; which early on has been confirmed by a considerable amount of experimental studies on a single-asperity contact, including Refs. [10-14]. While the JKR and DMT models seemed contradictory, Tabor formulated that the two models are in fact the two ends of the spectrum, and defined a transition parameter or the so-called Tobor parameter μ_T [15]

$$\mu_T = \left(\frac{RW^2}{E_c^2 z_0^3}\right)^{1/3}, \tag{2.6}$$

where W is the work of adhesion, z_0 is the equilibrium separation between the two bodies. The Tabor parameter was used to examine the model that applies depending on the degree of elastic deformation and the range of adhesion: for large μ_T the JKR model applies and the DMT models applies for small μ_T. The use of the Tabor parameter will be discussed more in Chapter 6. Maugis further combined the JKR and DMT models together to interpolate the two limiting cases in order to deal with intermediate cases [16]. In this Maugis-Dugdale (M-D) model, he defined the transition parameter, the Maugis parameter λ, that can be used to evaluate the regime that applies to a certain problem, either JKR, DMT, or intermediate. The transition parameter is equal to $1.16\mu_T$. It is shown that the JKR model is applicable when λ>5, and DMT when λ<0.1, whereas the Hertz model applies when λ=0 [16].

2.1.3: Atomic-Scale Stick-Slip Friction

Besides the observations of frictional properties that deviate from classical friction laws, another interesting observation in nanotribology that was possible due to the development of the AFM is atomic-scale stick-slip behavior on crystalline surfaces.

This behavior, unlike the conventional macroscopic stick-slip behavior observed *e.g.* in creaking door hinges, screeching tires, or even in earthquakes, originates from the atomic-scale periodicity of the substrate atomic lattice as the tip, which often has an amorphous crystal structure, slides across the surface. Atomic stick-slip behavior is manifested as a very characteristic saw-tooth shape of the lateral force that is caused by the AFM probe tip jumping unstably over single, or, under certain conditions, over a multiple number of lattice spacing [17, 18]. Mate *et al.* published first pioneering results on atomic stick-slip using a tungsten tip sliding over a graphite surface (Figure 2.2 [19]).

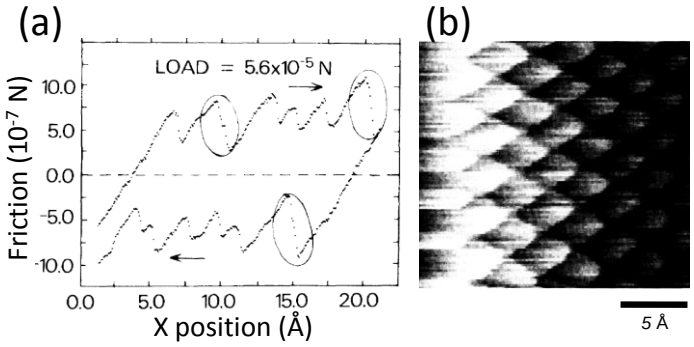

Figure 2.2: First atomic stick-slip friction data acquired with a tungsten tip on a graphite surface. (a) A characteristic saw-tooth pattern can be resolved, where the period of the pattern corresponds to the graphite lattice. (b) A regular pattern indicating the graphite lattice can be resolved. Adapted from Mate *et al.* [19].

Atomic stick-slip motion is a seemingly simple process, yet it contains a wealth of physical information, of which some is not fully understood yet, which will be discussed in more detail in Chapter 6. Atomic stick-slip motion can be understood in the following manner: the tip and substrate stick together initially while lateral strain builds up because of a high interfacial potential barrier – this is referred to as sticking, as shown in Figure

2.3, cases (a)-(c). When the lateral strain reaches a maximum value, the tip will slide rapidly with respect to the sample – this is referred to as slipping, shown as case (d) in Figure 2.3. This slip will result in the tip slipping one (or an integer number) of atomic lattice spaces until the tip becomes stuck in a surface potential minima once again. The process repeats itself as the strain energy needs to be built up again until the magnitude reaches a critical value to initiate the next slip event. Schematically, atomic stick-slip motion can be visualized with the saw-tooth pattern shown in Figure 2.3. From this figure, note that stick-slip behavior is characterized by the slow sticking phase followed by fast slipping of the tip with respect to the sample, with a contact area of multiple atoms involved, rather than the AFM tip smoothly tracing out individual atomic corrugations. After Mate *et al.*'s work, it has been reported that many other materials also exhibit atomic stick-slip friction, including muscovite mica [20], MoS_2 [21], diamond [22], as well as some metallic materials (*e.g.* copper [23] and gold [24]), and some ionic crystals (*e.g.* NaCl, NaF, KBr) [25-27].

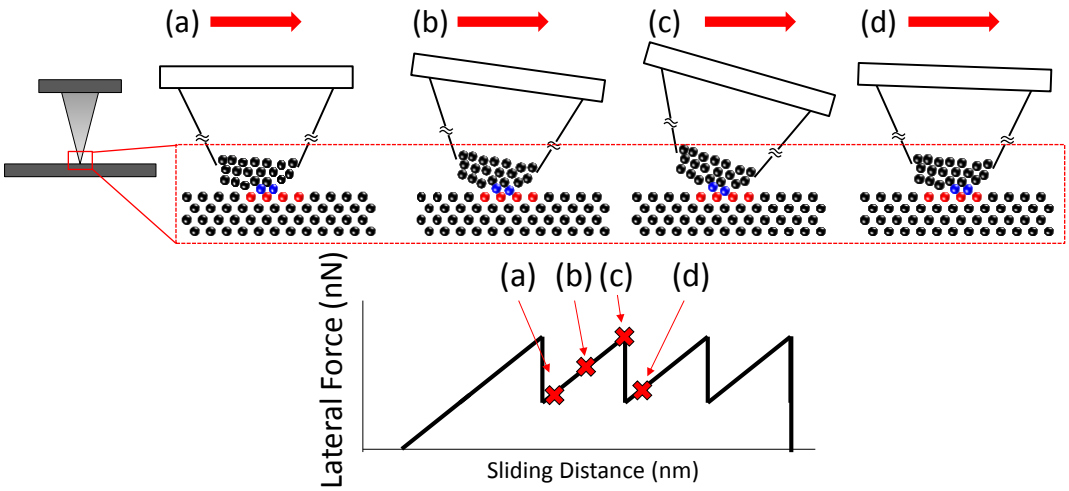

Figure 2.3: Cartoon showing atomic stick-slip motion for an AFM tip with an amorphous tip apex sliding across a crystalline surface. Red arrows indicate the sliding direction. From (a) to (c), the torsion of the cantilever is increasing while the tip apex is stuck at one position corresponding to the potential minimum. When the elastic strain in the cantilever reaches a critical magnitude, the tip apex will overcome the potential minimum, and thus the strain is quickly released by slipping quickly to the next position, as drawn in (d). This process repeats itself and the recorded lateral signal will produce a regular saw-tooth pattern, where the period of the pattern corresponds to the lattice spacing of the crystal.

Several theories have appeared as an attempt to explain and model atomic stick-slip behavior, and among them is the Prandtl-Tomlinson (PT) model, which was introduced in 1929 [28, 29]. The model is schematically depicted in Figure 2.4. In this one-dimensional (1-D) model, the atoms (grey spheres) ordered within a lattice acts a series of periodically-arranged energy barriers that the tip (blue sphere) must overcome as it slides over the surface. The elastic forces between the tip and sample, as well as the force generated by the cantilever, are modeled as a single spring with a stiffness *k* pulling the tip along the surface by the scanner (black rectangle), which defines the scanning

speed. As the tip slides along the surface, it becomes trapped in the potential minima between the atoms until sufficient elastic strain has built up in the spring to slide to the next site. When this occurs, the tip jumps to the next potential minima, advancing one atomic lattice position and resulting in the energy stored in the spring being dissipated. Determining where and how the stored elastic energy is dissipated is of great importance in order to explain the fundamental mechanisms of friction. The PT model has been expanded to address a number of important issues. For example, the stiffness of the tip-sample contact, tip, and cantilever all have different values separately considered in AFM experiments. Furthermore, the contact between the AFM asperity and the surface is not one point mass, since the AFM tip apex has a radius of ~10 nm.

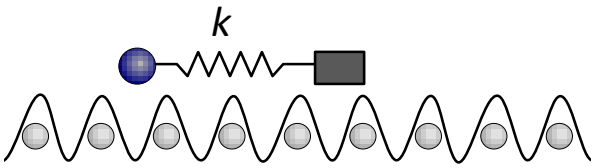

Figure 2.4: A 1-D representation of Tomlinson model. A monatomic tip (blue) scans over a fixed chain of atoms (grey). The tip is attached to a slider support (black rectangle) through an elastic spring having a stiffness *k*. The forces on the tip atom are $F_{\text{tip-sample}}$, arising from the interaction of the tip and sample and F_{elastic}, arising from the movement of the base.

Another common model is the Frenkel-Kontarova (FK) model [30], developed in 1938, which has another picture by taking a chain of atoms (representing atoms at the AFM tip apex) connected by springs with their direct neighbors. Hence, there is mutual interaction via harmonic potentials as represented by springs. The FK model is schematically depicted in Figure 2.5. Similar to the PT model, while pulling the chain along the periodic potential, the tip atoms feel a resistive force also from the gradient of

the periodic potentials in the surface. For the case of equal density of tip atoms and potential minima, and in the absence of lateral force, the equilibrium configuration is for all atoms to stay at the bottoms of the potential well. Pulling on the chain will build an elastic stress in the springs (sticking) and eventually cause the atoms to move up the side of the potential well and quickly slide down to the next bottom simultaneously (slipping). This special equal density case gives a maximum lateral force needed for sliding which is equal to the sum of the force to overcome each individual potential well. For the case of incommensurability, if the chain is stiff enough compared to the magnitude of the potential, the chain becomes free of the potential. This also will result in superlubricity since the loss and gain of each atom's interaction energy will cancel out each other [31, 32]. Additionally, if the number of atoms is not equal to the number of wells, friction is also greatly reduced.

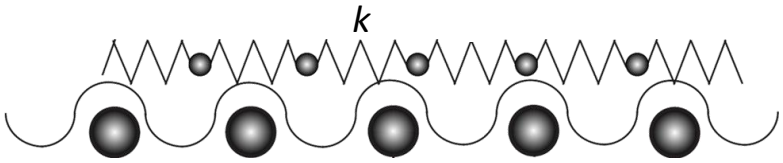

Figure 2.5: 1-D schematic of the FK model in which the tip atoms are connected by springs, having a force constant *k*, with their direct neighbors. They interact with each other while experiencing the surface potential. Pulling on the chain will build an elastic stress in the springs (sticking) and eventually cause the atoms to move up the side of the potential well and quickly slide down to the next bottom simultaneously (slipping).

2.2: Review of Adhesion Phenomena

Adhesion, which describes the energy of attraction between two surfaces, is another critical parameter that must be characterized in the fields of surface science and

nanotribology. Adhesion results from the attractive interaction between the two materials. The effect of adhesion increases at small scales, since the body forces scale with the object's volume whereas the surfaces forces scale with the radius of curvature and surface area. In tribological studies, adhesion is typically characterized as a force, and it is strongly geometry-dependent. Therefore, to better relate it to more fundamental quantities in surface science, such as surface energy, interfacial energy, and work of adhesion, models that can describe adhesion, based on physical assumptions and in terms of energies for given geometries must be considered.

As previously introduced, several existing contact mechanics models have considered adhesion. The Derjaguin approximation was the first to formulate the force to separate two contacting bodies, F_{adh}, may be estimated for two spheres (deformation neglected) using [33]

$$F_{\text{adh}} = -2\pi \left(\frac{R_1 R_2}{R_1+R_2}\right) W_{12}. \tag{2.7}$$

Here, R_1 and R_2 represent the radii of the spheres 1 and 2; W_{12} is the work of adhesion per unit area given as a function of distance D. The negative sign indicates that the force is compressive for positive values of R and W. W_{12} is determined by the difference in total energy per unit area between the interface and its isolated slabs, as formulated in the Dupré equation [9]: $W_{12} = \gamma_1 + \gamma_2 - \gamma_{12}$. In this equation, γ_1 denotes the surface energy of material 1, γ_2 the surface energy of material 2, and γ_{12} the interfacial energy between 1 and 2, the unit of γ is energy/area. It is then trivial to apply this analysis to a sphere-on-flat configuration (*i.e.* R_1=R, R_2=∞), which is more commonly considered in tribology, the Derjaguin approximation becomes

$$F_{\text{adh,DMT}} = -2\pi R W_{12}. \quad (2.8)$$

Here, the adhesive force is then only dependent on the radius of the sphere and the work of adhesion between materials 1 and 2. This equation is identical to the case of the DMT model, which is more valid in cases of rigid solids. For more compliant bodies, which is in the opposite limiting case, the JKR model describes more accurately the contact and adhesion properties between them [34], resulting in a different expression relating the adhesion force with the work of adhesion:

$$F_{\text{adh,JKR}} = -\frac{3}{2}\pi R W_{12}. \quad (2.9)$$

As discussed before, the M-D model shows a transition between these two values of adhesion forces obtained by JKR and DMT models.

2.3: Brief Discussion on Computer Simulations in Tribology

While significant progress in nanotribology was made possible thanks to the success in experimental tools, particularly the AFM, one important drawback of it (and some other characterization tools, including the surface force apparatus (SFA) and the quartz crystal microbalance (QCM)) is the inability to observe *in-situ* the buried interface for a nanoscale single-asperity contact. Although analytical models, such as the aforementioned FK and PT models, were able to help explain experimental observations, they are quite limited because they usually consider ideal conditions, *e.g.* zero temperatures, and/or impose assumptions, *e.g.* wearless sliding, no heat dissipation etc. Computer simulations can avoid some of those issues and have been extremely powerful tools to investigate nanoscale friction phenomena at the buried interface by providing atomistic insights, predicting new observations and also explaining experimental results,

and in turn, experiments can help validate simulation results. The rapid advancements of computing hardware were primarily responsible for popularity and usefulness of computer simulations. It is beyond the scope of this thesis to discuss the simulation techniques in detail. Below is a brief introduction to the two widely used simulation techniques that were implemented by my collaborators by optimally matching the test parameters.

Computer simulations in tribology can perform virtual, numerical tests in which test parameters can be precisely predefined, such as the geometry, test conditions, and environmental parameters, and interactions between system's building blocks. Simulations allow us to explore the effect of those test parameters on friction, adhesion, lubrication, and wear. Unlike laboratory experiments, simulations enable tribologists to follow and analyze the full dynamics of each building block instantaneously. While all simulation results must be interpreted with care, several previous studies explicitly demonstrated (by direct comparison by matching experimental parameter or to other simulation techniques) that the useful physical information can be well captured by simulations [24, 35-37].

In tribology, one common simulation technique is the finite element method (FEM). FEM is a numerical technique in which the building blocks are considered as finite bodies governed by continuum mechanics, and problems are analyzed by finding approximate solutions to boundary value problems for partial differential equations. One major advantage of FEM is its capability of simulating a large range of systems with sizes from nanoscale contacts to macroscopic devices, such as automobile or buildings, at large time scales; on contrary, one possible disadvantage is that at the nanoscale the

applicability of FEM, or rather the continuum mechanics assumptions that form the basis of the mathematical equations solved in FEM, become questionable. To date, FEM has been utilized in many tribological studies across length scales, including the following reports [36, 38-43].

Another commonly used simulation technique in tribology is molecular dynamics (MD). MD simulations are based on atomistic interactions between the building blocks, *i.e.* atoms and/or molecules. MD is capable of tracking the evolution of each building block's configuration and energetic information by obtaining how displacements, velocities, and orientations of particles evolve with time. MD uses empirical potential energy models that describe the interaction between the particles. While MD is considered to be capable of capturing the discreteness of atoms and their respective interactions, compared with the continuum equations used in FEM simulations, the complex and large number of equations that must be formed typically limit the size of the simulation volume. Furthermore, given that MD calculates atomic-scale phenomena, calculations must be performed at very small time steps, on the order of pico- or femtoseconds, to capture the dynamics of atomic-scale phenomena.

Recently, many important fundamental discoveries in nanotribology were achieved thanks to various simulation works. For example, Luan *et al.* observed that continuum mechanics predictions may breakdown if the atomic arrangement at the surface is not properly considered [44]. Mo *et al.* found that continuum mechanics is well applicable to nanoscale friction in cases of large adhesion forces, but will fail for non-adhesive contacts [45]. Finally, with the increasing availability of computing power, researchers often utilize the combined approach of experiments and simulations, allowing

them to compare results obtained from the two techniques. Some recent examples of experimental studies combined with simulations for studying nanoscale friction include Refs. [24, 43, 46] and the excellent review papers [10, 47].

2.4: References

1. D. Dowson, *History of Tribology*; Professional Engineering Publishing Limited: London, UK, 1998.
2. F. Bowden and D. Tabor, The area of contact between stationary and between moving surfaces. *Proceedings of the Royal Society of London. Series A, Mathematical and Physical Sciences* **1939**, 169(938), 391-413.
3. J. Greenwood and J. Williamson, Contact of nominally flat surfaces. *Proceedings of the Royal Society of London. Series A. Mathematical and Physical Sciences* **1966**, 295(1442), 300-319.
4. B.N.J. Persson, Elastoplastic contact between randomly rough surfaces. *Physical Review Letters* **2001**, 87(11), 116101.
5. S. Hyun, L. Pei, J.F. Molinari, and M.O. Robbins, Finite-element analysis of contact between elastic self-affine surfaces. *Physical Review E* **2004**, 70(2), 026117.
6. K.L. Johnson, *Contact Mechanics*; Cambridge University Press: Cambridge, UK, 1987.
7. K.L. Johnson, K. Kendall, and A.D. Roberts, Surface energy and the contact of elastic solids. *Proceedings of the Royal Society of London A* **1971**, 324(1558), 301-313.
8. B. Derjaguin, V. Müller, and Y.P. Toporov, Effect of contact deformations on the adhesion of particles. *Journal of Colloid and Interface Science* **1975**, 53(2), 314-326.
9. C.M. Mate, *Tribology on the Small Scale: A Bottom Up Approach to Friction, Lubrication, and Wear*; Oxford University Press: Oxford, UK, 2008.
10. I. Szlufarska, M. Chandross, and R.W. Carpick, Recent advances in single-asperity nanotribology. *Journal of Physics D: Applied Physics* **2008**, 41(12), 123001.
11. R.W. Carpick, N. Agraït, D. Ogletree, and M. Salmeron, Measurement of interfacial shear (friction) with an ultrahigh vacuum atomic force microscope. *Journal of Vacuum Science & Technology B: Microelectronics and Nanometer Structures* **1996**, 14(2), 1289-1295.

12. U.D. Schwarz, O. Zwörner, P. Köster, and R. Wiesendanger, Quantitative analysis of the frictional properties of solid materials at low loads. *Physical Review B* **1997**, 56(11), 6987-6996.
13. E. Meyer, R. Lüthi, L. Howald, M. Bammerlin, M. Guggisberg, and H.J. Güntherodt, Site-specific friction force spectroscopy. *Journal of Vacuum Science & Technology B* **1996**, 14(2), 1285-1288.
14. M. Enachescu, R. Van Den Oetelaar, R.W. Carpick, D. Ogletree, C. Flipse, and M. Salmeron, Atomic force microscopy study of an ideally hard contact: the diamond (111)/tungsten carbide interface. *Physical Review Letters* **1998**, 81(9), 1877-1880.
15. D. Tabor, Surface forces and surface interactions. *Journal of colloid and interface science* **1977**, 58(1), 2-13.
16. D. Maugis, Adhesion of spheres: the JKR-DMT transition using a Dugdale model. *Journal of colloid and interface science* **1992**, 150(1), 243-269.
17. S. Medyanik, W. Liu, I.-H. Sung, and R.W. Carpick, Predictions and observations of multiple slip modes in atomic-scale friction. *Physical Review Letters* **2006**, 97(13), 136106.
18. S. Maier, Y. Sang, T. Filleter, M. Grant, R. Bennewitz, E. Gnecco, and E. Meyer, Fluctuations and jump dynamics in atomic friction experiments. *Physical Review B* **2005**, 72(24), 245418.
19. C.M. Mate, G.M. McClelland, R. Erlandsson, and S. Chiang, Atomic-scale friction of a tungsten tip on a graphite surface. *Physical Review Letters* **1987**, 59(17), 1942-1945.
20. S. Fujisawa, Y. Sugawara, S. Morita, S. Ito, S. Mishima, and T. Okada, Study on the stick-slip phenomenon on a cleaved surface of the muscovite mica using an atomic force/lateral force microscope. *Journal of Vacuum Science Technology B* **1994**, 12(3), 1635-1637.
21. S. Morita, S. Fujisawa, and Y. Sugawara, Spatially quantized friction with a lattice periodicity. *Surface Science Reports* **1996**, 23(1), 1-41.
22. G.J. Germann, S.R. Cohen, G. Neubauer, G.M. McClelland, H. Seki, and D. Coulman, Atomic scale friction of a diamond tip on diamond (100) and (111) surfaces. *Journal of Applied Physics* **1993**, 73(1), 163-167.
23. R. Bennewitz, T. Gyalog, M. Guggisberg, M. Bammerlin, E. Meyer, and H. Güntherodt, Atomic-scale stick-slip processes on Cu (111). *Physical Review B* **1999**, 60, 11301-11304.

24. Q. Li, Y. Dong, D. Perez, A. Martini, and R.W. Carpick, Speed dependence of atomic stick-slip friction in optimally matched experiments and molecular dynamics simulations. *Physical Review Letters* **2011**, 106(12), 126101.
25. L. Howald, H. Haefke, R. Lüthi, E. Meyer, G. Gerth, H. Rudin, and H.J. Güntherodt, Ultrahigh-vacuum scanning force microscopy: Atomic-scale resolution at monatomic cleavage steps. *Physical Review B* **1994**, 49(8), 5651-5656.
26. R. Lüthi, E. Meyer, M. Bammerlin, L. Howald, H. Haefke, T. Lehmann, C. Loppacher, H.J. Güntherodt, T. Gyalog, and H. Thomas, Friction on the atomic scale: An ultrahigh vacuum atomic force microscopy study on ionic crystals. *Journal of Vacuum Science & Technology B* **1996**, 14(2), 1280-1284.
27. R.W. Carpick, Q. Dai, D.F. Ogletree, and M. Salmeron, Friction force microscopy investigations of potassium halide surfaces in ultrahigh vacuum: structure, friction and surface modification. *Tribology Letters* **1998**, 5(1), 91-102.
28. G.A. Tomlinson, A molecular theory of friction. *Philosophical Magazine* **1929**, 7(46), 905-939.
29. L. Prandtl, Ein Gedankenmodell zur kinetischen Theorie der festen Körper. *Zeitschrift für Angewandte Mathematik und Mechanik* **1928**, 8(2), 85-106.
30. M. Weiss and F.-J. Elmer, Dry friction in the Frenkel-Kontorova-Tomlinson model: Static properties. *Physical Review B* **1996**, 53(11), 7539-7549.
31. M. Dienwiebel, G. Verhoeven, N. Pradeep, J. Frenken, J. Heimberg, and H. Zandbergen, Superlubricity of graphite. *Physical Review Letters* **2004**, 92(12), 126101.
32. G. Verhoeven, M. Dienwiebel, and J. Frenken, Model calculations of superlubricity of graphite. *Physical Review B* **2004**, 70(16),
33. B. Derjaguin, Friction and adhesion IV. The theory of adhesion of small particles. *Kolloid Zeits* **1934**, 69, 155-164.
34. K. Johnson, K. Kendall, and A. Roberts, Surface energy and the contact of elastic solids. *Proceedings of the Royal Society of London. A. Mathematical and Physical Sciences* **1971**, 324(1558), 301.
35. Y. Dong, X.Z. Liu, P. Egberts, Z. Ye, R.W. Carpick, and A. Martini, Correlation between probe shape and atomic friction peaks at graphite step edges. *Tribology Letters* **2012**,
36. C. Lee, Q. Li, W. Kalb, X.-Z. Liu, H. Berger, R.W. Carpick, and J. Hone, Frictional characteristics of atomically thin sheets. *Science* **2010**, 328(5974), 76.

37. G. Gao, R.J. Cannara, R.W. Carpick, and J.A. Harrison, Atomic-scale friction on diamond: a comparison of different sliding directions on (001) and (111) surfaces using MD and AFM. *Langmuir* **2007**, 23(10), 5394-5405.
38. V. Hegadekatte, N. Huber, and O. Kraft, Finite element based simulation of dry sliding wear. *Modelling and Simulation in Materials Science and Engineering* **2005**, 13(1), 57-75.
39. R.L. Jackson and I. Green, A finite element study of elasto-plastic hemispherical contact against a rigid flat. *Journal of Tribology* **2005**, 127(2), 343-354.
40. Y. Song and B. Bhushan, Simulation of dynamic modes of atomic force microscopy using a 3D finite element model. *Ultramicroscopy* **2006**, 106(8–9), 847-873.
41. B. Bhushan, Contact mechanics of rough surfaces in tribology: multiple asperity contact. *Tribology Letters* **1998**, 4(1), 1-35.
42. Q. Li, T.E. Tullis, D. Goldsby, and R.W. Carpick, Frictional ageing from interfacial bonding and the origins of rate and state friction. *Nature* **2011**, 480(7376), 233-236.
43. M. Mishra, P. Egberts, R. Bennewitz, and I. Szlufarska, Friction model for single-asperity elastic-plastic contacts. *Physical Review B* **2012**, 86(4),
44. B. Luan and M.O. Robbins, The breakdown of continuum models for mechanical contacts. *Nature* **2005**, 435(7044), 929-932.
45. Y. Mo, K.T. Turner, and I. Szlufarska, Friction laws at the nanoscale. *Nature* **2009**, 457(7233), 1116-9.
46. K. Falk, F. Sedlmeier, L. Joly, R.R. Netz, and L. Bocquet, Molecular origin of fast water transport in carbon nanotube membranes: superlubricity versus curvature dependent friction. *Nano Letters* **2010**, 10(10), 4067-73.
47. Y. Dong, Q. Li, and A. Martini, Molecular dynamics simulation of atomic friction: A review and guide. *Journal of Vacuum Science & Technology A: Vacuum, Surfaces, and Films* **2013**, 31(3), 030801.

Chapter 3: Experimental Techniques and Setup

Due to the multidisciplinary nature of nanotribology, the studies presented in this thesis involve the employment of multiple instruments to perform nanotribological tests and characterization. The key instruments, including an atomic force microscope (AFM), a Raman spectrometer, and a transmission electron microscope (TEM) are described within this Chapter, as well as AFM force calibration details.

3.1.1: Atomic Force Microscopy

Atomic force microscopy (AFM) [1] was invented by Binnig *et al.*, shortly after winning the Nobel Prize for the invention of scanning tunneling microscopy (STM) in 1986 [2]. Unlike STM, which was capable of imaging of atomic-scale features of only electrically conductive samples, an AFM can achieve the same performance on both conductors and insulators while also measuring the tip-sample forces. The original AFM incorporated a STM tip as sensing mechanism [1] and thus was only sensitive to forces perpendicular to the sample surface. Later, Mate *et al.* expanded the AFM to measure both normal and lateral forces using optical interferometry as a bi-axial sensing mechanism [3].

Since then, Mate's design had proven to be highly valuable to nanotribologists. A sharp AFM tip can be considered to represent a nanoscale asperity; this is substantially easier to analyze than the complex, multi-asperity contacts typically encountered in macroscale sliding experiments. Marti *et al.* developed a design that uses a four-quadrant photo-sensitive diode (PSD) that was based on Meyer *et al.*'s PSD-based normal force detection system [4]. This allowed both normal and lateral forces to be simultaneously

recorded in a convenient way [5]. Currently, this optical beam deflection method is found in most AFM's. A schematic view of Marti's design is shown in Figure 3.1 (a).

An AFM is capable of measuring several physical quantities at ultrahigh resolution: sub-nanometer normal and lateral displacements of the cantilever, sub-nanonewton forces exerting on the tip, sub-millivolt voltages in terms of the work function difference between the tip and sample, and sub-nanoamp electrical currents through the tip-sample contact. In modern commercial AFM's, the force sensing device is an ultra-sharp microfabricated probe tip attached to the free end of a flexible cantilever that mechanically amplifies tip-surface interaction forces. These microfabricated tips typically have a radius of curvature of $\lesssim$10 nm, as shown in Figure 3.1 (b). High-precision sample translation in the *x*, *y*, and *z*-directions are generated by piezoelectric scanners that allow the tip to move laterally and vertically with respect to the sample. During scanning, the interacting atomic forces between the tip and the sample surface cause the cantilever to bend and deflect. The cantilever will bend vertically from its equilibrium position as a result of attractive or repulsive force in the normal direction, and will twist laterally from its equilibrium position as a result of the lateral friction force; this mechanism is shown in Figure 3.1 (c). This thesis only deals with contact-mode AFM which simultaneously monitors normal forces and records lateral forces, *i.e.* during the scan, the AFM electronics maintain a constant normal force for their feedback loop by pressing the tip against the sample while the PSD records the lateral signal.

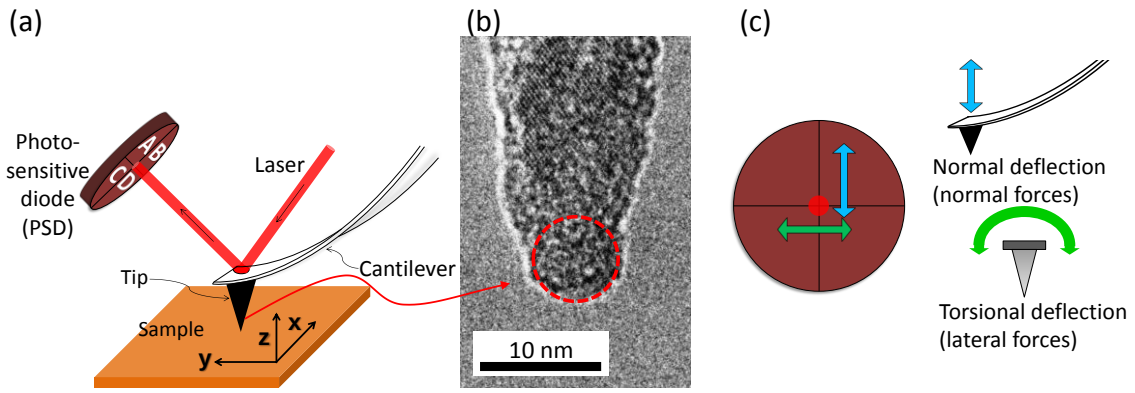

Figure 3.1: (a) Schematic setup of an AFM. A rectangular microfabricated cantilever scans across the sample surface; the cantilever deflection is recorded by a laser beam that is reflected from the backside of the cantilever to the four-quadrant photo-sensitive diode (PSD). (b) A representative TEM image of an unused contact-mode silicon tip. In the center, the silicon lattice is resolved, revealing the crystalline structure which is covered by a native, amorphous silicon oxide layer of a few nanometers thickness. The red dash circle was fit to estimate the tip radius of ~4-5 nm in this case. (c) A PSD is used to simultaneously monitor the normal and torsional motion of the cantilever. Detection of forces is through the laser displacement: normal displacement of the laser corresponds to the cantilever bending normal to the surface due to normal forces; lateral displacement of the laser is due the cantilever twisting in response to lateral/friction forces.

In all commercial AFM's, the cantilever long axis is not parallel to the sample surface, but rather has a finite tilt angle. The rationale for this tilt is to prevent the cantilever and the probe chip from touching the sample surface during scanning, which can be problematic for samples with out-of-plane features similar to or exceeding the tip height (~15 μm). Another reason for this tilt is to minimize interferometric effects of the laser reflection from the backside of the cantilever and the reflection from the sample

surface. However, the presence of the cantilever tilt angle causes a slight longitudinal tip displacement along the cantilever long axis upon tip-sample contact with an increased applied load of the cantilever [6]. This issue is particularly important when performing force-distance spectroscopy, to be discussed in Section 3.2, or when varying the applied normal force during a friction measurement. The slight tip displacement is undesirable, but it can be minimized by tilt angle compensation proposed by Cannara *et al.*, which involves moving the *y*-piezo by a small fraction of the *z*-piezo displacement [6]. The definitions for *x*, *y*, and *z* are given in Figure 3.1 (a).

3.1.2: AFM Friction Force Microscopy: Atomic Stick-Slip and Contact Stiffness

One of the most important modes of AFM that is utilized for our studies is the measurement of lateral forces[1]. When a tip scans across a flat homogenous surface at a constant normal force, a uniform lateral signal can be observed in both forward and backward directions. While the AFM tip rasters over a surface, data (surface topography, applied normal force, and lateral forces) are recorded at a certain resolution, *e.g.* 512×512 elements, *i.e.* 512 points in the *x*-direction and 512 lines in the *y*-direction, and stored in a matrix. The recorded matrix is then used to construct a 2-D or 3-D image. A typical example of a silicon tip scanning on a heterogeneous sample is shown in Figure 3.2 (a). This sample consists of a single-layer graphene (area A) deposited on a SiO_2 substrate

[1] This mode of AFM for measuring lateral forces is often referred to as friction force microscopy (FFM) or lateral force microscopy (LFM). In this thesis no distinction is made among them and AFM, and the terminology is used interchangeably.

(area B). The hysteresis loop, as shown in Figure 3.2 (b), enclosed by the forward and backward lateral signals is called a friction loop. The friction force is computed from

$$F_f = \frac{F_{\mathrm{L,fwd}} - F_{\mathrm{L,bwd}}}{2}, \tag{3.1}$$

where $F_{\mathrm{L,fwd}}$ and $F_{\mathrm{L,bwd}}$ denote the lateral force in the forward and backward directions, respectively. Since the gap of the friction loop represents the friction force magnitude, hence material A is exhibiting a lower friction force than material B.

As discussed in Section 2.1.2, when a tip scans over a crystalline surface the lateral force typically exhibits a periodic stick-slip pattern. For example, Figure 3.2 (c) shows a 2-D lateral force image recorded when a sharp AFM silicon tip is scanned over an ultra-clean surface of muscovite mica in a dry nitrogen environment. A regular three-fold symmetric lattice is observed. A typical line scan from the image shows that the friction loop exhibits a saw-tooth pattern in the forward and backward scan directions, as shown in Figure 3.2 (d). From such a stick-slip friction loop, a number of important physical parameters can be extracted. First, the mean friction force can be calculated in the manner given in Equation 3.1; the maximum lateral force (the force at which slip occurs, which is the static force of friction) can also be determined. Second, when integrated over the scan distance and divided by the length scanned, one obtains the energy dissipation per unit length or unit cell of the material. Third, the underlying crystallinity, including the lattice spacing and crystallographic alignment, can be observed directly from the friction image. Lastly, the total lateral stiffness, denoted as k_{tot}, can be determined.

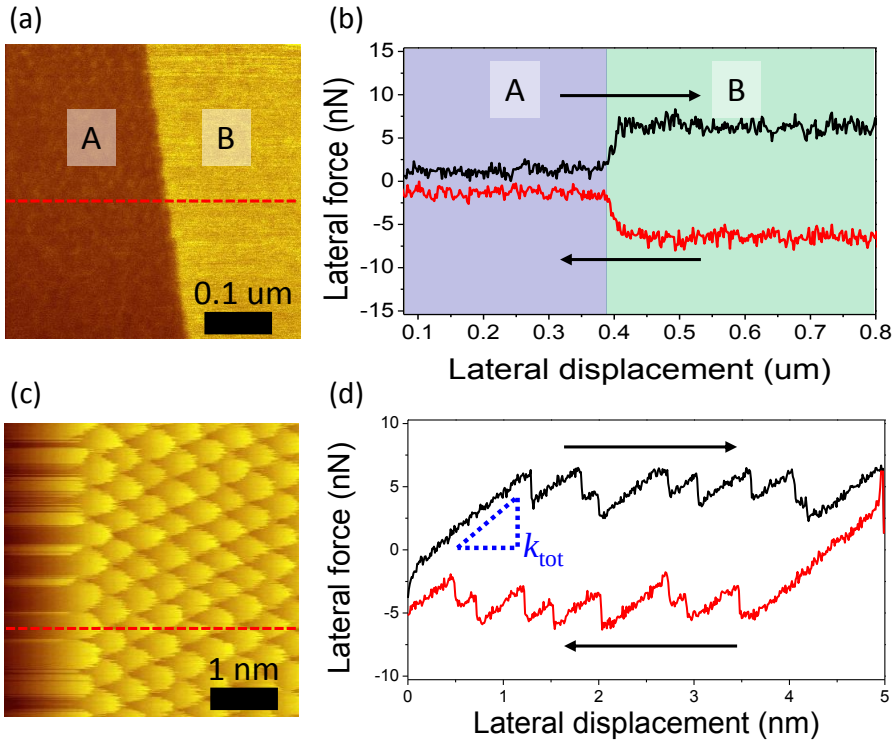

Figure 3.2: (a) A typical friction force image from a Si tip scanned over an area consisting of two materials, graphene on A and SiO_2 on B, which exhibit distinct frictional behaviors. The image is constructed from a 512×512 matrix of sampled points. Lower brightness corresponds to lower friction. (b) A typical friction loop taken from the red dash line in (a). Black arrows indicate the scan direction. Due to hysteresis, the forward and backward scans form a friction loop. Clearly, the gap of the loop at A is smaller than that at B. (c) A friction force image of a Si tip on clean muscovite mica surface, resolving an atomic stick-slip pattern. Three-fold symmetry can be observed from the image, which matches the symmetry and spacing of the sample's lattice. (d) A representative friction loop, where stick-slip pattern can be seen. The slope of the sticking phase corresponds to the total lateral stiffness k_{tot}.

The lattermost quantity is equal to the slope of the lateral force *vs.* displacement data during the sticking phase in the stick-slip friction traces, as indicated in Figure 3.2

(d). This quantity can be used to determine the lateral contact stiffness at the tip-sample interface using the following equation [7]

$$\frac{1}{k_{\mathrm{tot}}} = \frac{1}{k_{\mathrm{contact}}} + \frac{1}{k_L} + \frac{1}{k_{\mathrm{tip}}}, \tag{3.2}$$

where k_{contact} represents the lateral contact stiffness, k_L the lateral stiffness of the cantilever, and k_{tip} is the stiffness of the tip apex. The first experimental studies on the lateral contact stiffness were performed by Carpick *et al.* [7] and by Lantz *et al.* [8], independently from each other around the same time, and has been measured and evaluated in a number of other studies. The total lateral stiffness includes contributions from both the lateral stiffness of the tip-sample contact k_{conact}, the cantilever stiffness k_L, and the stiffness of the tip structure k_{tip}. In continuum theory, the lateral contact stiffness is related to the real contact area according to

$$k_{\mathrm{contact}} = 8G^* a_r \tag{3.3}$$

where G^* is the reduced shear modulus, given by $\frac{1}{G^*} = \frac{2-\nu_{\mathrm{sub}}}{G_{\mathrm{sub}}} + \frac{2-\nu_{\mathrm{tip}}}{G_{\mathrm{tip}}}$, and a_r the contact radius.

Experimentally, the value for k_{tot} for nanoscale contacts typically ranges between 1-10 N/m. Values in this range were observed in the present studies and also reported by multiple other previous studies [7-14]. Typical values of k_L for contact-mode AFM are usually much greater than k_{tot} (tens to hundreds of N/m). The stiffness of the tip has also been reported to be on the same order as k_L, implying that k_{contact} should also be on the order of 1 N/m, which was indeed reported Refs. [7] and [8]. In Chapter 6, the significance of k_{tot} will become clear as we discuss matching test parameters between experiments and simulations.

3.1.3: Brief Overview of AFM Instrumentation Used

Four AFM systems were employed in the studies presented in this thesis. The first is a Veeco Multimode AFM (formerly Veeco, now Bruker Inc., Santa Barbara, CA, USA), referred to as the Multimode AFM henceforth. The Multimode AFM can operate in either air or dry environment. The dry environment is achieved using a home-built hood, and the humidity can be maintained at ~2% relative humidity (RH) by purging the hood with nitrogen gas from a nitrogen gas cylinder (Airgas Inc., Malvern, PA, USA). The noise level of the scanner is minimized with the hood mounted while the entire AFM is secured on a vibration isolation air table. In the Multimode AFM, the cantilever has a tilt angle of 11°. The Multimode AFM is shown in Figure 3.3 (a).

Second, an Asylum Research MFP-3D AFM (Asylum, an Oxford Instrument Company, Santa Barbara, CA, USA), referred to as the Asylum AFM henceforth, was used in a dry nitrogen environment. The samples were placed inside a BioHeater Closed Fluid Cell from Asylum Research under relative humidity ~3% by purging the fluid cell with nitrogen gas obtained from the vapor of a liquid nitrogen dewar (Airgas Inc.). Two key advantages of the Asylum AFM is that the optical contrast is sufficiently high allowing for quick identification of samples (such as graphene and fluorinated graphene) and the large scan size of the scanner (100×100 μm^2). The noise level of the scanner is minimized by the closed hood while the entire AFM is secured on a vibration isolation air table. In the Asylum AFM, the cantilever has a tilt angle of 11°. The Asylum AFM is shown in Figure 3.3 (b).

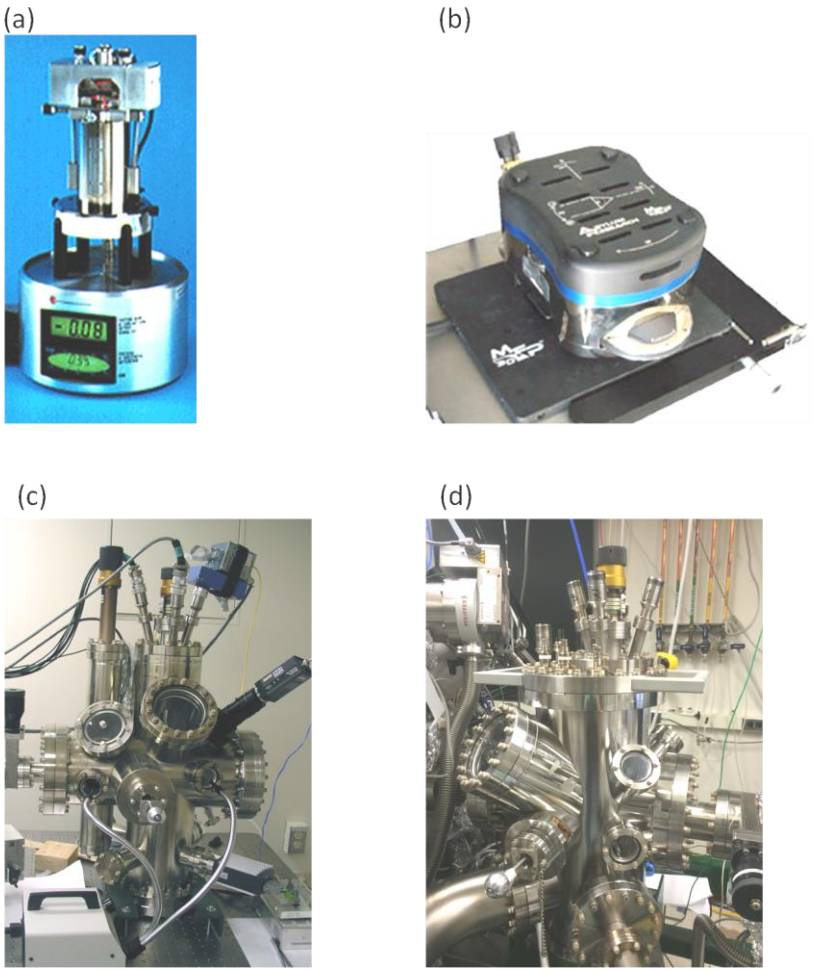

Figure 3.3: The work presented in this thesis is performed with four different AFM's. (a) Veeco Multimode AFM, (b) Asylum MFP-3D, (c) RHK 350 AFM, and (d) RHK 750 AFM.

Third is the RHK 350 AFM (RHK Technology Inc., Troy, MI, USA), referred to as the RHK 350 AFM henceforth. All measurements in this instrument were performed at <2% relative humidity by purging the chamber with N_2 obtained from the vapor of a liquid nitrogen dewar. The RHK 350 AFM has an extremely low noise level, which is achieved by the compact design of the scanner (the "Beetle-type" design first developed by Dai, *et al.* [15]) resulting in a relatively small mechanical loop; the sample stage is

located atop a stack of metal plates separated by Viton rubber for vibration damping, and the entire AFM is vibration-isolated by a table situated atop laminar-flow air legs. In the RHK 350 AFM, the cantilever has a tilt angle of 22.5°. The extremely low noise level allows us to resolve atomic stick-slip friction. The RHK 350 AFM is shown in Figure 3.3 (c).

Last is an ultra-high vacuum (UHV) RHK 750 AFM (RHK Technology Inc.), referred to as the RHK 750 AFM henceforth, operating at a base pressure of $\sim 6\times10^{-10}$ Torr. This low base pressure ensures an ultra-clean environment and minimizes the influence of sample surface contamination. The UHV pressure is also essential for matching experimental parameters with those of the simulations since the latter generally does not consider the presence of a surrounding gaseous environment. The RHK 750 AFM includes a fast entry load-lock chamber for exchanging samples from ambient conditions by independently venting and evacuating the chamber without breaking vacuum of the main chamber. The entire AFM, with a surface science apparatus attached to it, is bolted onto a steel frame supported by vibration isolation air legs to reduce external mechanical vibrations. The RHK 750 AFM scanner is identical to the one in RHK 350 AFM, therefore also capable of achieving atomic stick-slip resolution as well, although the overall signal-to-noise ratio is similar or lower than the RHK 350 AFM, possibly due to the presence of the surface science system and its mechanical vacuum pumps operating continuously. In the RHK 750 AFM, the cantilever also has a tilt angle of 22.5°.

The RHK 750 AFM by design allows for variable temperature experiments. For low temperatures, a built-in liquid helium cryostat (model RC-102 UHV, Cryo Industries

of America Inc., Manchester, NH, USA) is capable of cooling the sample down to approximately ~40 K. The cryostat is equipped with a silicon diode temperature sensor (DT-4XX series, LakeShore Cryotronics Inc., Westerville, OH, USA) located near the connection point between the cryostat and the AFM sample stage. A temperature controller (LakeShore 331, LakeShore Cryotronics Inc.) is connected to the temperature sensor allowing for real time temperature readout and logging. Note that due to the undesired thermal dissipation in the connection between the cryostat and the sample stage, the temperature at the sample has an offset of ~30 K above that of the cryostat. Finally, for elevated temperatures, specially designed samples holders are equipped with a tungsten filament below the sample, allowing the sample to be heated up to ~800 K using radiative heating. A K-type thermocouple is built in right below the sample, used for reading the more representative sample temperatures for both elevated and cryogenic temperatures. The RHK 750 AFM is shown in Figure 3.3 (d).

3.2: Force Distance Spectroscopy

Beyond its surfaces imaging and frictional tests at high resolution, an AFM can also serve as an important tool for nanoscale testing of mechanical properties of materials. In 1989, Burnham *et al.* pioneered the use of an AFM to measure mechanical properties of various materials as a function of tip-sample separation [16]. One specific mechanical testing operation modes is force distance (FD) spectroscopy, from which two important physical parameters can be obtained. The first is the measurement of the pull-off force (or the adhesion force) between the AFM tip and the sample; the second is the determination of the elastic properties of thin films and nanoscopic regions of samples.

As the adhesion force is a significant quantity in nanotribology, nowadays it is common to perform morphology, friction, and adhesion tests altogether.

A FD curve is the data recorded during a FD measurement. At the beginning of a FD test, while the tip-sample separation is large (also known as the out-of-contact state), there is no interaction between the tip and the sample, thus the cantilever is in its equilibrium state as it is not experiencing any interaction force. As the AFM scanner approaches the sample by extending the *z*-piezo on which the cantilever chip is mounted, the cantilever deflection is recorded simultaneously. This generates a plot of the normal force signal given by the cantilever deflection *vs.* vertical tip-sample displacement or distance (hence the name force-distance curves). A schematic of a FD curve is shown in Figure 3.4, taken for the simplest case of AFM. The green curve is the approaching portion (curve parts 1 and 2), and the black curve is the retraction portion (curve parts 3, 4, and 5). At the right side of the curve (curve parts 1 and 5), the scanner is fully retracted and far away from the sample, therefore no forces act on the tip. The cantilever is then in its undeflected state.

As the scanner further approaches the sample surface, the cantilever remains undeflected until the tip is brought close to the sample and experiences an attractive force. When the gradient of the attractive force exceeds the normal spring constant of the cantilever, there is a sudden jump associated with the snap-in of the tip, resulting in a sudden vertical jump in the FD curve. As the scanner continues moving toward the sample, the cantilever deflection increases. After reaching its full extension, the scanner starts to retract away from the surface and the cantilever deflection decreases. Due to adhesion between the tip and sample, the tip remains in contact with the surface causing a

tensile load on the tip. There is another sudden jump associated with the pull-off event when the gradient of the adhesive force reduction exceeds the cantilever's spring constant, corresponding the contact separation. The pull-off force is calculated based on the absolute force difference between the pull-off event and the equilibrium state.

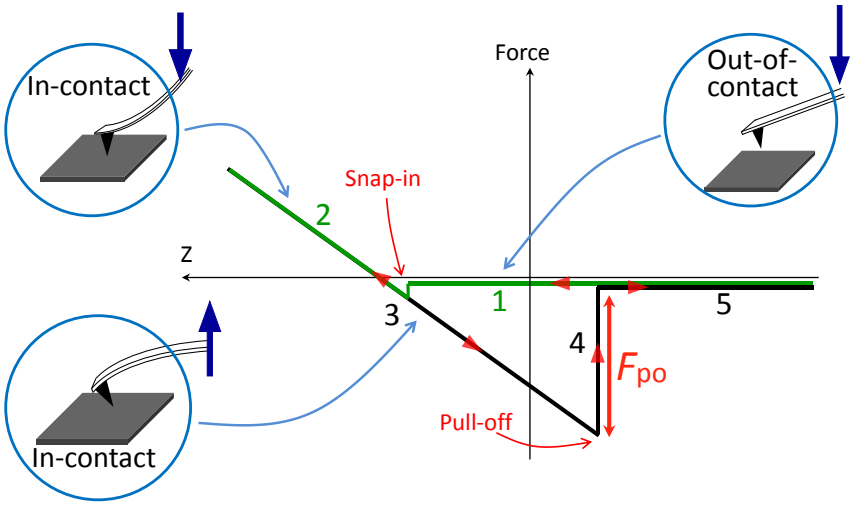

Figure 3.4: A typical force distance (FD) curve. Dark blue arrows indicate the direction of the AFM tip motion. The tip approaches the sample surface from a large tip-sample separation distance (out-of-contact state, curve part 1), and after the snap-in, the tip presses on the sample (in-contact state) while it pushes on the sample (curve part 2). This completes the approach part of the curve, plotted in green. After the approach, the tip retracts from the surface (curve part 3), and the tip remains in contact with the surface until the pull-off event occurs (curve part 4), and separates from the sample (curve part 5), plotted in black.

Eventually the scanner retracts far enough in the direction away from the surface such that the cantilever returns to its undeflected state. In the linear region of the FD curve (in-contact portion), the slope represents the signal sensitivity of the PSD and will be used for force calibration procedures, to be discussed in Section 3.3. When the

cantilever stiffness is much greater than that of the specimen, the slope is related to the elastic modulus of the specimen and therefore material elastic properties can be extracted [17]. On the other side of the spectrum, when the stiffness of the surface is greater than that of the cantilever, a typical FD curve as shown in Figure 3.5 can be observed. The data was acquired on a graphite sample. In such cases, at all points on the curve while the tip is in contact with the surface, the force changes linearly with displacement. From the FD curve, it is possible to calculate the work of adhesion from the contact mechanics models introduced in Section 2.2. Specifically, the work of adhesion W is related to the adhesion force F_{adh} by $F_{\text{adh,DMT}} = -2\pi RW$ and $F_{\text{adh,JKR}} = -\frac{3}{2}\pi RW$, for DMT and JKR regimes, respectively, assuming R is measured independently. Furthermore, if the work of adhesion for a pair of the materials is known, either from the literature or *in-situ* measurements [18], one can independently calculate the radius of an AFM tip R by measuring the adhesion force F_{adh} between that material pair and taking into account the proper contact mechanics model.

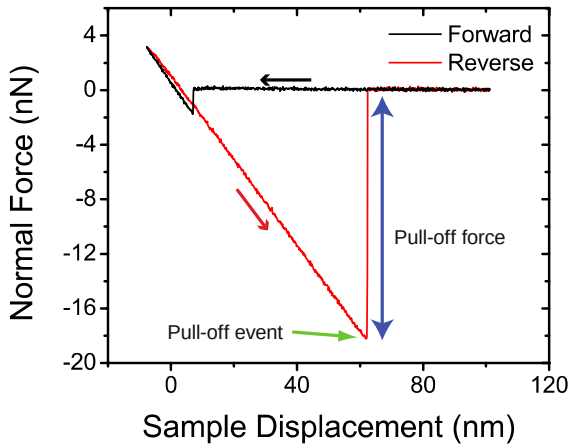

Figure 3.5: A typical FD curve measured in a direct pull-off measurement on graphite. The blue arrow indicates the magnitude of the pull-off force; the green arrow indicates the pull-off event. The pull-off force measured in this graph corresponds to ~18 nN.

3.3: Force Calibration of AFM Cantilevers

A full quantitative study by means of AFM is not possible without careful force calibration of the AFM cantilever. Regardless of the operation mode or detection method used, the measured signals, which are usually a voltage or a current, must be accurately calibrated to obtain forces. Therefore, cantilever force calibration is a key requirement to conduct accurate AFM studies. For commercial cantilevers, manufacturers often provide force constants that are highly inaccurate, making it necessary for the user to carry out a proper calibration procedure for each cantilever. Although many calibration methods have been introduced starting from the early development of AFM, no single method has been established as the primary standard. Here we discuss common methods that were used in the present studies.

3.3.1: Normal Force Calibration

For normal force calibration, a commonly employed calibration method is the Sader method[2] [19]. In this method, the normal force constant k_n is calculated from the measurement of the cantilever resonance frequency f_0 and quality factor Q_f in a medium such as air or dry nitrogen, with the knowledge of its planar view dimensions (lateral dimensions) of the cantilever beam. With a regular optical microscope (Olympus BX 51, Olympus Inc., Tokyo, Japan), the cantilever lateral dimensions can be rather accurately determined. The measurement of $f_{0,\mathrm{n}}$ and Q_n can be performed in most AFM systems by monitoring the cantilever thermal noise spectrum or by deliberately exciting the cantilever. The force constant k_n is given by

$$k_n = 0.1906\rho_f b^2 l Q_n \Gamma_i^n(f_{0,\mathrm{n}}) f_{0,\mathrm{n}}^2 \qquad (3.4)$$

where ρ_f is the density of the medium, b the cantilever width, l the length, and Γ_i^n the imaginary component of the hydrodynamic function, which depends on the Reynolds number, $\mathrm{Re} = \rho_f f_{0,\mathrm{n}} b^2/4\eta$, where η is the viscosity of the medium. For common rectangluar single-beam cantilevers, this method is reliable, and combined with an accurate $f_{0,\mathrm{n}}$ and Q_n, the uncertainty can be as low as ~5% [19].

However, in the absence of a vicous medium (and thus in the case of extremely low cantilever damping, such as the case for UHV conditions), the Sader method cannot be applied. In this case, the geometrical method needs to be used instead for obtaining the normal spring constant according to the beam equation for the normal stiffness [20]

$$k_n = \frac{Ewt^3}{4l^3}. \qquad (3.5)$$

[2] For convenience, Sader *et al.* have also created this online calibration applet: http://www.ampc.ms.unimelb.edu.au/afm/calibration.html

Here, E is the Young's modulus of the cantilever material; w, t, and l are the width, thickness, and length of the cantilever, respectively. Similar to the Sader method, the cantilever planar dimensions can be easily obtained from optical microscopy microscopy or manufacturer's specifications. However, the cantilever thickness can vary significantly over cantilevers even of the same type. Also the thickness can vary along direction of the cantilever's long axis. As evident from Equation 3.5, the thickness has a strong effect on the normal stiffness because it shows up raised to the third power. To account for this, one either can use electron microscopy to measure the thickness, or calculate the thickness from the first normal resonance frequency $f_{0,n}$ of the cantilever in UHV conditions according to the following equation [20]

$$t = \frac{4\sqrt{3}\pi l^2}{1.873^2} f_{0,n}\sqrt{\frac{\rho}{E}}, \tag{3.6}$$

where ρ is the material density of the cantilever. Filleter has shown that the geometrical method consistently gives a force constant that is about 17% lower than the Sader method [21], although the cause for the deviation remains unclear.

The sensitivity of the photodetector S, which is needed to convert measured readout volts to nanometers of cantilever deflection, was determined by measuring the slope of the cantilever deflection signal in a FD curve, as discussed in Section 3.2. The inverse slope of the curve is given in a unit of nm/V. The normal force F_n can then be calculated by the equation

$$F_n = k_n S V_{\mathrm{a-b}} \tag{3.7}$$

where $V_{\mathrm{a\text{-}b}}$ is the PSD normal voltage signal that one records.

3.3.2: Lateral Force Calibration

There exist several methods for lateral force calibration. In this thesis, we have used three different lateral force calibration methods: (1) The Sader method for torsional force calibration [22]; (2) the geometrical method for lateral calibration [20]; and (3) the diamagnetic lateral force calibration (D-FLC) method [23]. The choice for a particular method is made depending on the specific instrumental limitations.

The torsional Sader method is derived in an analogous manner to the normal Sader method, and thus similarly makes the assumption that the length of the rectangular cantilever beam is much greater than the width, which in turn is much greater than the beam thickness. It involves determining the natural torsional resonance frequency and the corresponding quality factor in a given medium, often in air or dry nitrogen. Using optical microscopy, the planar view dimensions of the cantielver are determined. Knowing those parameters, one calculates the torsional stiffness k_{φ} according to the equation

$$k_{\varphi} = 0.1592\rho_f b^4 l Q_t f_t^2 \Gamma_i^t(f_t) \qquad (3.8)$$

where ρ_f is the density of the fluid, b and l the width and length of the cantilever, respectively; Q_t the torsional quality factor, f_t the torsional resonance frequencey, and finally the Γ_i^t is the imaginary part of the hydrodynamic fuction. With a measurement of the tip height, which can be obtained from electron microscopy, the lateral stiffness k_{φ} can then be calculated [22].

For the geometrical method for lateral calibration, the following equation is used to relate the rectangular cantilever dimensions to the torsional stiffness:

$$k_{\varphi} = \frac{Gwt^3}{3lh^2}\,. \tag{3.9}$$

Here, G is the shear modulus of the cantilever material, h is height of the tip that is attached to the end of the cantilever.

Silicon contact mode cantilevers were used for all results presented in this thesis. The following elastic properties of silicon are used consistently: E = 169 GPa, and ρ = 2.33×10^3 kg/m^3, and G = 68 GPa for the <110> direction, for the beam geometry calibration [20, 24]. Optical microscopy is used to determine the planar dimensions of the cantilevers; electron microscopy was used to measure the tip height. Filleter showed that the geometrical method consistently gives a force constant that is about 10% higher than the Sader lateral method [21], and the cause for the deviation remains unclear.

Lastly, the D-LFC method makes use of a home-built calibration setup consisting of a diamagnetic pyrolytic graphite (PG) sheet levitating atop four strong NdFeB magnets. The PG sheet (~5×5×0.5 mm^3) acts as a spring vibrating laterally. Moreover, due to the low air and eddy-current damping, the spring constant of the calibrator was accurately predetermined by measuring the sheet's natural vibration frequency. This natural vibration frequency can be accurately measured with a high-speed camera (Micro eX1, Vision Research Inc., Wayne, NJ) at a frame rate of 1 kHz. Using MATLAB, the motion of the floating graphite can be traced and fit to a damped sinusoidal oscillation, allowing extraction of the natural frequency of the graphite.

After the pre-calibration of the D-FLC device, it can then can be used to calibrate cantilevers. To this end, it is sufficient to do a regular AFM measurement on a clean muscotive mica specimen glued onto the PG sheet with the calibrator being the spring

system. During the scan, the floating PG sheet including the muscotive mica will move laterally relative to the magnets mounted on the AFM sample base. In this method, as the scanner is moving, the PG sheet undergoes a lateral displacement from which we evaluate the shearing force. This force causes a torsional deflection in the cantilever. By measuring the lateral output from the PSD as response to that cantilever twisting, and using the force evaluated, the cantilever lateral spring constant is calibrated. The important advantages of this method in comparison to other methods are that it does not rely on the knowledge of the lateral optical senstivity and the tip height.

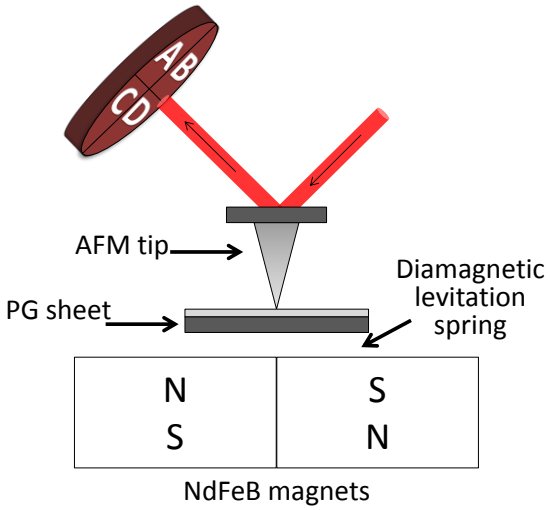

Figure 3.6: Schematic view of the D-LFC setup. Note here the design of the AFM. During the calibration, the AFM tip and the PG sheet are moving together with respect to the magnets.

Due to the design limitions imposed by the design of the RHK AFM's, a special holder needed to be designed to render it compatible with those AFM[3]. The most important limitation is due to the fact that the scanner head needs to rotate in order to do

[3] The RHK AFM-compatible D-LFC setup was designed and built in collaboration Mr. Qizhan Tam (an undergraduate student the Department of Mechanical Engineering and Applied Mechanics, University of Pennsylvania), by closely following the original design described in Ref. [21].

tip approach, which means that the D-LFC needs to be able to also rotate in the in-plane direction to retain the required scan angle of the tip with respect to the graphite specimen (along the principal diagonals). This is achieved with a custom-designed aluminum fixture to hold the D-LFC setup. The fixture has a thin handle allowing for rotating the fixture without perturbing the entire sample holder and thus the scanner head. Additionally, an aluminum safety cap is designed to protect the levitating graphite from falling off the magnets during mounting and unmounting the setup, as well as during introducing the D-LFC into the chamber. The major components are shown in Figure 3.7 along with a photograph of the entire setup in the AFM chamber when ready for calibration.

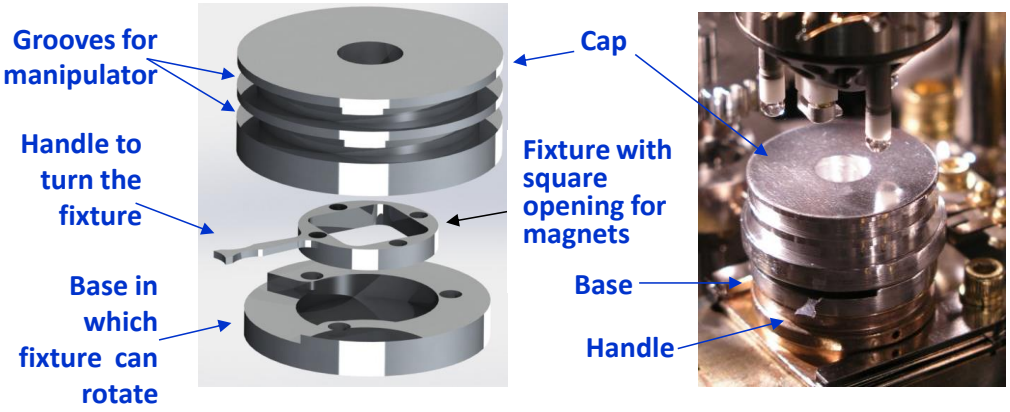

Figure 3.7: Left: Schematic view of the holder for the D-LFC setup specially designed to ensure compatibility with the RHK AFM's. Right: Optical image of the setup mounted into a RHK specimen holder inside the RHK AFM.

For all lateral force calibrations, with the exception of the D-LFC method, the sensitivity of the quadrant detector is assumed to be the same as the normal sensitivity [20]. The lateral force F_L can then be calculated by the equation:

$$F_L = k_L S V_{\mathrm{c-d}} \tag{3.10}$$

where $V_{\text{c-d}}$ is the PSD lateral signal that one records. Note that for the cases of torsional Sader method or the lateral geometric method, one needs to convert k_φ to k_L to account for the fact that lateral twisting occurs at the tip end, this is achieved according to the equation

$$k_L = \frac{3h}{2l} k_\varphi \tag{3.11}$$

where h denotes the tip height and l the cantilever length.

3.4: Raman Spectroscopy

Raman spectroscopy was invented by C.V. Raman in his Nobel Prize-winning discovery in 1928 [25]. It has been recognized as a valuable spectroscopy technique ever since. Raman spectroscopy is based on inelastic light scattering or the "Raman effect", initially observed in molecular liquids [25]. When a laser (or other intense monochromatic light sources) is irradiated, most of the light is scattered by the sample at the same wavelength as that of the incident light source. This process is known as Rayleigh scattering. However, a small proportion of the incoming light (~1:10^7) is scattered at a wavelength shifted from the original wavelength. The shift from the original wavelength is due to interactions of the light with excited states of the molecules/atoms in the material, leading to inelastic scattering. This effect is therefore referred to as inelastic light scattering. Specifically, if the scattered light is up-shifted from the initial state, the effect is called Stokes scattering; conversely, if the scattered light is down-shifted, then the effect is called anti-Stokes scattering. The energy difference between the incident and scattered photons correspond to internal energy

levels. Depending on the nature of the material under investigation, those levels correspond to vibrational, rotational, electronic, excitonic, and phononic modes etc [26]. The effects of Stokes and anti-Stokes scattering are schematically shown in Figure 3.8.

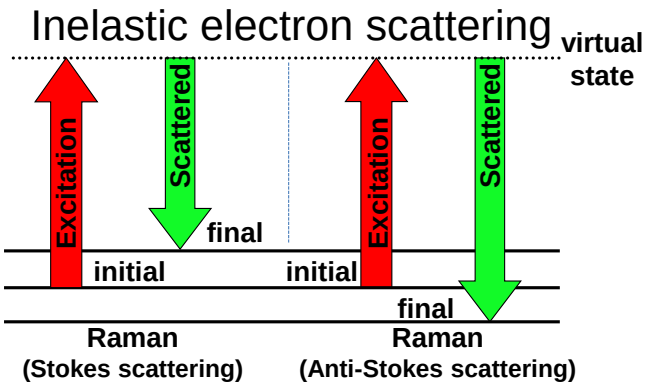

Figure 3.8: Two types of inelastic electron scattering. Left: the final scattered state has a higher energy than the initial state (Stokes scattering); Right: the final state has a lower energy state (anti-Stokes scattering).

In recent years, Raman spectroscopy has become a critical tool in studying carbon materials [27]. Ferrari *et al.* were the first to explore Raman spectroscopy for studying graphene [28] and demonstrated that graphene samples with different numbers of layers have distinct spectra, and therefore can be used in determination of layer thickness of graphene in a fast and non-destructive manner. A typical Raman spectrum on either graphene or graphite has two major vibrational modes: the E_{2g} and A_{1g} modes, corresponding to stretching and breathing mode of the carbon hexagonal network, respectively, as shown in Figure 3.9 (a). Those two modes result in three major peaks in the Raman spectrum obtained on graphite or graphene: the G and 2D peaks at 1580 cm^{-1}

and 2670 cm^{-1}, respectively. A typical Raman spectrum on the center of a single layer graphene flake is shown in Figure 3.9 (b).

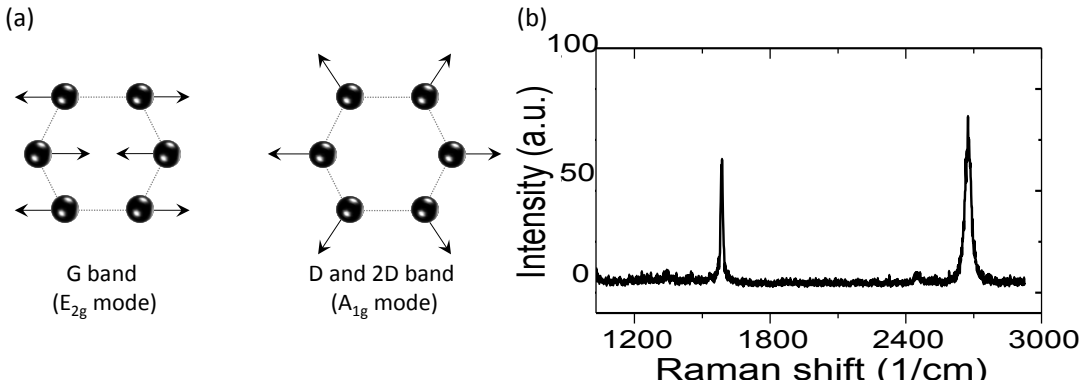

Figure 3.9: (a) Vibrational modes of carbon atoms (black spheres) in a graphene/graphite network. The case on the left corresponds to E_{2g} mode, or the 'stretching mode'; and the right case represents the A_{1g} mode, or the 'breathing mode'. (b) A typical Raman spectrum on a single-layer graphene, with the G and 2D peaks at ~1580 cm^{-1} and ~2700 cm^{-1}.

Notice that in the presence of defects (holes, edges, other atom species than carbon, or amorphization) in the graphene, an additional peak, termed the D peak, will appear at around ~1300 cm^{-1}. For graphene studies, this peak is therefore often utilized in studying defects. The Raman spectrometer used for our work is NT-MDT Ntegra, as shown in Figure 3.10. A 532 nm excitation laser is used and only signals from Stokes scattering are recorded and analyzed. A Peltier-cooled CCD detector (Andor Technologies Inc., an Oxford Instruments company, Belfast, UK) with 1024×256 pixels was operated at -55 °C.

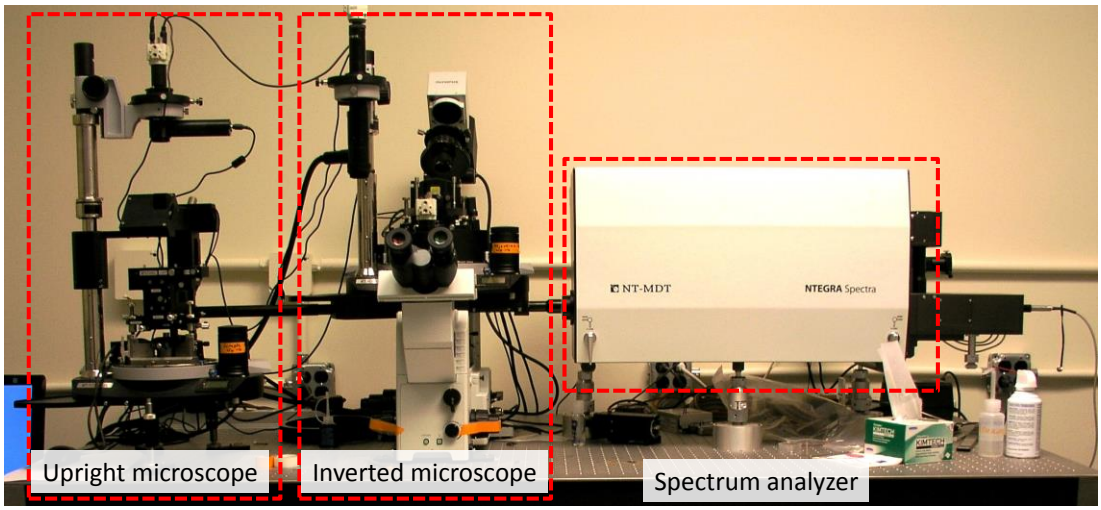

Figure 3.10: Results from Raman spectroscopy presented in the thesis are acquired with a NT-MDT Integra Raman spectrometer. The key components of the spectrometer are indicated, from left to right: upright microscope, inverted microscope allowing for bottom illumination of the Raman laser, and finally the spectrum analyzer. The entire spectrometer is resting on an air table to reduce mechanical noise when the sample is moved with respect to the laser beam for recording a Raman map.

3.5: TEM for Examining the AFM Tip Shape and Tip Radius

While AFM is an extremely useful and the primary tool for tribological tests, it does not allow direct examination of the tip shape, or even the ability to directly measure the tip radius. As mentioned earlier, the latter is an important quantity because, for example, it is needed to apply continuum contact mechanics models for further analyses. Therefore, TEM needs to be utilized to provide additional information about the tip, which can reveal change or wear of the tip apex due during scanning [29]. The process of examining the tip after scanning is called *post-mortem* TEM. It is also necessary to do *pre-mortem* TEM, *i.e.*, examining the tip before scanning, since tip dimensions can

deviate significantly from the manufacturer's specifications and from tip to tip. The TEM is specifically used in the studies on the thermal activation of atomic stick-slip friction, where experiments and simulations are combined by matching their test parameters, more on this in Chapter 6.

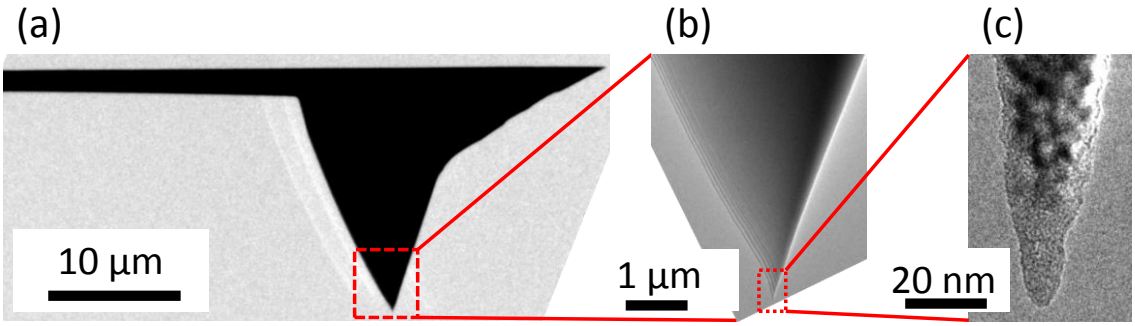

Figure 3.11: (a) Tip profile of a Si AFM tip; the probe chip (not shown) is located beyond the far left of the image. (b) A zoomed-in image of the tip shank. The typical fringes are due to the variation in the thickness of the shank. (c) A high-resolution TEM image of the tip apex where Si crystal lattice can be resolved. The tip is terminated by a thin amorphous silicon oxide layer.

The combined *pre-* and *post-mortem* TEM images allow us to carefully compare and thus better understand the sliding mechanisms of AFM scans. Additionally, TEM imaging is critical calculating the work of adhesion, as discussed in Section 3.2. Specifically, one can use a tip to measure the adhesion force between the tip material and a sample; then from *post-mortem* TEM imaging the tip radius can be calculated. After choosing the appropriate contact mechanics model based on the material properties, the work of adhesion between the tip material and the substrate can also be determined. Note that for the tip radius determination, the intrinsic cantilever tip tilt angle is properly taken into account. Lastly, for matching with simulations, every experimental parameter needs

to be determined as best as one can, allowing simulations to create same test conditions and making the comparison between the experimental and simulation results reliable.

AFM probe tip profiles are acquired using a special home-built tip holder compatible with the specific TEM instrument that was used [30, 31]. Figure 3.11 shows a typical series of images obtained using TEM. The novel holder was used to ensure repeatable imaging of probe tip profiles and is capable of mounting up to three probe chips at a session, and therefore increasing imaging throughput. Due to the intrinsic spatial limitations of the TEM and thus the corresponding probe holder design, only tip profiles along the long axis of the cantilever were examined. The TEM employed was a JEOL 2100 with a LaB_6 thermionic filament having a 0.25-nm point-to-point resolution. Image data were collected at 200 keV under high vacuum conditions at a base pressure of 10^{-8}-10^{-7} Torr. The JEOL 2100 TEM is shown in Figure 3.12.

Figure 3.12: The JEOL 2100 high-resolution TEM that was employed to investigate AFM tips.

3.6: References

1. G. Binnig, C.F. Quate, and C. Gerber, Atomic force microscope. *Physical Review Letters* **1986**, 56(9), 930-933.
2. G. Binnig and H. Rohrer, Scanning tunneling microscopy. *Surface Science* **1983**, 126(1), 236-244.
3. C.M. Mate, G.M. McClelland, R. Erlandsson, and S. Chiang, Atomic-scale friction of a tungsten tip on a graphite surface. *Physical Review Letters* **1987**, 59(17), 1942-1945.
4. G. Meyer and N.M. Amer, Simultaneous measurement of lateral and normal forces with an optical-beam-deflection atomic force microscope. *Applied Physics Letters* **1990**, 57(20), 2089.
5. O. Marti, J. Colchero, and J. Mlynek, Combined scanning force and friction microscopy of mica. *Nanotechnology* **1990**, 1(2), 141.
6. R.J. Cannara, M.J. Brukman, and R.W. Carpick, Cantilever tilt compensation for variable-load atomic force microscopy. *Review of Scientific Instruments* **2005**, 76, 053706.
7. R.W. Carpick, D.F. Ogletree, and M. Salmeron, Lateral stiffness: A new nanomechanical measurement for the determination of shear strengths with friction force microscopy. *Applied Physics Letters* **1997**, 70(12), 1548.
8. M.A. Lantz, S.J. O'Shea, A.C.F. Hoole, and M.E. Welland, Lateral stiffness of the tip and tip-sample contact in frictional force microscopy. *Applied Physics Letters* **1997**, 70(8), 970.
9. Q. Li, Y. Dong, D. Perez, A. Martini, and R.W. Carpick, Speed dependence of atomic stick-slip friction in optimally matched experiments and molecular dynamics simulations. *Physical Review Letters* **2011**, 106(12), 126101.
10. E. Gnecco, R. Bennewitz, T. Gyalog, C. Loppacher, M. Bammerlin, E. Meyer, and H. Güntherodt, Velocity dependence of atomic friction. *Physical Review Letters* **2000**, 84(6), 1172-1175.
11. S. Medyanik, W. Liu, I.-H. Sung, and R.W. Carpick, Predictions and observations of multiple slip modes in atomic-scale friction. *Physical Review Letters* **2006**, 97(13), 136106.

12. A. Socoliuc, R. Bennewitz, E. Gnecco, and E. Meyer, Transition from stick-slip to continuous sliding in atomic friction: entering a new regime of ultralow friction. *Physical Review Letters* **2004**, 92(13), 134301.
13. S. Maier, Y. Sang, T. Filleter, M. Grant, R. Bennewitz, E. Gnecco, and E. Meyer, Fluctuations and jump dynamics in atomic friction experiments. *Physical Review B* **2005**, 72(24), 245418.
14. E. Gnecco, R. Bennewitz, T. Gyalog, and E. Meyer, Friction experiments on the nanometre scale. *Journal of Physics: Condensed Matter* **2001**, 13, 619.
15. Q. Dai, R. Vollmer, R.W. Carpick, D.F. Ogletree, and M. Salmeron, A variable temperature ultrahigh vacuum atomic force microscope. *Review of Scientific Instruments* **1995**, 66(11), 5266-5271.
16. N.A. Burnham and R.J. Colton, Measuring the nanomechanical properties and surface forces of materials using an atomic force microscope. *Journal of Vacuum Science & Technology A: Vacuum, Surfaces, and Films* **1989**, 7(4), 2906-2913.
17. K.L. Johnson, *Contact Mechanics*; Cambridge University Press: Cambridge, UK, 1987.
18. T.D.B. Jacobs, K.E. Ryan, P.L. Keating, D.S. Grierson, J.A. Lefever, K.T. Turner, J.A. Harrison, and R.W. Carpick, The effect of atomic-scale roughness on the adhesion of nanoscale asperities: A combined simulation and experimental investigation. *Tribology Letters* **2013**, 50(1), 81-93.
19. J.E. Sader, J.W.M. Chon, and P. Mulvaney, Calibration of rectangular atomic force microscope cantilevers. *Review of Scientific Instruments* **1999**, 70, 3967.
20. E. Meyer, H.J. Hug, and R. Bennewitz, *Scanning Probe Microscopy: The Lab on a Tip*; Springer Verlag & Business Media: Heidelberg, 2004.
21. W.T.W. Filleter, *Nanometer-scale studies of friction, dissipation, and plasticity*, PhD Thesis, 2009, McGill University.
22. C.P. Green, H. Lioe, J.P. Cleveland, R. Proksch, P. Mulvaney, and J.E. Sader, Normal and torsional spring constants of atomic force microscope cantilevers. *Review of Scientific Instruments* **2004**, 75(6), 1988.
23. Q. Li, K.S. Kim, and A. Rydberg, Lateral force calibration of an atomic force microscope with a diamagnetic levitation spring system. *Review of Scientific Instruments* **2006**, 77(6), 065105.
24. M.A. Hopcroft, W.D. Nix, and T.W. Kenny, What is the Young's modulus of silicon? *Journal of Microelectromechanical Systems* **2010**, 19(2), 229-238.

25. C.V. Raman and K. Krishnan, A new type of secondary radiation. *Nature* **1928**, 121(3048), 501-502.
26. D.A. Long, *The Raman Effect: A Unified Treatment of the Theory of Raman Scattering by Molecules*; John Wiley & Sons, Ltd: West Sussex, England, 2002.
27. A.C. Ferrari and J. Robertson, Raman spectroscopy of amorphous, nanostructured, diamond–like carbon, and nanodiamond. *Philosophical Transactions of the Royal Society of London. Series A: Mathematical, Physical and Engineering Sciences* **2004**, 362(1824), 2477-2512.
28. A.C. Ferrari, J.C. Meyer, V. Scardaci, C. Casiraghi, M. Lazzeri, F. Mauri, S. Piscanec, D. Jiang, K.S. Novoselov, S. Roth, and A.K. Geim, Raman spectrum of graphene and graphene layers. *Physical Review Letters* **2006**, 97(18), 187401.
29. T.D.B. Jacobs and R.W. Carpick, Nanoscale wear as a stress-assisted chemical reaction. *Nature Nanotechnology* **2013**, 8(2), 108-112.
30. T.D.B. Jacobs, *Imaging and understanding atomic-scale adhesion and wear: Quantitative investigations using in situ TEM*, PhD Thesis, 2013, University of Pennsylvania.
31. G.E. Wabiszewski, *Interrogation of single asperity electrical contacts using atomic force microscopy with application to nems logic switches*, PhD Thesis, 2013, University of Pennsylvania.

Chapter 4: Adhesion Properties of Few-Layer Graphene: The Effect of Sliding History on Adhesion

This Chapter presents results on the adhesion properties of few-layer graphene (FLG). Through these studies, we aim to gain better understanding of the effects which govern adhesion to graphene surfaces, and how those can affect contact area and friction during nanoscale sliding. This Chapter begins with an introduction to graphene, and then reviews previous friction and adhesion studies on graphene. Following the introduction, experimental details, including sample preparation and test protocols, are outlined. Subsequently, the results of these experiments and discussion of the results will be presented. The results in this Chapter have been partially published in Ref. [1].

4.1: Introduction and Prior Studies on Graphene Surface Energy and Adhesion

Graphene is currently one of the most well-studied examples of an isolated two-dimensional (2-D) material. Despite theoretical predictions of the electrical properties of graphene in 1947 [2], the first experimental sample was not discovered until 2004 [3]. The 2-D nature of graphene is given by the fact that it consists of single layers of carbon atoms that are arranged in a hexagonal pattern. Graphene sheets are covalently bonded in-plane, whereas the interlayer interactions are governed by much weaker van der Waals interactions. Since its discovery, graphene has attracted much attention because it possesses many superior electrical, thermal, and mechanical properties [3, 4]. The

potential of graphene is so well recognized that the Nobel Prize of Physics in 2010 was awarded to its discoverers "for groundbreaking experiments on graphene" [5].

Currently there exist a number of techniques to produce graphene, yielding various sizes, thicknesses, and quality. One of the most popular techniques is the mechanical exfoliation of graphene from bulk graphite, also known as the "Scotch tape" method [3], which is capable of producing high-quality single layer and few layer graphene. However, the flake sizes are typically limited to tens of micrometers laterally. Nevertheless, due to the high quality, this method is appealing for fundamental research and characterization. Another commonly used technique is chemical vapor deposition (CVD) [6], which typically results in more defects in the graphene than observed in the exfoliation method [3]. However, CVD graphene synthesis can routinely produce single-layer graphene at large scale, especially with the improving growth quality [7, 8], this route is most promising for mass production [9]. Another advantage of CVD graphene is that one can then transfer graphene onto a variety of substrates, allowing for chemically functionalizing the graphene [10-14]. Lastly, there are two other synthesis routes to form single graphene layers, including chemical synthesis [15, 16] and thermal decomposition/epitaxial growth [17]. These latter two methods of graphene synthesis were not used in producing any graphene samples used in this thesis, and are not discussed further.

There are a few studies of the mechanical and tribological properties of graphene, but these studies demonstrate that graphene exhibits remarkable mechanical and tribological properties. For example, macroscale friction measurements of graphene prepared by various methods (*e.g.* CVD, exfoliated, and epitaxial graphene) showed a

friction coefficient lower than bulk graphite [18, 19], suggesting a possible application as a solid lubricant. At the nanoscale, Lee *et al.* reported exfoliated graphene as the strongest material ever measured [4], with the strength of CVD graphene is only slightly lower than that of exfoliated graphene [20]. Filleter *et al.* showed that a single layer of epitaxial graphene has higher friction than a bilayer [21]. This phenomenon was later also observed on other exfoliated 2-D materials by Lee *et al.* [22]. The monotonic decrease in friction from single to multiple layers was proposed to be a universal property of 2-D materials if the material is not strongly adhered to a supporting substrate [22]. This layer-dependent "strengthening" (an increase in friction force along the sliding direction, until a saturation level was reached) is proposed to be a result of a thin-film puckering effect: thinner atomic sheets are more susceptible to out-of-plane deformation than thicker sheets, resulting in out-of-plane deformation of graphene sheets around the tip due to tip-graphene adhesion and shear forces, leading to larger contact areas and thus higher friction [22], as shown in Figure 4.1. In a similar fashion, Egberts *et al.* investigated friction properties of CVD graphene and found that CVD graphene substantially lowers the friction force compared to the surrounding oxidized copper surface, and that the puckering effect, which previously had only been observed on exfoliated graphene, also occurs on CVD grown graphene. For graphite, Deng *et al.* [23] recently reported that exposing the surface to ambient air increases the interaction between the AFM tip and top graphite layer; correspondingly, the top layer adheres strongly to the tip and locally delaminates when the tip slides over it at a tensile load, leading to increased friction as the load is decreased (*i.e.* a negative friction coefficient). This study focused on frictional effects as opposed to the dependence of adhesion on sliding.

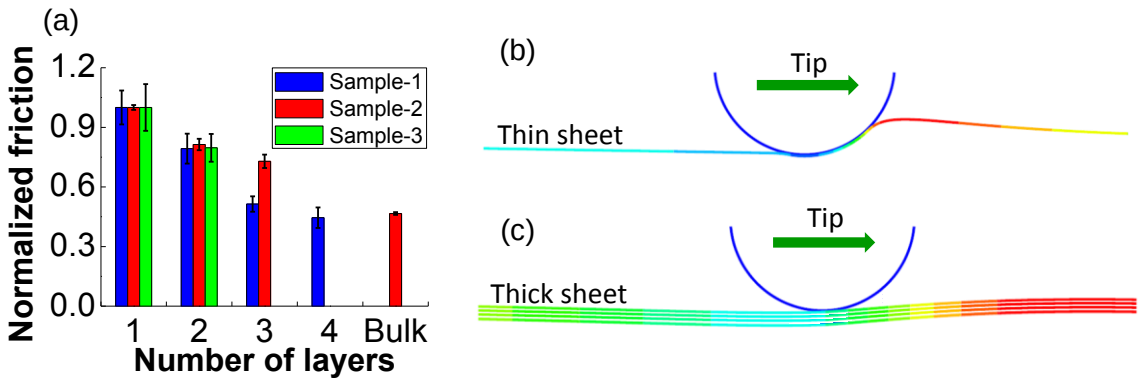

Figure 4.1: (a) Graphene friction *vs.* layer numbers. The magnitude of the forces is normalized to the value for the thinnest layer. (b) and (c) The proposed puckering effect. As the AFM tip slides over the graphene membrane (direction indicated by the green arrows), due to the low bending stiffness of thin graphene (b), the graphene deforms elastically in the out-of-plane due to shear and adhesion forces, resulting in an increased contact area in front of the tip (indicated by the color scale, red being the highest deflection height and blue the lowest). Images adapted from [22].

Despite these advances in understanding the trends observed for the friction response of graphene, results from recent studies on adhesion between graphene sheets and an interacting countersurface [24-27] have not produced clear trends (*e.g.,* as a function of the number of FLG layers) and specific mechanisms governing adhesion have not yet been described. Given that adhesion is important for many potential applications of graphene (*e.g.* as a protective coating, in thin-layer devices, or for reducing surface friction), a better understanding of the adhesion behavior of graphene is desirable. In devices that use graphene as an integrated part of the structure, one must consider three different interactions: interfacial adhesion between the graphene and its substrate; adhesion between a moving asperity (*e.g.* an AFM tip, or an asperity on a counter-

surface) and the graphene/substrate system; and for multilayer graphene films, the interaction between the graphene layers. To date, only a few studies have been devoted to explore these interactions with even fewer focused on the layer-dependence of adhesion [24-28]. Both theoretical and experimental studies conducted to estimate the adhesive interaction between graphene and SiO_2 give a range of values for adhesion energies for graphene-SiO_2 interfaces [24-28]. These discrepancies may be due to substrate roughness [29], substrate treatment, substrate morphology [28], and sliding history; the lattermost effect will be discussed in the study.

In this Chapter, adhesive interactions between silicon tips and FLG sheets on supporting substrate are investigated. AFM is used to determine the number of FLG layers and to perform local friction and adhesion measurements [30]. The pull-off forces between FLG samples and silicon tips are significantly affected by sliding the tip along the surface of graphene before conducting pull-off force measurements. This phenomenon is called the "sliding-history effect" in the following sections.

4.2: Experimental Details

4.2.1: Sample Preparation

FLG samples were produced by the mechanical exfoliation method using bulk Kish graphite (Covalent Materials Inc., Tokyo, Japan) and deposited onto a Si substrate with a 300 nm thick SiO_2 layer, or on freshly-cleaved muscovite mica substrates. Due to experimental limitations, graphene samples are at least 2-3 days old (initially exposed to air for a few hours, and then the remaining time in dry nitrogen) before any AFM and adhesion data were acquired. The Si substrate was cleaned before graphene exfoliation

using a piranha solution and then rinsed with deionized water (18.2 MΩ resistance). The root-mean-square (RMS) roughness of the silicon substrate was found to be ~0.3 nm measured over a 1×1 μm^2 area. Graphene samples were then characterized using optical microscopy and Raman microscopy to locate areas of interest before conducting AFM measurements. Before adhesion measurements were performed, these areas were again located with the AFM in topographic images acquired in contact mode. The height difference between subsequent layers was then used to confirm the number of layers present in the region of interest. Samples of FLG on muscovite mica were produced via micromechanical exfoliation onto a freshly cleaved mica surface inside a sealed chamber purged by clean dry nitrogen, at a relative humidity (RH) <2%. A typical graphene flake deposited on SiO_2 is shown in Figure 4.2.

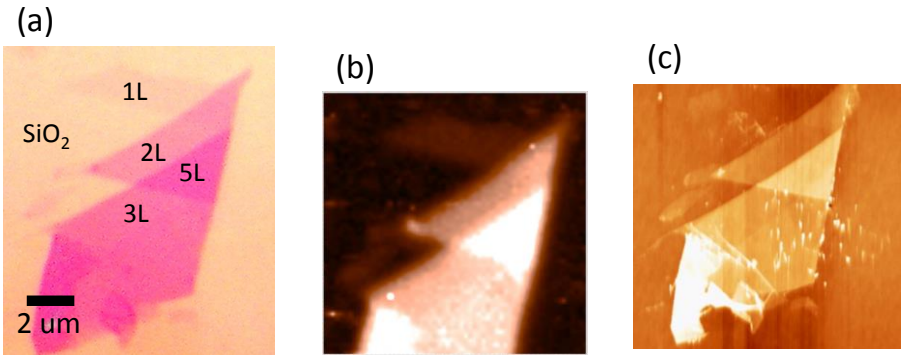

Figure 4.2: Mechanical exfoliation method is used to prepare graphene samples. (a) Optical image of a typical graphene flake prepared this way. (b) A typical Raman map of the G band, and (c) AFM topography image of the same flake. Layer numbers are determined based on AFM topography and Raman topography images, and are indicated here by 1L, 2L etc. Single-layer graphene has a thickness of ~0.34 nm.

The bulk graphite sample used in this study is highly ordered pyrolytic graphite (HOPG, SPI Supplies Inc., West Chester, PA, USA). All graphite samples were cleaved *ex-situ* in laboratory air (RH ~30-60%) and then introduced into the nitrogen-purged AFM chamber with a few minutes, thus minimizing air exposure. Adhesion measurements on freshly-cleaved samples were then conducted within 1 hour of cleaving the sample, while maintaining the low humidity environment. The graphite samples were then "aged" by leaving the samples inside the AFM chamber at <2% RH for a period of 6 days. Under these conditions, the gas environment will have trace amounts of water, oxygen, and other residual species [31]. In both freshly-cleaved and aged graphite samples, regions of interest are those areas having flat terraces greater than 100 nm in lateral dimensions.

4.2.2: Experimental Protocol

For experiments, the Raman spectrometer and Multimode AFM were first used to identify areas of interested and determination of the thickness. All other subsequent experiments were conducted in the RHK 350 AFM in a dry nitrogen environment. The dry nitrogen environment reduces the possible effects of water adsorption and prevents meniscus formation at the contact. Silicon contact-mode AFM cantilevers (CSC 37, Mikromasch Inc., Sofia, Bulgaria) were used as force sensors without further treatment, for all the experiments. The normal bending spring constant was calibrated using the Sader method [32]. The sensitivity of the PSD was the determined by measuring the slope of deflection versus *z*-sample displacement signal in a pull-off measurement against a Si substrate. Calibration of lateral spring constant was not necessary as the primary goal

was studying adhesion properties, which only involves normal forces and therefore lateral forces were less relevant. Pull-off force measurements were conducted by performing pull-off measurements on several different samples, including mechanically-exfoliated graphene on SiO_2 wafers, freshly-cleaved graphite, and air-aged graphite.

Two different series of experiments were performed: direct pull-off measurements and pre-sliding pull-off measurements. Both measurements utilize the already introduced FD spectroscopy. In direct pull-off measurements, adhesion measurements were performed using the following protocol. First, an area of interest was selected, the tip was then slid repeatedly over an area of 20×20 nm^2 of a graphene sheet to reduce possible particle contaminants between the tip and surface. Second, after breaking the contact at least once, either 20 or 100 pull-off measurements were acquired at nominally the same area on a region of the graphene sheet at a rate of 1 Hz. Third, the procedure was then repeated at other randomly-selected regions of this area of interest pertaining to graphene having different layer thicknesses. Choosing layer thicknesses at random allows us to exclude the effect of tip changes on any trends observed as a function of layer thickness. Measured pull-off forces were then averaged for each region, where the error quoted in the pull-off value represents the standard deviation.

In pre-sliding pull-off measurements, the following protocol was followed. First, just as for the case of direct pull-off measurement, once the area of interest was found, the tip was scanned over an area of 20×20 nm^2 to remove tip contamination. Second, the AFM slow-scan direction was disabled to ensure the tip would slide over the same 20 nm line, within the limits of sample/tip drift. Drift was estimated to be 1-2 nm laterally per 30 min of scanning. Third, after 512 cycles of scanning back and forth along the same line at

30 nm/s (total sliding time ~300 s, total sliding distance ~20 μm), scanning was halted and a series of pull-off measurements were then immediately recorded. The pull-off measurement was started from contact with retraction occurring first, so that the pull-off force could be recorded for the first moment the tip broke contact with the surface, and then was approached to the surface to make contact again. Subsequently, 19 additional pull-off measurements were recorded in the same position, *i.e.*, without any lateral motion at a rate of 1 Hz.

4.3: FEM Simulations

Additionally, to gain mechanistic information and to mimic the processes governing single asperity adhesion on graphene, FEM simulations were conducted for pre-sliding pull-off measurements by Dr. Q. Li. For simplicity, we have simulated a 2-D contact mechanics problem considering adhesive interaction as described in the model in Ref. [22]. Briefly, the model consists of a single layer graphene sheet represented by a thin elastic plate, and the substrate is a rigid body representing the SiO_2 substrate. The tip-graphene interaction is implemented by an effective adhesive force and a frictional shear stress. The values of graphene bending stiffness and in-plane rigidity for graphene were taken from Ref. [33]. Both the tip-graphene interaction strength, w_{tip-gr}, and the graphene-substrate interaction strength, w_{gr-sub}, are described by an effective adhesive potential derived for graphene based on the Lennard-Jones potential by integrating over the surface of the contacting bodies [34]. Using this model, the two types of pull-off measurements described above were simulated. The first case is intended to mimic the direct pull-off measurements, where the tip is brought into contact with the sheet and then

immediately withdrawn while the normal force was recorded. In the second case, intended to mimic the pre-sliding pull-off measurements, the same tip was brought into contact with the sheet and then slid along the surface under a compressive normal load until friction reaches a steady-state value. Following sliding, the tip was withdrawn from the surface while the normal force was recorded. The configurations were examined as a function of the interaction ratios between $w_{\text{tip–gr}}$ and $w_{\text{gr–sub}}$. Two ratios were examined: 1.2 and 2.0, representing cases with 'fresh' and 'aged' graphene surfaces, respectively. The maximum tensile normal load during retraction was regarded as the pull-off force. For the chosen ratios, the case of regular pull-off was compared to pre-sliding pull-off, representing the traditional and pre-sliding pull-off measurement, respectively.

4.4: Results

4.4.1: Direct Pull-Off Measurements

Figure 4.3 (a) shows five datasets, each of 100 pull-off force values, plotted *vs.* the measurement number on FLG. The pull-off forces are measured by direct pull-off measurements, or FD measurements. The FLG regions had thicknesses ranging from 1 to 5 layers, with one dataset acquired for each number of layers. Within each dataset, pull-off forces are plotted in chronological order. In these measurements, pull-off measurement number 1 refers to the first measured pull-off force, 2 the second measured pull-off force, *etc*. The pull-off forces were normalized to the mean value measured for each set of measurements to better show the relative change in the force. Figure 4.3 (a) shows that the variation in pull-off forces measured at one area of interest does not vary significantly with increasing pull-off measurement number.

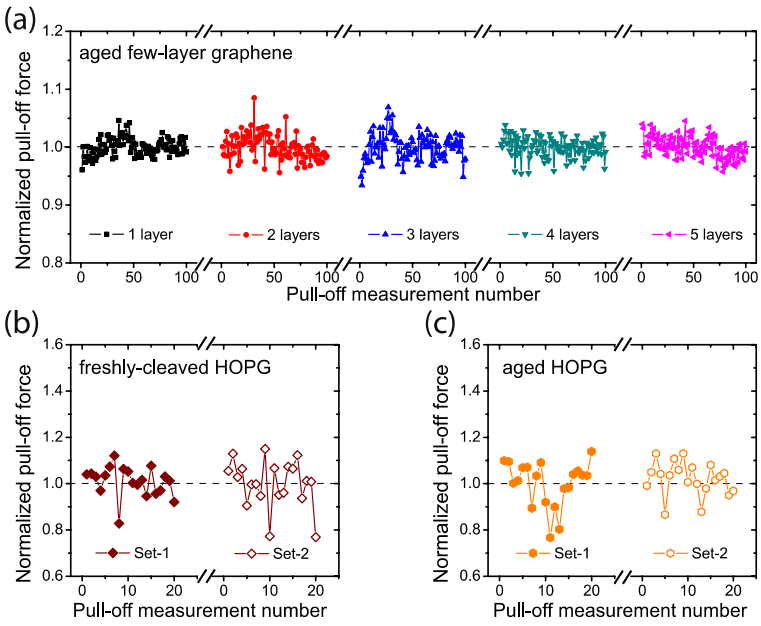

Figure 4.3: Normalized pull-off forces plotted versus measurement number on FLG with 1 to 5 layers, acquired using direct pull-off measurements. The measured pull-off forces have been normalized to their mean values in each set of connected data points. Normalized pull-off forces plotted versus FD curve measurement number for (b) freshly-cleaved and (c) aged graphite, respectively. In (b) and (c) the same tip was used. However, each "set" refers to pull-off forces measured in different regions of interest on the same sample. A gray dashed line indicates the mean value in each case.

The absolute mean pull-off force measured on a single layer graphene in Figure 4.3 (a) is 18.7±0.4 nN. This magnitude is representative of the values measured throughout the experiments. Similar values were obtained on regions with more layers. We can estimate the corresponding work of adhesion by applying continuum adhesive contact mechanics [35], and using an estimated tip radius of ~15±5 nm. This value is based both on manufacturer's values and on transmission electron microscopy

measurements of tip radii we acquired for other tips of the same make and model as that used here. This value is thus representative of unused AFM tips. According to the JKR model [36], this pull-off force corresponds to a work of adhesion of 0.26±0.09 J/m^2 between the silicon tips and graphene. When the DMT model is used [37], this pull-off force corresponds to a work of adhesion of or 0.20±0.07 J/m^2. Averaging these two results in a mean value of 0.23±0.11 J/m^2. This number is on the same order of magnitude as the values reported in the literature [25, 26].

In addition, direct pull-off force measurements were performed on freshly-cleaved graphite and aged graphite. In this case, each dataset consisted of 20 pull-off measurements within a given area of the sample, and two different areas of each sample were tested with the same tip. The results are plotted in Figure 4.3 (b) and (c), which show that for both freshly-cleaved and aged graphite, respectively, the pull-off forces did not vary over the course of a direct pull-off measurement series, just as observed in Figure 4.3 (a) for FLG. Furthermore, there was no significant change in the pull-off force trends measured on different regions of the freshly-cleaved and aged graphite samples.

Figure 4.4 (a) shows the mean pull-off force as a function of the number of graphene layers for FLG as well as for freshly-cleaved bulk graphite. Approximately 100 measurements are taken for each thickness value. For a given test, the same tip was used to measure all pull-off forces on FLG flakes of different thicknesses and on graphite. In each test, the pull-off force values were normalized to the mean value obtained for the lowest number of graphene layers, to emphasize the variation in adhesion as a function of the number of layers. This normalization also allows a comparison between pull-off forces measured with the three tips by reducing the effect of variability in tip size and tip

chemistry. Figure 4.4 shows that to within the standard deviation of the measurement, there is no variation in the measured pull-off force as a function of the number of graphene layers. Figure 4.4 shows that the pull-off forces measured on graphite were slightly lower on average than for FLG. However, the difference is within experimental uncertainty for Tips 1 and 2, and we note that the graphite sample had less air exposure than the FLG samples prior to insertion into the AFM chamber. The reduced air exposure of freshly cleaved graphite compared to FLG samples is due to the different amounts of time required for sample preparation in each case: the graphite can be cleaved, inserted in the AFM, and measured within as little as 10 minutes; FLG, on the other hand, requires optical microscopy and Raman imaging to identify the number of layers of graphene that are then targeted for subsequent AFM measurements. Figure 4.4 (b) shows the same experiment performed on a different FLG sample in ambient air, and also no significant variation in pull-off force is observed.

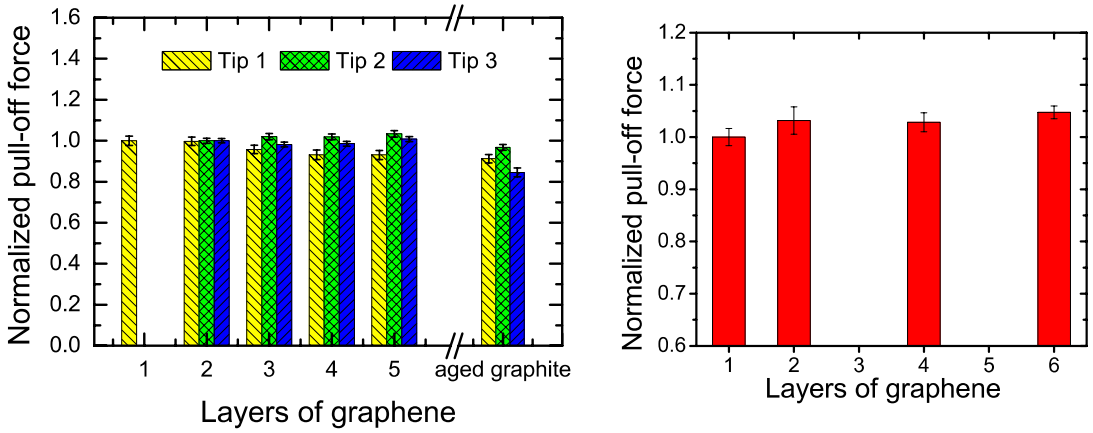

Figure 4.4: (a) Normalized pull-off forces versus number of layers of graphene. The same tip was used within one test, and a single area investigated for each bar plotted. The number of layers was varied with a random order. Different tips and FLG samples were used in the three tests. Each test on graphite was performed on an N_2-aged sample, using the same tip used for the other FLG samples indicated for that test. Error bars represent the standard deviation in the mean value of the normalized pull-off force for each FLG or graphite sample (a few tens of measurements acquired for each). (b) Normalized pull-off forces versus number of layers of graphene, measured in ambient air. The same tip was throughout the entire measurement. The number of layers was varied in random order. Error bars represent the standard deviation in the mean value of the normalized pull-off force for each FLG (~100 measurements acquired for each).

4.4.2: Pre-sliding Pull-Off Measurements

In direct pull-off force measurements, lateral sliding of the tip does not occur, beyond the small amount of in-plane displacement that occurs (approximately 10% of the vertical extension, or ~10 nm) during a FD measurement resulting from the 22.5° tilt angle between the cantilever and the surface normal, which is intrinsic to the experimental protocol. FD measurements were repeated using a "tilt compensation"

protocol [38] that greatly reduces this in-plane displacement, and the trends were the same.

However, the previously-reported dependence of friction on the number of layers involves prolonged lateral sliding (several μm) of the tip with respect to the sample [22]. These prior friction results indicate that it is problematic to measure adhesion using the direct pull-off technique, as it does not include the influence of sliding history on the interface. However, using the pre-sliding test protocol, the pull-off force acquired includes an effect of tip sliding on the pull-off force in the first instant the contact between the sample and tip occurs.

Figure 4.5 shows the consecutive pull-off forces acquired after pre-sliding the tip on FLG samples, a freshly-cleaved graphite sample, and an aged graphite sample. In the same manner as Figure 4.3 (a), Figure 4.5 (a) shows the pull-off force recorded with increasing FD curve measurement number for FLG samples of different numbers of layers (1-5). In Figure 4.5 (a), the value marked by the gray dashed line represents the steady-state response used for normalizing the data and is based on the mean value of the 20 data points for each sample. This removes the effect of the transiently high values observed during the first few pull-off force measurements. The same measurements were also performed on freshly-cleaved graphite, Figure 4.5 (b), and aged graphite, Figure 4.5 (c), respectively. The first pull-off force measured is significantly higher than the pull-off forces subsequently measured for graphene (Figure 4.5 (a)) and for aged graphite (Figure 4.5 (c)) surfaces. Specifically, the pull-off force measured for FLG were 12-17% higher for FD curve measurement number 1 in comparison to subsequently measured pull-off

forces. However, freshly-cleaved graphite (Figure 4.5 (b)) shows no transient change in the measured pull-off force.

Figure 4.6 shows the mean value of the first pull-off force measured (normalized to the mean value of the 20 pull-off forces that are equivalent to the steady-state values found, indicated by the dashed line) for all layers of FLG and aged graphite. The data presented involves the normalized values acquired using multiple tips and different samples. For example, in the case of FLG, the data acquired is from more than 100 different pull-off force measurements for each layer number. As in the case of the direct pull-off measurements, the error bars represent the standard deviation in the calculated mean value. Figure 4.6 shows that the first pull-off force is significantly higher than subsequent values. Furthermore, there is no statistically significant variation in the measured value of first pull-off force for graphene with the number of graphene layers.

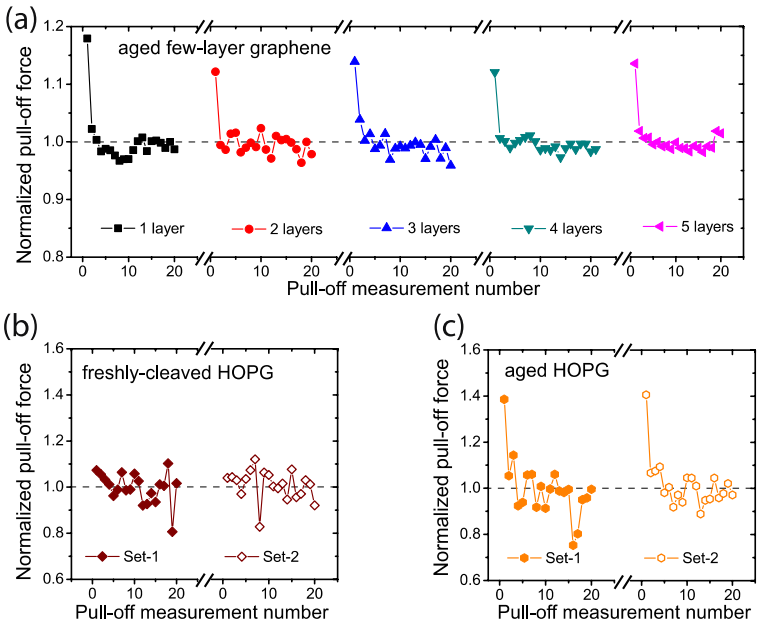

Figure 4.5: (a) Normalized pull-off forces *vs*. measurement number on FLG with 1 to 5 layers, acquired using the pre-sliding methodology. The pull-off forces of the each set (connected with a solid line) have been normalized to the mean values of that particular set (represented by a grey dashed line). The measurements on graphene come from a single sample and have all been conducted using the same tip. The same pre-sliding measurement carried out on (b) freshly-cleaved graphite and (c) aged graphite. In (b) and (c) the same tip has been used in both "sets", but measurements have been performed on different regions of interest that are far away from each other. The pull-off forces have been normalized to the mean value of the dataset (black dashed line).

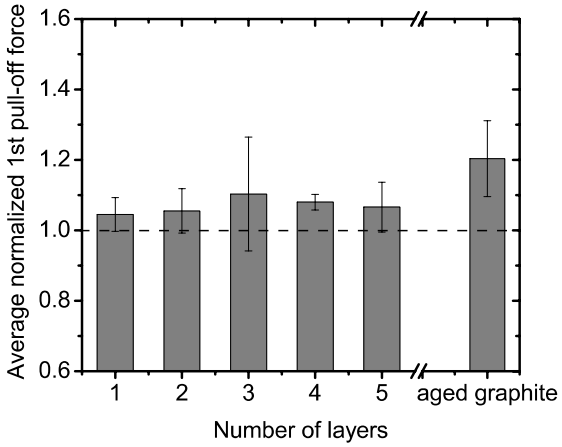

Figure 4.6: Mean pull-off forces of the first data point of all dataset of pull-off force measurements collected, normalized beforehand in a manner described earlier. The mean values for each FLG layer number and for aged graphite was calculated from over 100 measurements of an increased pull-off force during pre-sliding measurements. Error bars represent the standard deviation obtained from averaging the first data points for each layer number.

Lastly, experiments were performed pre-sliding measurements on the following samples: FLG on mica and bare mica samples. The results are shown in Figure 4.7. For the case of mica (Figure 4.7 (a)), due to its strong adhesive interaction between the FLG and the substrate, the transient increase in adhesion is absent. Additionally, if the material has a strong intrinsic interlayer interaction, *e.g.* mica, there will also be no transient increase in adhesion, as shown in Figure 4.7 (b).

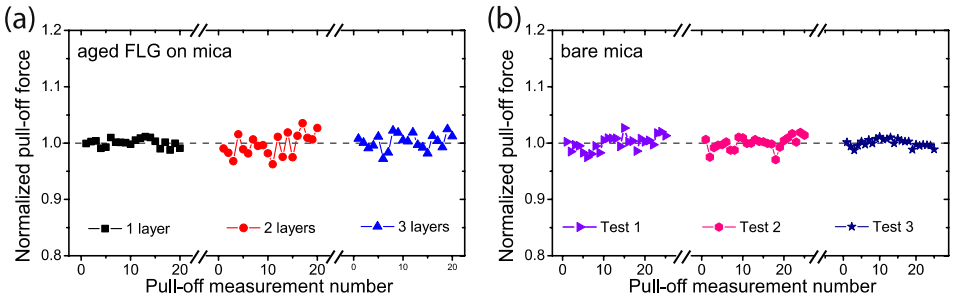

Figure 4.7: (a) Normalized pre-sliding pull-off forces measured on graphene on muscovite mica. Clearly, overall the pull-off force stays rather constant and no sliding-history dependence is observed due to the stronger graphene-mica adhesion. Notice the 1 layer graphene shows an extremely low variation. (b) Normalized pre-sliding pull-off forces measured on a bare muscovite mica substrate. No sliding-history dependence is observed in any of these cases.

4.4.3: FEM Simulations

FEM simulations were conducted to gain mechanistic insight into observed behavior. The two different types of AFM pull-off experiments were simulated: direct pull-off, and pre-sliding pull-off. We also investigated the effect of changing the adhesive interaction between the tip and the graphene relative to the graphene-substrate interaction. In the FEM simulations, only the first pull-off force is measured, as opposed to the AFM measurements where many subsequent pull-off forces are measured. The results of these simulations are shown in Figure 4.8. Figure 4.8 (a) shows that there is no difference in the pull-off force measured in both direct pull-off and with pre-sliding when the ratio between the tip-graphene interaction strength, $w_{\text{tip–gr}}$, and the graphene-substrate interaction strength, $w_{\text{gr–sub}}$, is 1.2, representing the case where the sample is not aged. Figure 4.8 (b) and (c) show snapshots of the FEM simulation during a pull-off measurement via the direct pull-off and the pre-sliding pull-off methods, respectively.

The deformation of the graphene film is the same during pull-off measurements in direct pull-off and pre-sliding pull-off measurements. However, when the ratio w_{tip-gr}/w_{gr-sub} is increased to 2.0 to represent the case of an aged sample where the topmost layer has higher adhesion, there is a ~9% higher measured pull-off force in pre-sliding experiments compared to direct pull-off experiments. Figure 4.7 (d) and (e) show snap-shots of tip, graphene film, and substrate during the pull-off simulation. Figure 4.7 (d) shows that in direct pull-off force measurements, the graphene film is symmetric around the tip and lifting off the substrate. However, Figure 4.7 (e) shows that pre-sliding drastically changed the interface configuration: at the same tip-substrate separation distance, the graphene film exhibits a greater amount of delamination for the case of pre-sliding than direct pull-off, as well as a greater contact area at the point of snap-out, yielding a greater pull-off force.

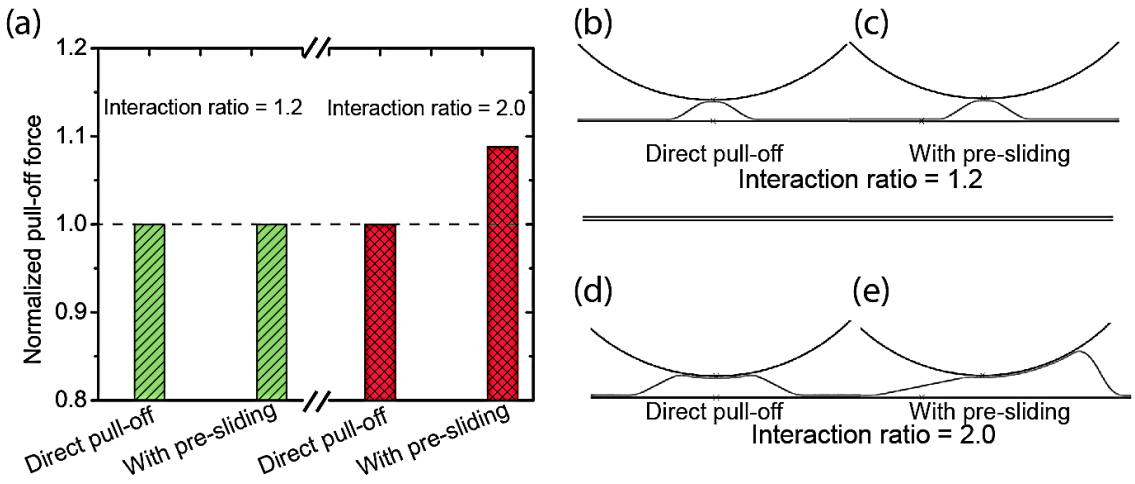

Figure 4.8: (a) FEM simulation results for normalized pull-off forces for interaction rations of w_{tip-gr}/w_{gr-sub} =1.2 (green) and 2.0 (red) using direct pull-off measurements and with pre-sliding. The direct pull-off force is the same as that with pre-sliding for an interaction ratio of 1.2, whereas an interaction ratio of 2.0 results in an increase of ~9% compared to direct pull-off. (b) and (c) show excerpts from simulations with interaction ratio 1.2 for direct pull-off and with pre-sliding, respectively. The same for (d) and (e) is shown but with interaction ratio 2.0.

4.5: Discussion

In direct pull-off measurements, the pull-off forces did not change over a set of 100 measurements. The mean pull-off force observed on a single layer graphene is 18.7±0.4 nN, corresponding to an average value of the work of adhesion of 0.23±0.11 J/m^2. This average value is well in the range of the values reported in the literature [25-27]. Only a slight variation in the direct pull-off force data is observed, suggesting that the contact geometry of the tip and graphene does not evolve significantly over the course of measurement. These slight variations are likely due to changes in local morphology or roughness of the substrate, as previously reported in the literature [27-29]. Similar results

were also obtained on both freshly-cleaved and aged graphite, although the standard deviations are higher than that observed for FLG. The origin of this variation is not understood. Figure 4.4 shows a weak but statistically insignificant variation in measured direct pull-off forces on FLG as pull-off measurements are repeated, which is consistent with previously reported adhesion measurements in the literature [22, 27]. Further experiments conducted on different number of layers of FLG in laboratory air also show a negligible variation in the measured pull-off forces with the number of layers.

These observations of direct pull-off forces with insensitivity to the number of graphene layers are in apparent contrast to the previously-reported layer-dependent friction force on graphene. A monotonic decrease in friction force of approximately ~50% is observed for a four layer FLG in comparison to one layer [22]. The mechanism behind the layer-dependent friction is explained by the lower bending stiffness of single layer graphene. Being more susceptible to out-of-plane elastic deformation, higher friction occurs than for thicker sheets because adhesion and friction forces lead to larger contact areas between the tip and graphene. However, in direct pull-off force measurement (without pre-sliding of the tip), no variation was observed in the work of adhesion as a function of number of layers. Thus, the total intrinsic adhesive interaction, which is due primarily to van der Waals forces, does not depend observably on the number of layers. Thus, as postulated previously, the observed dependence of friction on number of layers is not due to changes in tip-sample adhesion. Furthermore, it suggests that the contact geometry in direct pull-off force measurements is rather different than what occurs during friction measurements. A possible explanation for the layer-

insensitive pull-off force measurements may result from the fact that adhesion forces are dominated by the surface interactions between the AFM tip and the graphene surface. FEM results in Figure 4.8 (b) and Figure 4.8 (d) show that the graphene sheet deforms symmetrically under tensile forces, consistent with the literature [39]. This symmetric deformation of the graphene sheet during pull-off measurements is likely to be isolated to the topmost graphene layer in either the FLG or bulk graphite samples, resulting in a layer-independent pull-off force. A FEM simulation with different numbers of layers will be discussed in a future publication.

The steady-state pull-off forces observed in pre-sliding pull-off measurements on FLG in Figure 4.5 (a), *i.e.*, the pull-off forces recorded at pull-off measurement numbers greater than 5, show similar trends as those determined from direct pull-off measurements Figure 4.3 (a). Similar trends are also observed for measurements done on freshly-cleaved and aged graphite between the steady state values measured in pre-sliding measurements in Figure 4.5 (b) and (c) respectively, and those measured on the same sample using the direct pull-off measurement technique in Figure 4.3 (b) and (c), respectively. This result indicates that after 5 pull-off measurements, the contact between the AFM tip and the sample is not affected by previous sliding. However, the increase in the first pull-off force measurement shown in Figure 4.5 (a), which can be up to ~17% higher than the steady state value, demonstrates that the nature of the interface just before the first pull-off measurement after sliding must be distinct from the other situations.

The variation in the initial enhancement of the pull-off force in pre-sliding measurements (Figure 4.6) is independent on the number of layers. Hence, the thin-film puckering effect that strongly influences friction measurements cannot be responsible for

the pull-off force enhancement since that effect depends on the number of layers and is absent for graphite. Using AFM, Deng *et al*. reported aging of graphite samples after cleavage when exposed to air increases the interaction between a sliding tip and the topmost graphite layer relative to the interlayer bonding between the bulk graphite layers [23]. We hypothesize that this mechanism is primarily responsible for the adhesion trends we observe in pre-sliding measurements.

This hypothesis is supported by two observations. First, as discussed above, the transient increase in pull-off force with pre-sliding, the steady-state pull-off force with pre-sliding, and the pull-off force from direct pull-off measurements are all independent of the number of layers, and that a transient increase in the pull-off force also occurs on aged graphite. Thus, it appears to be related to the state of the topmost graphene layer of the sample. Second, in freshly-cleaved graphite samples, no increase in pull-off force was observed in pre-sliding measurements, just as Deng *et al.* saw no increased tip-sample interaction for freshly-cleaved graphite [23]. These observations are consistent with the mechanism demonstrated by varying the adhesive interaction between the tip and substrate shown in the FEM simulation in Figure 4.8: aging the sample increases the adhesion between the topmost layer of graphene, and the structure of the graphene region around the contact is more strongly affected by sliding. It is further shown that if one imposes a strong adhesive interaction between the graphene and the substrate, for example by examining graphene exfoliated onto freshly-cleaved muscovite mica, the transient increase in adhesion is again lost.

The proposed mechanism by which pull-off forces are enhanced after pre-sliding is illustrated schematically in Figure 4.9. Due to a low substrate-graphene interaction

energy, the graphene loosely adheres to the substrate. Exposing the graphene to air (during sample preparation and the steps required to identify graphene on the substrate) results in aging of the top graphene layer (indicated by the red color), leading to an enhanced tip-graphene interaction that exceeds that of the graphene-graphene interlayer interaction. When the tip comes into contact, a symmetric pucker will form around the AFM tip as shown in Figure 4.9 (a). Upon sliding in Figure 4.9 (b), the symmetric pucker on the top-layer transforms asymmetrically such that the pucker at the front edge of the tip is larger in comparison to the rear edge. The size of the pucker at the front is expected to depend on the thickness of the graphene, as inferred from the friction measurements in Ref. [22]. After some sliding distance, the pucker reaches a maximum, steady-state size, resulting in a maximum steady-state contact area. Tip sliding is then halted and the tip-graphene contact is assumed to not relax; the tip then begins retract from the surface. This initial stage of a pre-sliding pull-off measurement is shown in Figure 4.9 (c). Owing to the increased tip-graphene interaction, the interfacial configuration of the tip and top graphene layer changes significantly, leading the top-layer to delaminate. The force required for separation is thus enhanced. This is consistent with the friction measurements of Deng *et al*., who see enhanced friction when retracting after pre-sliding on aged graphite or graphene [23].

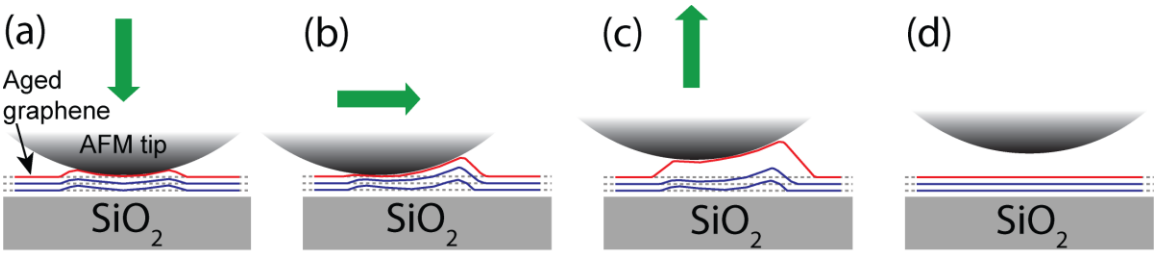

Figure 4.9: A schematic view of the pre-sliding pull-off measurement. The bold, green arrows indicate the direction of the tip motion. The red line represents the top graphene layer that is aged and thus can delaminate due to its enhanced interaction with the tip. (a) The AFM tip makes initial contact with the graphene sheet prior to reciprocating over that local area. (b) While scanning in a reciprocating motion, a small, asymmetric pucker gradually develops due to adhesion and friction between the sample and the tip. (c) At the end of the sliding cycles, the tip retracts. Due to the strengthened tip-graphene interaction, the interfacial configuration has changed such that the top layer locally delaminates. This enhances the pull-off force. (d) After retraction, the graphene sheet relaxes and returns to the undeformed state.

Comparing the case of a few graphene layers or many layers (graphite) to a single layer of graphene, based on previously-reported friction measurements [22], the single layer has a bigger pucker owing to its lower bending stiffness (associated with its low thickness). However, this does not lead to an even greater enhancement in the pull-off force compared to multiple layers. There are two factors which can contribute to this lack of layer dependence: (1) for multilayer samples, the interlayer interaction between the top graphene layer and second layer below is stronger than the interaction between monolayer graphene and the silicon oxide substrate. Therefore, there will be an additional force resisting the delamination of the top-layer, which tends to increase the pull-off force

for multilayers; and (2) there is an increased strain energy release rate for thinner layers due to the more highly deformed graphene around it. This will tend to decrease the pull-off force for thinner layers. These two effects can explain why the first pre-sliding-enhanced pull-off force for monolayer graphene (when weakly adhered to it substrate) is not significantly different than that for multilayers or for graphite. Full verification of these hypotheses would require detailed atomistic calculations which are beyond the scope of this paper. Finally, once the contact is broken, the top-layer pucker relaxes as shown in Figure 4.9 (d), and subsequent measurements show lower pull-off forces in comparison to the first measured pull-off force. The steady-state value obtained during subsequent measurements is similar to the case obtained during direct pull-off measurement.

We note that in some of the sets of measurements, particularly Figure 4.5 (a) for 1, 3, and 5 layers, and Figure 4.5 (c) for both measurement sets of aged graphite, the relaxation to the steady-state value of the pull-off force is not immediate: the next two or three pull-off force measurements show a slightly enhanced pull-off force. This suggests that, in some cases, the relaxation of the region of graphene deformed by the pre-sliding persists over a surprisingly long time scale, as the time elapsed between successive pull-off measurements in Figure 4.5 is 1 s. The lack of consistency in observing this effect could be due to thermal drift, or due to inhomogeneities in the graphene surface chemistry. Further work is required to fully understand this effect.

4.6: Summary

To summarize, from this study we have a better understanding of the roles of the three adhesive interactions that altogether govern the response of the entire mechanical system: the interfacial adhesion between the graphene and its SiO_2 substrate; adhesion between a moving asperity and the graphene/substrate system; and the interlayer interaction for multilayer graphene films. Adhesive interactions between tip and graphene increase upon exposing the graphene surface to oxygen-containing environments. The effect of sliding history on the surface of FLG and graphite becomes important when the adhesive interaction between the surface and the tip exceeds the graphene interlayer bonding or the graphene/substrate adhesion. Finally, given the insensitivity of the pull-off force to the number of layers of FLG, the graphene-substrate adhesion and the graphene interlayer bonding is apparently relatively unaffected by chemical modification, in contrast to the tip-graphene interaction. This result is consistent with the previous literature demonstrating the chemical impermeability of graphene sheets [26]. Based on our picture of the adhesion behavior of graphene, we hypothesized that the effect of sliding history is localized to the topmost layer and does not influence subsequent layers in multilayer FLG. However, more work is needed to further investigate the nature of the graphene deformation below the top layer, for example, by comparing the results of fresh to aged FLG samples, and by combining with simulation, which can provide information at and below the buried interface.

To summarize, experiments were performed to investigate the nanoscale adhesion properties of graphene onto silicon oxide using silicon AFM probes in nitrogen-purged

environments. Although previous observations show that friction on graphene, as with other atomically-thin films, exhibits a strong dependence on the number of layers, direct pull-off measurements (with no pre-sliding) show that the pull-off force is independent of the number of graphene layers. Based on estimates of the tip radii used, the average work of adhesion between the silicon tips (which have a native oxide) and graphene is found, using continuum adhesive contact mechanics, to be 0.23 ± 0.11 J/m^2. However, if the graphene or graphite has been aged via exposure to air, or a N_2 atmosphere (which contains trace amounts of water and oxygen), and if the tip is pre-slid against the sample, the pull-off force is enhanced by 12-17% the first time the tip-sample contact is broken. The enhancement disappears after subsequent pull-off force measurements at the same location. The enhancement is not observed for thin graphene layers that were deposited on freshly-cleaved muscovite mica and then aged; nor was it observed on freshly-cleaved graphite.

These results indicate that aging of graphite and graphene films result in strengthening of adhesive interaction between a silicon tip and the topmost layer of graphene on the sample. This effect is seen to occur in FEM simulations using physically reasonable parameters. Based on results of Deng *et al.* [23], the aging process leads to some degree of oxidation of the surface, and this more polar surface interacts more strongly with the native oxide of the silicon AFM tip. When the interaction between the tip and the topmost layer of graphene/graphite is further strengthened by sliding, the tip-graphene interfacial configuration is substantially altered such that topmost layer locally delaminates under tensile loading, leading to an enhanced pull-off force. Upon subsequent pull-off force measurements, the topmost graphene/graphite layer relaxes to

the geometrical state it had before sliding. The effect is suppressed in FLG exfoliated onto freshly-cleaved muscovite mica because the strong interaction energy between the mica and the graphene prevents the local delamination. These measurements, or the observation of a sliding dependent pull-off force, demonstrate the importance of the three interfaces (tip/substrate; substrate/graphene; graphene/tip) when measuring adhesion forces on 2-dimensional materials. It also shows that minimization of adhesion forces on graphene-terminated surfaces that will be exposed to oxygen-containing atmospheres can be attained by using few layers that are strongly adhered to their substrate.

4.7: References

1. X.-Z. Liu, Q. Li, P. Egberts, and R.W. Carpick, Nanoscale adhesive properties of graphene: The effect of sliding history. *Advanced Materials Interfaces* **2014**, 1-9.
2. P. Wallace, The band theory of graphite. *Physical Review* **1947**, 71(9), 622.
3. K.S. Novoselov, A.K. Geim, S.V. Morozov, D. Jiang, Y. Zhang, S.V. Dubonos, I.V. Grigorieva, and A.A. Firsov, Electric field effect in atomically thin carbon films. *Science* **2004**, 306(5696), 666-9.
4. C. Lee, X. Wei, J. Kysar, and J. Hone, Measurement of the elastic properties and intrinsic strength of monolayer graphene. *Science* **2008**, 321(5887), 385.
5. *The Nobel Prize in Physics 2010*. 2010; Available from: http://nobelprize.org/nobel_prizes/physics/laureates/2010/index.html.
6. X. Li, W. Cai, J. An, S. Kim, J. Nah, D. Yang, R. Piner, A. Velamakanni, I. Jung, E. Tutuc, S.K. Banerjee, L. Colombo, and R.S. Ruoff, Large-area synthesis of high-quality and uniform graphene films on copper foils. *Science* **2009**, 324(5932), 1312-4.
7. Z. Luo, S. Kim, N. Kawamoto, A.M. Rappe, and A.T.C. Johnson, Growth mechanism of hexagonal-shape graphene flakes with zigzag edges. *ACS Nano* **2011**, 5(11), 9154-9160.
8. P. Egberts, G.H. Han, X.Z. Liu, A.T.C. Johnson, and R.W. Carpick, Frictional behavior of atomically thin sheets: Hexagonal-shaped graphene islands grown on copper by chemical vapor deposition. *ACS Nano* **2014**, 5010–5021.

9. S. Bae, H. Kim, Y. Lee, X. Xu, J.S. Park, Y. Zheng, J. Balakrishnan, T. Lei, H.R. Kim, and Y.I. Song, Roll-to-roll production of 30-inch graphene films for transparent electrodes. *Nature Nanotechnology* **2010**, 5, 574-578.
10. J.T. Robinson, J.S. Burgess, C.E. Junkermeier, S.C. Badescu, T.L. Reinecke, F.K. Perkins, M.K. Zalalutdniov, J.W. Baldwin, J.C. Culbertson, and P.E. Sheehan, Properties of fluorinated graphene films. *Nano Letters* **2010**, 8, 3001-3005.
11. T. Kuila, S. Bose, A.K. Mishra, P. Khanra, N.H. Kim, and J.H. Lee, Chemical functionalization of graphene and its applications. *Progress in Materials Science* **2012**, 57(7), 1061-1105.
12. K.S. Novoselov, V.I. Fal'ko, L. Colombo, P.R. Gellert, M.G. Schwab, and K. Kim, A roadmap for graphene. *Nature* **2012**, 490(7419), 192-200.
13. L. Yan, Y.B. Zheng, F. Zhao, S. Li, X. Gao, B. Xu, P.S. Weiss, and Y. Zhao, Chemistry and physics of a single atomic layer: strategies and challenges for functionalization of graphene and graphene-based materials. *Chemical Society Reviews* **2012**, 41(1), 97-114.
14. V. Georgakilas, M. Otyepka, A.B. Bourlinos, V. Chandra, N. Kim, K.C. Kemp, P. Hobza, R. Zboril, and K.S. Kim, Functionalization of graphene: Covalent and non-covalent approaches, derivatives and applications. *Chemical Reviews* **2012**, 112(11), 6156-6214.
15. S. Park and R. Ruoff, Chemical methods for the production of graphenes. *Nature Nanotechnology* **2009**, 4(4), 217-224.
16. S. Stankovich, D. Dikin, G. Dommett, K. Kohlhaas, E. Zimney, E. Stach, R. Piner, S. Nguyen, and R. Ruoff, Graphene-based composite materials. *Nature* **2006**, 442(7100), 282-286.
17. C. Berger, Z. Song, T. Li, X. Li, A. Ogbazghi, R. Feng, Z. Dai, A. Marchenkov, E. Conrad, and W. De Heer, Ultrathin epitaxial graphite: 2D electron gas properties and a route toward graphene-based nanoelectronics. *Journal of Physical Chemistry B* **2004**, 108(52), 19912-19916.
18. Y.J. Shin, R. Stromberg, R. Nay, H. Huang, A.T.S. Wee, H. Yang, and C.S. Bhatia, Frictional characteristics of exfoliated and epitaxial graphene. *Carbon* **2011**, 49(12), 4070-4073.
19. K.-S. Kim, H.-J. Lee, C. Lee, S.-K. Lee, H. Jang, J.-H. Ahn, J.-H. Kim, and H.-J. Lee, Chemical vapor deposition-grown graphene: The thinnest solid lubricant. *ACS Nano* **2011**, 5107–5114.

20. G.H. Lee, R.C. Cooper, S.J. An, S. Lee, A. van der Zande, N. Petrone, A.G. Hammerberg, C. Lee, B. Crawford, W. Oliver, J.W. Kysar, and J. Hone, High-strength chemical-vapor-deposited graphene and grain boundaries. *Science* **2013**, 340(6136), 1073-6.
21. T. Filleter, J.L. McChesney, A. Bostwick, E. Rotenberg, K.V. Emtsev, T. Seyller, K. Horn, and R. Bennewitz, Friction and dissipation in epitaxial graphene films. *Physical Review Letters* **2009**, 102(8), 086102.
22. C. Lee, Q. Li, W. Kalb, X.-Z. Liu, H. Berger, R.W. Carpick, and J. Hone, Frictional characteristics of atomically thin sheets. *Science* **2010**, 328(5974), 76.
23. Z. Deng, A. Smolyanitsky, Q. Li, X.Q. Feng, and R.J. Cannara, Adhesion-dependent negative friction coefficient on chemically modified graphite at the nanoscale. *Nature Materials* **2012**, 11(12), 1032-1037.
24. M. Ishigami, J. Chen, W. Cullen, M. Fuhrer, and E. Williams, Atomic structure of graphene on SiO2. *Nano Letters* **2007**, 7(6), 1643-1648.
25. Z. Zong, C. Chen, M. Dokmeci, and K. Wan, Direct measurement of graphene adhesion on silicon surface by intercalation of nanoparticles. *Journal of Applied Physics* **2010**, 107(2), 6104.
26. S.P. Koenig, N.G. Boddeti, M.L. Dunn, and J.S. Bunch, Ultrastrong adhesion of graphene membranes. *Nature Nanotechnology* **2011**, 6(9), 543-546.
27. Z. Deng, N.N. Klimov, S.D. Solares, T. Li, H. Xu, and R.J. Cannara, Nanoscale interfacial friction and adhesion on supported versus suspended monolayer and multilayer graphene. *Langmuir* **2013**, 29(1), 235-43.
28. W. Gao and R. Huang, Effect of surface roughness on adhesion of graphene membranes. *Journal of Physics D: Applied Physics* **2011**, 44, 452001.
29. C. Lui, L. Liu, K. Mak, G. Flynn, and T. Heinz, Ultraflat graphene. *Nature* **2009**, 462(7271), 339-341.
30. R.W. Carpick and M. Salmeron, Scratching the surface: Fundamental investigations of tribology with atomic force microscopy. *Chemical Reviews* **1997**, 97(4), 1163-1194.
31. P. Egberts, Z. Ye, X.-Z. Liu, Y. Dong, A. Martini, and R.W. Carpick, Environmental dependence of atomic-scale friction at graphite surface steps. *Physical Review B* **2013**, 88(3),
32. J.E. Sader, J.W.M. Chon, and P. Mulvaney, Calibration of rectangular atomic force microscope cantilevers. *Review of Scientific Instruments* **1999**, 70, 3967.

33. M.F. Yu, O. Lourie, M.J. Dyer, K. Moloni, T.F. Kelly, and R.S. Ruoff, Strength and breaking mechanism of multiwalled carbon nanotubes under tensile load. *Science* **2000**, 287, 637.
34. L.Y. Jiang, Y. Huang, H. Jiang, G. Ravichandran, H. Gao, K.C. Hwang, and B. Liu, A cohesive law for carbon nanotube/polymer interfaces based on the van der Waals force. *Journal of the Mechanics and Physics of Solids* **2006**, 54(11), 2436-2452.
35. K.L. Johnson, *Contact Mechanics*; Cambridge University Press: Cambridge, UK, 1987.
36. K.L. Johnson, K. Kendall, and A.D. Roberts, Surface energy and the contact of elastic solids. *Proceedings of the Royal Society of London A* **1971**, 324(1558), 301-313.
37. B. Derjaguin, V. Müller, and Y.P. Toporov, Effect of contact deformations on the adhesion of particles. *Journal of Colloid and Interface Science* **1975**, 53(2), 314-326.
38. R.J. Cannara, M.J. Brukman, and R.W. Carpick, Cantilever tilt compensation for variable-load atomic force microscopy. *Review of Scientific Instruments* **2005**, 76, 053706.
39. Z. Ye, C. Tang, Y. Dong, and A. Martini, Role of wrinkle height in friction variation with number of graphene layers. *Journal of Applied Physics* **2012**, 112(11), 116102.

Chapter 5: Fluorination of Graphene Enhances Friction Due to Increased Corrugation

From the previous Chapter, the interfacial shear strength of silicon tips sliding against graphene was observed to be enhanced due to aging, and combined with pre-sliding, this aging effect can result in an increased contact area and thus greater adhesion force. This Chapter presents the results of friction studies of silicon tips sliding against graphene and fluorinated graphene (FG). Chemical modification of graphene by chemical reaction with fluorine gas will be shown to be another pathway by which the interfacial shear strength can be modified. Specifically, this chapter will focus on the frictional behavior of graphene compares with fluorinated graphene, including how various degrees of fluorination influence friction. Through this examination, it will be possible to understand the role of fluorination on τ and A_r. This Chapter begins with discussion of the friction reducing behavior of graphene and how chemical functionalization of graphene can influence friction. Following the introduction, experimental details, including sample preparation and test protocols, will be outlined. Subsequently, the results of the experiments and discussion of the results will be presented. The results presented in this Chapter have been partially published in Ref. [1].

5.1: Introduction to Graphene and Fluorinated Graphene

To gain more fundamental understanding of friction, graphene has proved to be an excellent material of choice for a number of reasons. First and most importantly, many studies on graphene to date have demonstrated promising friction-reducing properties even at thicknesses of one atomic layer [2-7]. Second, it is the thinnest known stable

material, the strongest ever measured, among many other superlative properties, making it interesting for both fundamental research and engineering applications. It is currently the most well-studied example of an isolated 2-D material. The special combination of these properties, along with high chemical stability and low friction and wear for graphene-treated surfaces [5], makes graphene an outstanding candidate for many other tribological applications.

To date, nearly all friction studies on graphene friction have been performed on pristine graphene, and as the material is relatively novel, only a few groups have reported experimental [8-16] or simulation [13, 17-21] studies of chemically functionalized graphene. There are several reasons for studying graphene derivatives. First, pristine graphene is a zero-band-gap semiconductor [22], whereas for many electronic applications, it is more desirable to have materials with a band gap, or even better, a tunable band gap. Inspired by the success of chemical modification of carbon nanotubes [23], similar treatments have been exploited to create a tunable band gap in graphene's energy spectrum. It has been demonstrated that a band gap opening can be induced by adsorption of atomic hydrogen on graphene [24, 25]. Another candidate was graphene oxide [26], although it is reported to be less energetically stable [27, 28]. Recently, because of its strong electronegativity, fluorination has been adopted as stable way of chemically functionalizing the carbon scaffold of graphene [29, 30].

FG, obtained by reacting graphene with xenon difluoride (XeF_2) gas, has a wide band gap that is as high as 2.9-3.0 eV depending on degree of fluorination [9, 10]. Several novel electronic applications have been reported based on FG [8, 16, 31]. Specifically, Robinson *et al.* observed that upon fluorination of graphene, it became

optically transparent, and that the electrical conductance decreased by 6 orders of magnitude. Other studies include Nair *et al.* [9] and Withers *et al.* [16], also synthesized FG and demonstrated the promising capabilities of tuning its electronic properties. Second, it is well known that macroscopic graphite fluoride is an excellent solid lubricant whose tribological properties can out-perform bulk graphite. Additionally, at the macroscale, it has been shown that adding fluorine atoms will make carbon-based materials more hydrophobic and reduces friction, which is the case with polytetrafluoroethylene [32]. However, at the nanoscale it is less clear whether the same trend can be observed when adding fluorine to graphene membranes.

Prior studies by Kwon *et al.* observed an increase of 6× in friction between a TiN coated AFM tip on graphene upon fluorination, which was hypothesized to be caused by damping effect via flexural phonons which in turn increased the out-of-plane stiffness of graphene resulting in higher friction [12]. In simulation results based on the density-functional theory, Leenaerts *et al.*'s calculations showed that both the Young's modulus, *E*, and the Poisson's ratio, *v*, of FG are smaller than those of pristine graphene, which in theory would result in lower bending stiffness for FG [18]. This result is contradicting Kwon *et al.*'s results and their DFT calculation. Additionally, they have also suggested that the discrepancy between the calculated elastic constants (*E* and *v*) and experimentally measured are likely to be caused by the presence of atomic defects in experiments. In their simulation study, Wang *et al.* found a low friction behavior between two FG layers in a shearing motion due to the low interlayer interaction induced by the electronegativity of F atoms, although no direct comparison with pristine graphene has been made [21].

From these studies, we see that the underlying mechanism for causing changes in frictional behavior of FG is not conclusive, and thus more study is needed. To date, it is also not clear how chemical modification affects the puckering mechanism seen in of atomically thin graphene films, as reported by Lee *et al.* [4] and discussed in Chapter 4 of this thesis. Additionally, the friction properties of silicon tips sliding against fluorinated graphene samples with various degree of fluorination will be studied to examine the influence of fluorine content on friction and other key mechanical properties. The atomic structures of graphene, partially fluorinated FG, and fully fluorinated FG are shown in Figure 5.1.

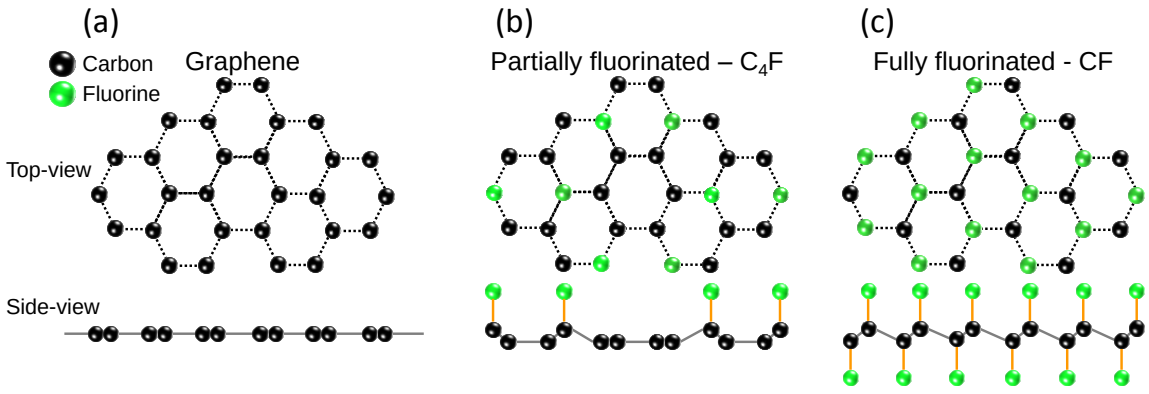

Figure 5.1: Atomic structures of (a) graphene, (b) partially fluorinated graphene, and (c) fully fluorinated graphene. Black spheres represent carbon atoms and green spheres represent fluorine atoms. Note the hexagonal structure of graphene is retained after fluorination, although the perfectly planar structure is lost due to the different bonding properties between C-C bonds and C-F bonds, resulting in out-of-plane deformation. Note that the structures illustrated here only represent ordered fluorination.

5.2 Experimental Details

5.2.2: Sample Preparation

Graphene and FG samples were prepared by Dr. J. Robinson (U.S. Naval Research Laboratory, Washington, D.C.). The methodology for fluorination follows the same methodology as described in Ref. [10]. Briefly, graphene films were grown on copper foils using CVD, then transferred to SiO_2/Si substrates [33]. Transferred graphene samples were then coated with a photo-resist layer that was then patterned. The sample was then exposed to 1 Torr XeF_2 and 35 Torr N_2 carrier gas in pulse mode at approximately 30° C in a Xactix® XeF_2 etching system (SPTS Technologies Inc., Newport, UK). As the coated regions were protected by photo-resist, only the uncoated regions were fluorinated. After XeF_2 exposure, the resist was removed in a short (~1 min.) acetone soak. After resist removal, pristine graphene regions are characterized side-by-side with fluorinated regions by optical microscopy, Raman spectroscopy, and AFM, allowing for a direct comparison of the influence of fluorination on the structure and mechanical properties on the films. The entire preparation is schematically shown in Figure 5.2.

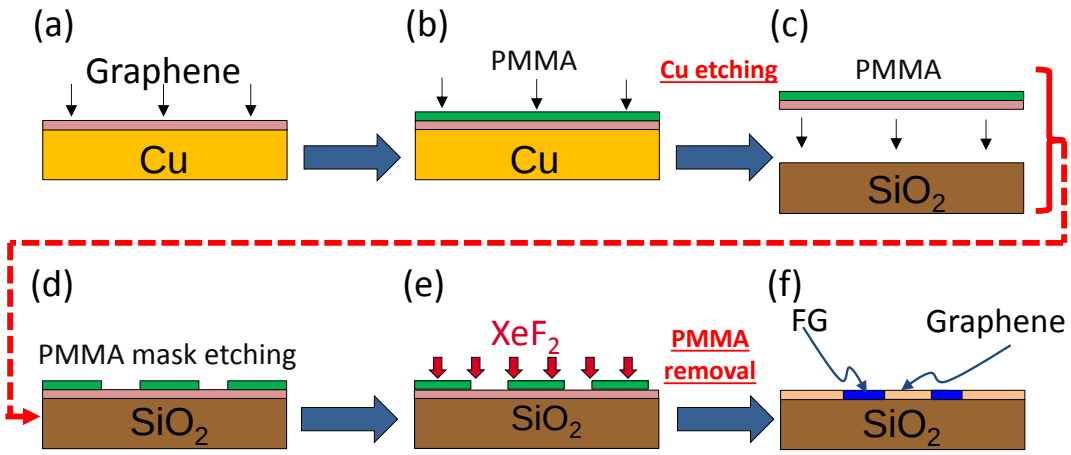

Figure 5.2: Sample preparation steps: (a)-(c) CVD graphene grown on Cu foil and transferred onto SiO_2/Si substrate. (d) PMMA mask was locally patterned. (e) Graphene on SiO_2/Si was selectively etched by XeF_2 gas; (f) after lift-off, pristine and fluorinated graphene were obtained side-by-side on substrate.

5.2.1: Experimental Protocol

Optical microscopy was first used to examine the optical contrast that developed as a result of graphene fluorination. Following this step, the samples were inserted in the Raman spectrometer with an excitation laser wavelength of 532 nm used to investigate the carbon properties of graphene and FG. For friction studies, two AFM systems were used. First, the RHK 350 AFM was used for its high force and displacement resolution, and second, the Asylum AFM was used for its large scan range. All measurements are performed in dry nitrogen environment (<2% RH). Load-dependent friction experiments were performed by unloading the normal force from high to low until pull-off occurs, while the lateral force signal was monitored simultaneously. For all experiments, contact mode AFM silicon cantilever probes (CSC 37, Mikromash Inc.) were used. The normal

force constant of the cantilevers was calibrated by the Sader method [34]. For lateral force calibration, for the RHK 350 AFM, the D-LFC method was used [35]. For the Asylum AFM, due to the spatial constraints of the fluid cell and the magnetic tip holder, the Sader lateral calibration method was used instead [36].

5.3: MD Simulation Protocol

To further identify the mechanism of friction enhancement due to fluorination, MD simulations of a nanoscale tip sliding on a fluorinated graphene surface were performed. These simulations were conducted using LAMMPS code [37] and the reactive force-field (ReaxFF) [38, 39] by Prof. Shenoy and his group. Specifically, a hemispherical Pt(111)-terminated asperity consisting of 1,626 atoms was slid over graphene or FG samples, which were supported by a stepped Pt(181) surface consisting of 5,280 atoms at 10 K of low temperature. The stepped Pt(181) surface qualitatively mimicked the atomic-level roughness of the SiO_2 substrate used in the experiments. The radius of the Pt tip was 2.3 nm, and the size of the Pt substrate was approximately $10\times6\times1.2$ nm^3 (length × width × height). Periodic boundary conditions were enforced at the edges along lateral directions. In the simulations, the inter-atomic interaction in fluorinated carbon systems was described by the ReaxFF potential [38] and the charge transfer effect was determined using the charge equilibration (QEq) method [40] at every MD step. The temperature of the system was controlled by the Berendsen thermostat, which rescales atom velocities every time step. The normal load was controlled by adjusting the initial tip height from the film, and the topmost 3 layers of the tip atoms were allowed to move only along the sliding direction to prevent rotation of the tip during

sliding. A virtual atom is introduced at 40 Å ahead of the tip and connected through a linear spring to mimic the lateral compliance of the AFM system. The simulation models used for both FG (specifically, C_4F) and pristine graphene are shown in Figure 5.3.

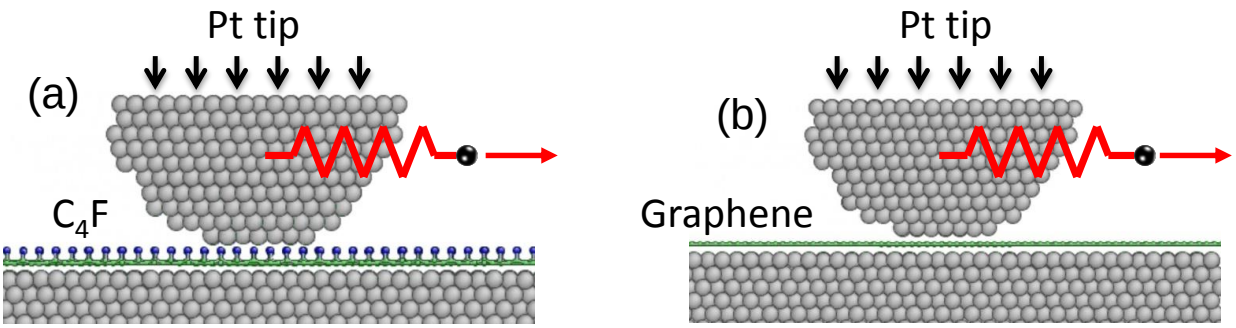

Figure 5.3: Two snapshots of MD simulations during tip sliding from left to right. The red arrows indicate the scan direction. The black arrows indicate the direction of the normal load. (a) C_4F and (b) pristine graphene.

5.4: Results

5.4.1: Optical Properties

Figure 5.4 (a) shows an optical image of a typical FG sample on the SiO_2/Si substrate. Because of the insulating nature of FG, regions that were exposed to XeF_2 fluorination appeared almost optically transparent, as described in Ref. [40], in contrast to the un-fluorinated (pristine) graphene regions that were protected by photo-resist. Within the fluorinated regions, one can observe some distributed purplish islands. These are multi-layer fluorinated graphene regions, as reported previously [10].

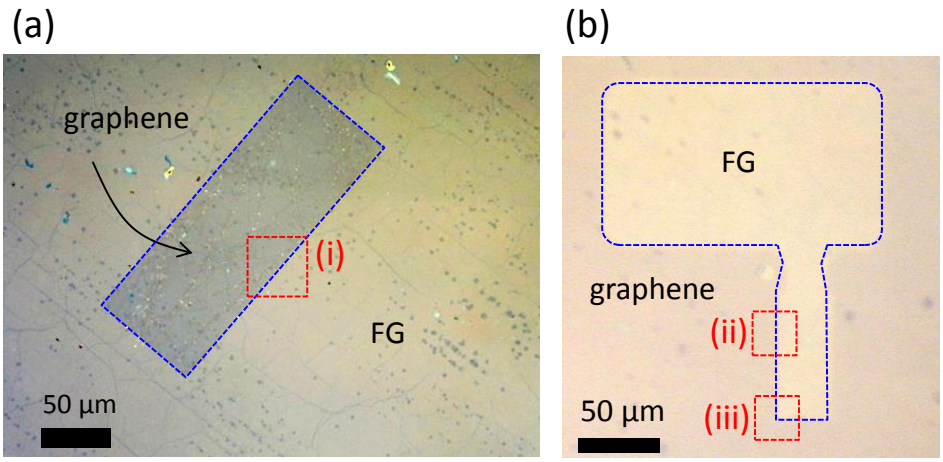

Figure 5.4: (a) Optical image of graphene and FG after 10 minute XeF_2 exposure. Small purplish islands are multi-layer fluorinated graphene regions. (b) Optical image of graphene and FG after 1 minute XeF_2 exposure. Blue boxes are drawn to better indicate the graphene-FG boundary.

5.4.2: Raman Spectroscopic Properties on Graphene and FG

Figure 5.5 (a) shows a Raman D peak map of the area containing both FG and pristine graphene. On the fluorinated area, shown in the blue box, the D peak signal is significantly higher, indicating a significant presence of defects. In order to better understand the influence of fluorination time on the properties of graphene, we examples samples where the degree of fluorination was systematically varied by controlling the XeF_2 gas exposure time, ranging from 60 sec to 1200 sec. We then measured the corresponding Raman spectra. Figure 5.5 (b) shows a set of representative Raman spectra taken on both pristine graphene and FG samples. Clearly, after 60 sec of fluorination, one can observe a pronounced increase of the D peak compared to the spectrum taken on pristine graphene, indicating that the hexagonal carbon structure of pristine graphene has been altered. As the fluorination progresses, the intensity of the 2D peak is suppressed

and the D peak emerges further, indicating that the material is becoming increasingly more fluorinated. Based on this Raman data, we therefore conclude that the enhancement of defects in FG depends sensitively on the relative degree of fluorination of graphene.

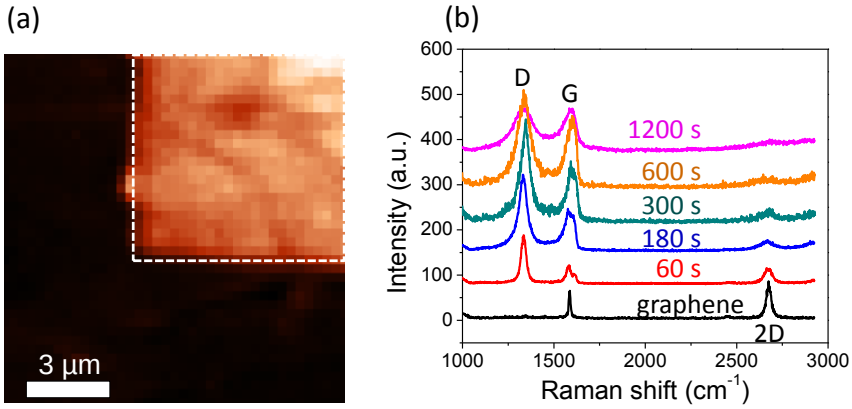

Figure 5.5: (a) Raman D peak map of the area indicated with red box (iii) in Figure 5.3 (b). (b) Raman spectra of graphene with various degrees of fluorination. For pristine graphene (black spectrum), the ratio between the 2D and G peak intensities indicates that the region consists of a single layer graphene [41]. As soon as the fluorination begins, a clear D peak appears, signifying the presence of defects due to fluorination. As the exposure time further increases, the intensity of 2D peak is suppressed and the D peak emerges, indicating that graphene is becoming more fluorinated.

5.4.3: Frictional Properties on Graphene and FG

AFM data acquired across a graphene-FG boundary is shown in Figure 5.6 (a) for topography, and (b) and (c) for friction. These data clearly demonstrate that friction on FG is much higher than that on graphene. High-resolution atomic stick-slip friction data were also acquired across a scan range of a few nanometers. The results are shown in Figure 5.6 (d) and (e) for graphene and FG, respectively. Figure 5.6 (d) shows that the

pristine graphene area exhibits a regular atomic stick-slip pattern, indicating a highly ordered graphene surface. In contrast, Figure 5.6 (e) shows no regular stick-slip friction pattern, suggesting that fluorination has destroyed the regularity of the graphene surface. Thus, both friction enhancement and the increase in disorder depend directly and sensitively on the degree of fluorination of graphene.

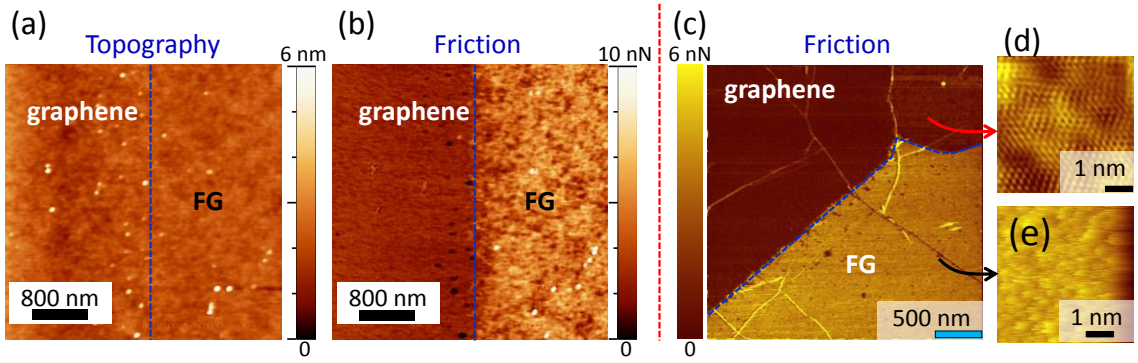

Figure 5.6: AFM topography and AFM friction map scanned on the area indicated with the red box (i) in Figure 5.4 (a). (a) Topography image from which it is clear that fluorination does not modify the roughness or topography of the area, (b) The corresponding friction signal taken at the same area. Darker region corresponds to lower friction forces. (c) Friction image collected on a different area. (d) High-resolution lateral force image acquired on the pristine graphene in (c), atomic stick-slip friction can be resolved with a periodic lattice, indicating the surface is highly ordered. (e) High-resolution lateral force image taken on FG. The absence of stick-slip friction on FG suggests that fluorination has destroyed the regularity of the graphene surface.

For a better quantitative comparison, we located the probe at an edge of graphene-FG boundary and let it scan repeatedly along a horizontal line crossing that boundary. A representative set of friction *vs.* normal load measurements collected simultaneously on graphene and FG is shown in Figure 5.7 (a). By performing linear fits on the friction data,

the effective nanoscale friction coefficient can be found for FG, denoted by μ_{FG}, and for graphene, denoted by $\mu_{graphene}$. Comparing the two, one can see that μ_{FG} is 6 times greater than $\mu_{graphene}$, for the particular sample we measured. In the same manner, we performed friction *vs.* load tests on samples of various fluorination times, and extracted μ_{FG} and $\mu_{graphene}$, and plotted the ratios between them in Figure 5.7 (b) as a function of fluorination time. For samples exposed to XeF_2 for 150 sec or longer, Figure 5.7 (b) has a slope of 0.28±0.02 min^{-1}, indicating that each unit increase in friction ratio corresponds to 3.6 minutes of exposure or roughly a 13% increase in F/C ratio based on recent XPS studies [42].

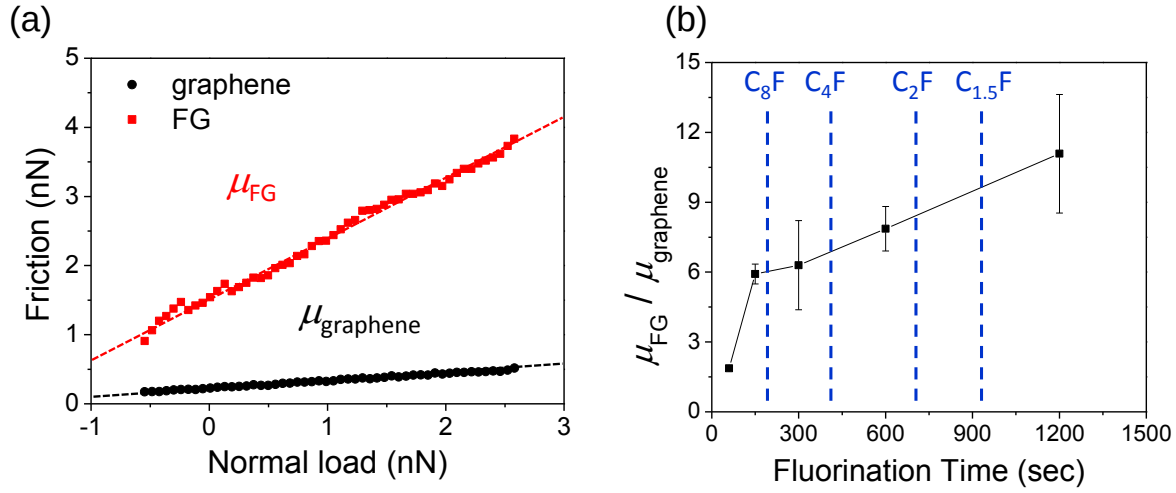

Figure 5.7: Friction *vs.* load data acquired across the graphene-FG boundary. Comparison of friction *vs.* normal load data sets plotted obtained by AFM experimental data. The slope of the two data sets are fit by a linear function, revealing a 6 times difference for friction coefficients between FG and pristine graphene. (b) Ratio of measured coefficient of friction (from linear fits to respective friction *vs*. normal load plots) between fluorinated graphene and graphene, as a function of fluorination time. Labeled vertical lines indicate specific stoichiometries determined from X-ray photoelectron spectroscopy (XPS) for corresponding fluorination times [42].

5.4.3: MD Simulation Results

MD simulations were performed for a nanoscale tip sliding on graphene sheets as a function of atomic content of fluorine on graphene at three different constant normal loads: pristine graphene, C_8F, and C_4F, representing increasing fluorination times. Figure 5.8 (a) shows the variation of friction with normal load for these simulations. Consistent with experiments, friction on all FG samples is much higher than on pristine graphene; the effective $\mu_{FG}/\mu_{graphene}$ ratio ranges from 7.3-8.0.

We then calculated the interaction energy between the tip and the sample as we varied the tip position. Three contour plots representing the spatial variation of tip-sample interaction energy for pristine graphene, C_8F, C_4F, and C_2F are shown (Figure 5.8 (c)-(f)). We extracted the local amplitude of the potential energy variation (the energy corrugation) and plotted it against the atomic fluorine content (Figure 5.8 (b)), illustrating a strong dependence. For example, at 0 nN applied load, pristine graphene exhibits a corrugation of only 12.9 meV, while the corrugation of C_8F is 206 meV, 15 times larger.

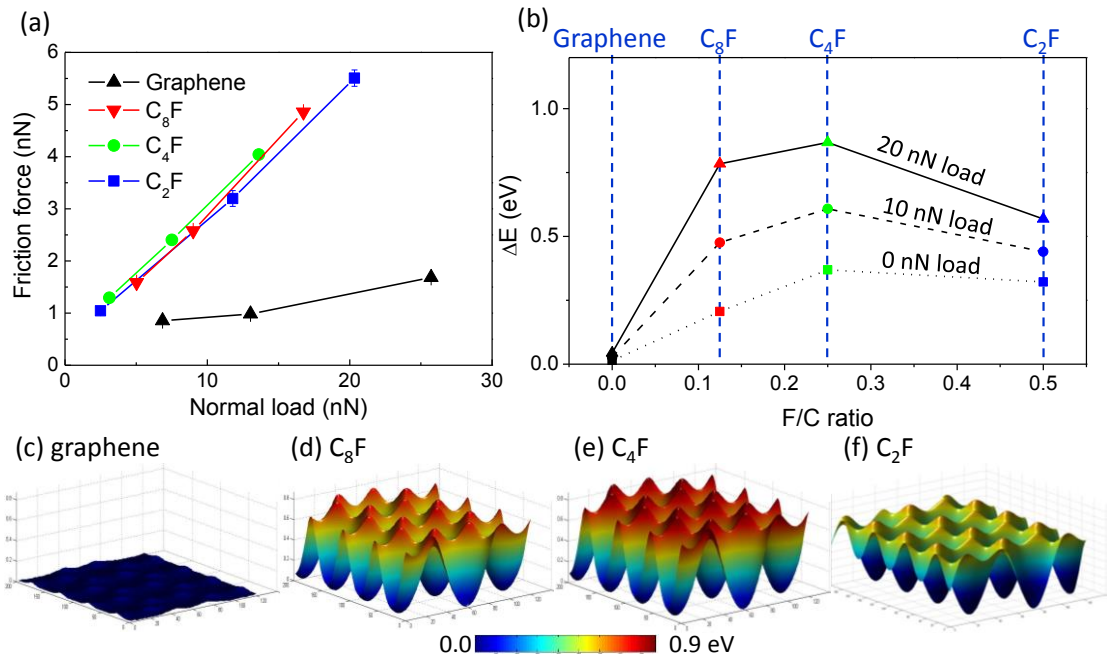

Figure 5.8: Results from MD simulations. (a) Friction as a function of normal load for pristine graphene, C_8F, C_4F, and C_2F. A strong increase in friction occurs once the graphene is fluorinated. Additional fluorination does not affect the friction further. Overall $\mu_{FG}/\mu_{graphene}$ ratio ranges between 7.3-8.0. (b) Corrugation amplitude of the potential energy as a function of atomic content of fluorine on graphene from the simulations in (a), calculations performed at 3 different loads: 0, 10, and 20 nN. (c)-(f) Contour maps of the tip-sample potential energy for the same samples. Each map is shown for an area of ~0.7×1.0 nm^2. The color scale for all three maps covers the range 0-0.9 eV.

5.5: Discussion

First, from the experimental point of view, we can rule out the influence of the relative humidity. Indeed, since the relative humidity was always kept very low in our system (< 2% RH), and given the hydrophobic nature of the fluorinated surface compared to graphene [9], we therefore rule out that the significant increase of friction was

somehow a result of capillary condensation on FG [43]. Second, we consider the puckering mechanism. Puckering of atomically-thin films has been identified as a mechanism for extra frictional dissipation observed on two-dimensional for the following two reasons: (a) a lower bending stiffness would lead to more puckering. However, the out-of-plane bending rigidity of FG is not significantly lower than that of graphene or may even be higher [9, 11], and from the MD results, there was no indication of puckering of FG in front of the sliding tip, as evident from Figure 5.3 (a). This excludes the puckering effect [4] as a mechanism for the observed friction enhancement. (b) Higher adhesion would lead to more puckering. However, the adhesion on FG was not significantly different that on graphene as confirmed by our experimental measurements and MD simulations.

Given that aforementioned mechanisms for friction enhancement on FG in comparison to pristine graphene will not yield the observed friction contrast, the increased energy corrugation for FG, as determined from MD simulations, emerges as a likely the mechanism for the recorded variation in friction. The relationship between friction and energy corrugation has been extensively discussed in previous studies [44-46]. The underlying physical behavior is explained by the PT [47] model which describes a spring-coupled entity sliding in a rigid one dimensional sinusoidal potential at zero temperature as discussed in Chapter 2. A transition from smooth, low friction sliding to unstable, higher friction occurs when the corrugation energy along the sliding direction E_0 exceeds $ka^2/2\pi^2$, where k is the lateral contact stiffness at the tip-sample interface, and a is the lattice constant. In the stick-slip regime, the static friction F_f (the force at which slip occurs) is equal to $\pi E_0/a$. Indeed, for the MD results, $aF_f/\pi E_0$ is in the range of 2-5,

consistent with Ref. [51] and the idea that the PT model is a reasonable framework. We deem the MD simulations to be reliable, as they reproduced the experimental finding of greatly increased peak friction with increased fluorination. While care should be taken in comparing MD simulations with AFM experiments, Li *et al*. [48] recently showed very good agreement between energetic parameters, specifically the energy corrugation extracted from MD simulations and well-matched experiments.

The enhanced corrugation is readily explained by the high electronegativity of the fluorine atoms. The highly localized negative charge over F atoms as well as their geometric protrusion above the carbon basal plane leads to a strong local variation in the interfacial potential energy at fluorinated sites. Density functional theory calculations [21] have recognized that the electrostatic interaction originating from the polarized bonds between carbon and functional groups will dominate over the van der Waals interaction by altering the potential energy surface which in turn affects the friction behavior accordingly. Our results are also qualitatively consistent with the aforementioned MD simulations of hydrogenated graphene by Dong *et al.* [49], who predicted that partially hydrogenating the upper surface of graphene will increase friction, although no experimental data in vacuum have been reported to verify this prediction. Dong *et al.* found that increased friction was unrelated to changes in adhesion or film elasticity, but rather, was due to increased potential corrugation induced by the H atoms. Fessler *et al.* reported that hydrogenation increases friction for graphene and attributed this increase to hydrogenation-induced contamination. Cleaning the surface with the AFM tip reduces contamination and hence decreases the friction [50]. Here, we

extensively scanned the area of interest prior to friction measurements. We therefore do not expect this cleaning effect to affect the observed friction contrast.

Moreover, regarding the order of fluorination in MD, it is observed that the regular distribution of F atoms on graphene adopted in the simulations led to friction traces and energy corrugation maps that exhibit ordered patterns, as shown Figure 5.8 (a). This is in contrast to the disordered image of the FG sample as seen in experiments, shown in Figure 5.8 (f), where no regular stick-slip pattern was observed. To see the order-dependent frictional characteristics, disordered C_4F is prepared by attaching F atoms with the number of 0.25 F/C ratio on the graphene where the sites are randomly selected. As shown in Figure 5.9 (b), the profile has an irregular pattern which is different from the case using ordered FG samples but the overall shape is similar to the experimental results, consistent with the hypothesis that fluorine atoms would be randomly distributed on the graphene sites. The maximum peak friction becomes lower for the case of d-C_4F due to the irregularity induced frictional scattering, but the value is still higher than that of pristine graphene. Müser *et al.* have shown using generic atomistic simulations and a scaling analysis that, for atomically-flat surfaces, disordered surfaces exhibit higher friction than ordered surfaces that are otherwise chemically identical [51]. Indeed, Dong *et al.*'s results [49] show that disordered arrangements of H atoms can greatly increase friction on graphene. Therefore, despite differences between simulations and experiments in the arrangement of F atoms, both are consistent with the hypothesis that fluorination greatly increases friction because of the corrugation induced by localized charge.

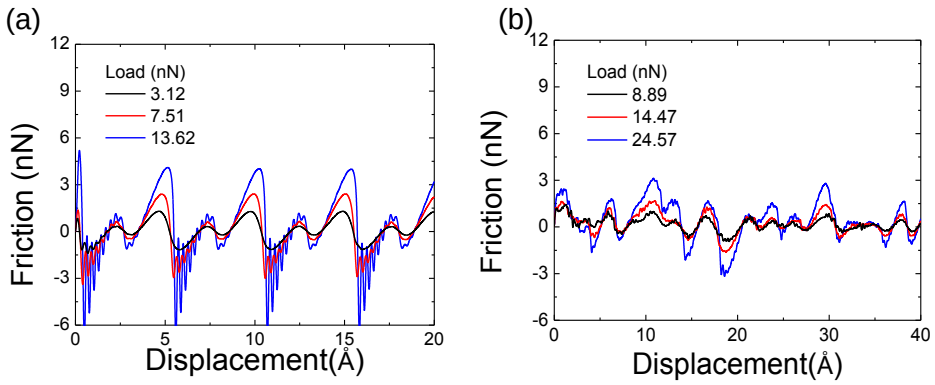

Figure 5.9: Simulation results for C_4F. (a) Friction traces obtained in MD simulations of sliding on ordered FG and graphene. Consistent with the experimental observations, the simulation results indicate that friction on FG samples is much higher than that on pristine graphene. Because of the regular distribution of F atoms on graphene, the friction profile shows ordered pattern for FG samples that is different from the experiments. (b) The line profiles of the friction force for disordered C_4F as a function of normal load.

Finally, from that the simulation results shown in Figure 5.8 (a), (b), and (f), it is noted that the MD results suggest that the energy corrugation and μ_{FG} reduce slightly when F/C ratio exceeds 0.25 and approaching 0.5. No corresponding reduction in friction was observed in our experiments for these fluorination levels. The inconsistency could be related to aging effects of the sample (*i.e.* slow desorption of fluorine, as reported by Stine *et al.* [42]) during measurements or the ideally simplified, well-ordered FG structure we adopted in our simulations. Another possibility is that at long fluorination time, the F content is sufficiently high such that it essentially forms another layer completely covering graphene. A similar trend has been observed for hydrogenation of diamond surfaces [52]. More studies are needed to fully explore this effect for fluorination of graphene.

5.6: Summary

In conclusion, we find that friction on FG strongly depends on the relative degree of fluorination, with increasing fluorination leading to higher friction. Moreover, no ordered lattice in atomic stick-slip friction can be resolved on FG, indicating that the FG is disordered. This effect is attributed to significantly altered energy landscape experienced by the tip due to fluorination. Static friction rises in proportion to this energy barrier, in accordance with the Prandtl-Tomlinson model. These results provide the first insights into the atomic-scale effects of functionalization on friction properties of graphene; and more importantly, they suggest a potential approach to sensitively probe the local chemistry and structure of functionalized graphene. Finally, we observed that fluorination of graphene surfaces provides a pathway to alter the shear strength of graphene-tip interfaces.

5.7: References

1. Q. Li, X.-Z. Liu, S.-P. Kim, V.B. Shenoy, P.E. Sheehan, J.T. Robinson, and R.W. Carpick, Fluorination of graphene enhances friction due to increased corrugation. *Nano Letters* **2014**, 5212–5217.
2. T. Filleter, J.L. McChesney, A. Bostwick, E. Rotenberg, K.V. Emtsev, T. Seyller, K. Horn, and R. Bennewitz, Friction and dissipation in epitaxial graphene films. *Physical Review Letters* **2009**, 102(8), 086102.
3. K.-S. Kim, H.-J. Lee, C. Lee, S.-K. Lee, H. Jang, J.-H. Ahn, J.-H. Kim, and H.-J. Lee, Chemical vapor deposition-grown graphene: The thinnest solid lubricant. *ACS Nano* **2011**, 5107–5114.
4. C. Lee, Q. Li, W. Kalb, X.-Z. Liu, H. Berger, R.W. Carpick, and J. Hone, Frictional characteristics of atomically thin sheets. *Science* **2010**, 328(5974), 76.
5. D. Berman, A. Erdemir, and A.V. Sumant, Reduced wear and friction enabled by graphene layers on sliding steel surfaces in dry nitrogen. *Carbon* **2013**, 59, 167-175.

6. P. Egberts, G.H. Han, X.Z. Liu, A.T.C. Johnson, and R.W. Carpick, Frictional behavior of atomically thin sheets: Hexagonal-shaped graphene islands grown on copper by chemical vapor deposition. *ACS Nano* **2014**, 5010–5021.
7. J.Y. Park, S. Kwon, and J.H. Kim, Nanomechanical and charge transport properties of two-dimensional atomic sheets. *Advanced Materials Interfaces* **2014**, 1(3), 28.
8. S.H. Cheng, K. Zou, F. Okino, H.R. Gutierrez, A. Gupta, N. Shen, P.C. Eklund, J.O. Sofo, and J. Zhu, Reversible fluorination of graphene: Evidence of a two-dimensional wide bandgap semiconductor. *Physical Review B* **2010**, 81(20), 205435.
9. R.R. Nair, W. Ren, R. Jalil, I. Riaz, V.G. Kravets, L. Britnell, P. Blake, F. Schedin, A.S. Mayorov, S. Yuan, M.I. Katsnelson, H.M. Cheng, W. Strupinski, L.G. Bulusheva, A.V. Okotrub, I.V. Grigorieva, A.N. Grigorenko, K.S. Novoselov, and A.K. Geim, Fluorographene: a two-dimensional counterpart of Teflon. *Small* **2010**, 6(24), 2877-84.
10. J.T. Robinson, J.S. Burgess, C.E. Junkermeier, S.C. Badescu, T.L. Reinecke, F.K. Perkins, M.K. Zalalutdniov, J.W. Baldwin, J.C. Culbertson, and P.E. Sheehan, Properties of fluorinated graphene films. *Nano Letters* **2010**, 8, 3001-3005.
11. F. Withers, T.H. Bointon, M. Dubois, S. Russo, and M.F. Craciun, Nanopatterning of fluorinated graphene by electron beam irradiation. *Nano Letters* **2011**, 11(9), 3912-6.
12. S. Kwon, J.-H. Ko, K.-J. Jeon, Y.-H. Kim, and J.Y. Park, Enhanced nanoscale friction on fluorinated graphene. *Nano Letters* **2012**, 6043-6048.
13. C.-H. Hu, P. Zhang, H.-Y. Liu, S.-Q. Wu, Y. Yang, and Z.-Z. Zhu, Structural stability and electronic and magnetic properties of fluorinated bilayer graphene. *The Journal of Physical Chemistry C* **2013**, 3572-3579.
14. J.-H. Ko, S. Kwon, I.-S. Byun, J.S. Choi, B.H. Park, Y.-H. Kim, and J.Y. Park, Nanotribological properties of fluorinated, hydrogenated, and oxidized graphenes. *Tribology Letters* **2013**, 137-144.
15. W.-K. Lee, M. Haydell, J.T. Robinson, A.R. Laracuente, E. Cimpoiasu, W.P. King, and P.E. Sheehan, Nanoscale reduction of graphene fluoride via thermochemical nanolithography. *ACS Nano* **2013**, 6219-6224.
16. F. Withers, M. Dubois, and A.K. Savchenko, Electron properties of fluorinated single-layer graphene transistors. *Physical Review B* **2010**, 82(7), 073403.
17. S.S. Han, T.H. Yu, B.V. Merinov, A.C.T. van Duin, R. Yazami, and W.A. Goddard, Unraveling structural models of graphite fluorides by density functional theory calculations. *Chemistry of Materials* **2010**, 22(6), 2142-2154.

18. O. Leenaerts, H. Peelaers, A. Hernández-Nieves, B. Partoens, and F. Peeters, First-principles investigation of graphene fluoride and graphane. *Physical Review B* **2010**, 82(19), 195436.
19. H. Şahin, M. Topsakal, and S. Ciraci, Structures of fluorinated graphene and their signatures. *Physical Review B* **2011**, 83(11), 115432.
20. Y. Li, F. Li, and Z. Chen, Graphane/Fluorographene bilayer: considerable C-H...F-C hydrogen bonding and effective band structure engineering. *Journal of the American Chemical Society* **2012**, 134(27), 11269-75.
21. L.-F. Wang, T.-B. Ma, Y.-Z. Hu, H. Wang, and T.-M. Shao, Ab initio study of the friction mechanism of fluorographene and graphane. *The Journal of Physical Chemistry C* **2013**, 12520–12525.
22. A.H. Castro Neto, F. Guinea, N.M.R. Peres, K.S. Novoselov, and A.K. Geim, The electronic properties of graphene. *Reviews of Modern Physics* **2009**, 81(1), 109-162.
23. Y.P. Sun, K.F. Fu, Y. Lin, and W.J. Huang, Functionalized carbon nanotubes: Properties and applications. *Accounts of Chemical Research* **2002**, 35(12), 1096-1104.
24. D.C. Elias, R.R. Nair, T.M.G. Mohiuddin, S.V. Morozov, P. Blake, M.P. Halsall, A.C. Ferrari, D.W. Boukhvalov, M.I. Katsnelson, and A.K. Geim, Control of graphene's properties by reversible hydrogenation: Evidence for graphane. *Science* **2009**, 323(5914), 610.
25. R. Balog, B. Jorgensen, L. Nilsson, M. Andersen, E. Rienks, M. Bianchi, M. Fanetti, E. Laegsgaard, A. Baraldi, S. Lizzit, Z. Sljivancanin, F. Besenbacher, B. Hammer, T.G. Pedersen, P. Hofmann, and L. Hornekaer, Bandgap opening in graphene induced by patterned hydrogen adsorption. *Nature Materials* **2010**, 9(4), 315-319.
26. Z. Luo, Y. Lu, L.A. Somers, and A.T.C. Johnson, High yield preparation of macroscopic graphene oxide membranes. *Journal of the American Chemical Society* **2009**, 131(3), 898-899.
27. D. Dikin, S. Stankovich, E. Zimney, R. Piner, G. Dommett, G. Evmenenko, S. Nguyen, and R. Ruoff, Preparation and characterization of graphene oxide paper. *Nature* **2007**, 448(7152), 457-460.
28. I. Jung, D.A. Dikin, R.D. Piner, and R.S. Ruoff, Tunable electrical conductivity of individual graphene oxide sheets reduced at "low" temperatures. *Nano Letters* **2008**, 8(12), 4283-7.

29. D. O'Hagan, Understanding organofluorine chemistry. An introduction to the C-F bond. *Chemical Society Reviews* **2008**, 37(2), 308-319.
30. H.Y. Liu, Z.F. Hou, C.H. Hu, Y. Yang, and Z.Z. Zhu, Electronic and magnetic properties of fluorinated graphene with different coverage of fluorine. *Journal of Physical Chemistry C* **2012**, 116(34), 18193-18201.
31. K.-I. Ho, C.-H. Huang, J.-H. Liao, W. Zhang, L.-J. Li, C.-S. Lai, and C.-Y. Su, Fluorinated graphene as high performance dielectric materials and the applications for graphene nanoelectronics. *Scientific Reports* **2014**, 4, 7.
32. I. Woodward, W.C.E. Schofield, V. Roucoules, and J.P.S. Badyal, Super-hydrophobic surfaces produced by plasma fluorination of polybutadiene films. *Langmuir* **2003**, 19(8), 3432-3438.
33. X.L. Li, X.R. Wang, L. Zhang, S.W. Lee, and H.J. Dai, Chemically derived, ultrasmooth graphene nanoribbon semiconductors. *Science* **2008**, 319(5867), 1229-1232.
34. J.E. Sader, J.W.M. Chon, and P. Mulvaney, Calibration of rectangular atomic force microscope cantilevers. *Review of Scientific Instruments* **1999**, 70(10), 3967-3969.
35. Q. Li, K.S. Kim, and A. Rydberg, Lateral force calibration of an atomic force microscope with a diamagnetic levitation spring system. *Review of Scientific Instruments* **2006**, 77(6), 065105.
36. C.P. Green, H. Lioe, J.P. Cleveland, R. Proksch, P. Mulvaney, and J.E. Sader, Normal and torsional spring constants of atomic force microscope cantilevers. *Review of Scientific Instruments* **2004**, 75(6), 1988.
37. S. Plimpton, Fast parallel algorithms for short-range molecular dynamics. *Journal of Computational Physics* **1995**, 117(1), 1-19.
38. A.C.T. van Duin, S. Dasgupta, F. Lorant, and W.A. Goddard, ReaxFF: A reactive force field for hydrocarbons. *The Journal of Physical Chemistry A* **2001**, 105(41), 9396-9409.
39. S.K. Singh, S.G. Srinivasan, M. Neek-Amal, S. Costamagna, A.C.T. van Duin, and F.M. Peeters, Thermal properties of fluorinated graphene. *Physical Review B* **2013**, 87(10), 104114.
40. A.K. Rappe and W.A. Goddard, Charge equilibration for molecular dynamics simulations. *The Journal of Physical Chemistry* **1991**, 95(8), 3358-3363.
41. A.C. Ferrari, J.C. Meyer, V. Scardaci, C. Casiraghi, M. Lazzeri, F. Mauri, S. Piscanec, D. Jiang, K.S. Novoselov, S. Roth, and A.K. Geim, Raman spectrum of graphene and graphene layers. *Physical Review Letters* **2006**, 97(18), 187401.

42. R. Stine, W.-K. Lee, K.E. Whitener, Jr., J.T. Robinson, and P.E. Sheehan, Chemical stability of graphene fluoride produced by exposure to XeF_2. *Nano Letters* **2013**, 13(9), 4311-6.
43. I.-S. Byun, D. Yoon, J.S. Choi, I. Hwang, D.H. Lee, M.J. Lee, T. Kawai, Y.-W. Son, Q. Jia, H. Cheong, and B.H. Park, Nanoscale lithography on monolayer graphene using hydrogenation and oxidation. *ACS Nano* **2011**, 5(8), 6417-6424.
44. A. Socoliuc, R. Bennewitz, E. Gnecco, and E. Meyer, Transition from stick-slip to continuous sliding in atomic friction: entering a new regime of ultralow friction. *Physical Review Letters* **2004**, 92(13), 134301.
45. S.Y. Krylov and J.W.M. Frenken, Thermal contact delocalization in atomic scale friction: a multitude of friction regimes. *New Journal of Physics* **2007**, 9(10), 398-398.
46. N.N. Gosvami, T. Filleter, P. Egberts, and R. Bennewitz, Microscopic friction studies on metal surfaces. *Tribology Letters* **2009**, 39(1), 19-24.
47. C.M. Mate, *Tribology on the Small Scale: A Bottom Up Approach to Friction, Lubrication, and Wear*; Oxford University Press: New York, 2008.
48. Q. Li, Y. Dong, D. Perez, A. Martini, and R.W. Carpick, Speed dependence of atomic stick-slip friction in optimally matched experiments and molecular dynamics simulations. *Physical Review Letters* **2011**, 106(12), 126101.
49. Y.L. Dong, X.W. Wu, and A. Martini, Atomic roughness enhanced friction on hydrogenated graphene. *Nanotechnology* **2013**, 24(37), 6.
50. G. Fessler, B. Eren, U. Gysin, T. Glatzel, and E. Meyer, Friction force microscopy studies on SiO2 supported pristine and hydrogenated graphene. *Applied Physics Letters* **2014**, 104(4), 041910.
51. M.H. Müser, L. Wenning, and M.O. Robbins, *Physical Review Letters* **2001**, 86, 1295.
52. P.L. Piotrowski, R.J. Cannara, G. Gao, J.J. Urban, R.W. Carpick, and J.A. Harrison, Atomistic factors governing adhesion between diamond, amorphous carbon and model diamond nanocomposite surfaces. *Journal of Adhesion Science and Technology* **2010**, 24(15-16), 2471-2498.

Chapter 6: Thermally-Activated Atomic-Scale Friction

Chapters 4 and 5 presented results which demonstrated that it is possible to alter adhesion and friction by changing the tip-graphene adhesive interaction and the real contact area, as well as by changing the interfacial potential energy landscape of the material via functionalization. This chapter transitions to a new topic. Rather than modifying the chemistry of the surface to vary the shear strength, the influence of the scanning speed and temperature will now be examined in detail to demonstrate their influence on the shear strength. This Chapter is organized with the following structure: first, prior studies on the speed and temperature dependence of atomic-scale friction will be reviewed. New results demonstrating the effect of friction by varying the speed of sliding, the content of which was published in Ref. [1], will then be presented. Finally, recent and preliminary results on the temperature dependence of friction will be discussed in the context of both previous literature and the results on speed dependent friction.

6.1: Introduction

In the PT model introduced in Chapter 2, the assumed temperature of the model was 0 K, which obviously is not accurate given that most experimental measurements of atomic stick-slip are conducted at room temperature (~300 K). Since the typical interfacial potential energy corrugation of approximately 1 eV was observed (obtained from fits to experimental data using the PT model [2]), the thermal energy at 300 K ($k_B T$ = 0.026 eV), while small, is not negligible and cannot be ignored in considering a comprehensive description of atomic-scale friction. To account for this additional source of energy, the PT model at finite temperature (the "PTT model") was developed. This

model has predictions for the speed dependence of atomic-scale friction [2-9] as well as the temperature dependence [5, 10-14]. However, the form of these variations depends on the speed or temperature range studied, and the underlying mechanisms remain a matter of debate. Furthermore, there exists a number of experimental studies showing that the PTT model is not widely applicable in atomic friction studies, because the mechanisms of thermally activated friction are still under debate. For example, the speed-dependence of friction was investigated by Zwörner *et al*. on various samples, including diamond and HOPG [9], and it was found that friction was insensitive to the speed. In another study, Barel *et al.* found that the speed dependence can be either increasing or decreasing depending on the system temperature [15]. Additionally, Bouhacina *et al.* and Gnecco *et al.* observed that $F_f \propto \text{const} + \ln(v)$ [2, 16], where F_f is friction and v is the scanning speed. Later, Sang *et al.* updated this model and derived that $F_f \propto \text{const}+\ln(v)^{3/2}$ [8]. Data by Riedo *et al.* were consistent with this model [4]. In this picture thermal activation is considered during atomic-scale sliding including the fact that the lateral force is increasing as the tip is sticking. The model predicts a saturation of the friction force at sufficiently high speeds. However, there are only two studies where stick-slip behavior was resolved while measuring friction as a function of temperature [3, 4]. Furthermore, the range of speeds examined in these studies is rather limited: ~μm/s. Thus, it is not well-established whether these thermally activated models are indeed accurate descriptions of atomic friction processes. The present work focuses on further investigation of the scanning speed dependence (the speed at which the sample is translated with respect to the fixed end of the cantilever) and the temperature dependence

of atomic stick-slip friction (the temperature of the specimen), which allow us to understand the laws of friction the atomic scale, and in turn possibly reveal the influence of speed and temperature on the shear strength of materials at contact interfaces.

Given the lack of validation of thermally activated atomic friction models, fundamental studies of friction where atomic stick-slip friction is observed over the complete parameter space examined is motivated. Atomic stick-slip friction is determined by the observation of stick-slip with lattice periodicity in lateral force measurements, which can then be analyzed to understand the elementary mechanisms of friction [17-19]. Atomic stick-slip often occurs when two clean surfaces, at least one of which is crystalline, are translated in relative motion [20]. Fundamental mechanisms of atomic-scale sliding have already been analyzed in many studies using the PT model [21, 22]. The PT model describes sliding as a process of building-up followed by an unstable release of energy in sufficiently compliant elastic elements of the system while traversing a periodic energy landscape (corresponding to the surface lattice sites) with sufficiently deep local energy minima. Upon slip at the maximum lateral force (the static friction force), physically unspecified dissipation causes the interface to stop slipping at the next lattice site (or sometimes multiple lattice sites, as reported by Medyanik *et al.* [23] and Roth *et al.* [24]) and the process repeats.

As discussed above, the PTT model appears to be widely applicable to atomic friction studies where scanning speed or temperature is varied, in contrast to the PT model. However, validating models quantitatively, understanding how energy is dissipated, and describing the atomic-level processes by which slip occurs dynamically at the interface are beyond the capabilities of the PTT model and are challenging because of

the inaccessibility of the buried interface in experiments. As observation of these processes may be the critical to the solution of thermally activated friction, a method must be derived to visualize the contact in greater detail. However, it is currently impossible experimentally to directly observe the contact with atomic resolution and record atomic stick-slip during sliding. Given that this is the likely pathway to the development physical models of friction and to understand the dissipation mechanisms, this level of detail can at present only be obtained by comparing atomic stick-slip experiments with MD simulations. These simulations provide a means of directly observing and interpreting atomic interactions within the interface [25, 26].

However, a critical discrepancy between AFM experiments and MD simulations is that the scanning speeds of AFM and MD, until the present work, differ by orders of magnitude. This issue results from: (a) the femtosecond time steps used in standard MD to capture atomic motion limit the time duration that can be simulated, constraining the simulations to high scanning speeds ($>10^{-1}$ m/s); and (b) the far slower scanning speeds ($<10^{-6}$ m/s) of AFM experiments which are typically constrained by instruments' intrinsic mechanical and data acquisition limits. This discrepancy limits the ability to reliably compare results from AFM and MD, and provides a primary scientific motivation for this experimental study: to improve the experimental apparatus of the AFM such that high scanning speed atomic stick-slip measurements can be recorded.

6.2: Speed Dependence of Friction

Two approaches exist in investigating thermally activated friction: varying the scanning speed and varying the temperature (or a combination of the two). In the first

part of this study, the friction force as a function scanning speed is investigated. Varying the scanning speed of AFM atomic stick-slip measurements has real engineering applications. In the development of atomic friction theories, most AFM measurements achieve a range of scanning speeds of 1 nm/s to 1 μm/s. This range of scanning speeds compares well with piezo motors and inchworms [7]. However, MEMS devices typically operate between a range of μm/s – mm/s [27] and the current generation of hard disk drives typically achieve a relative speed between the write/read head and the disk 50 m/s [28]. Additionally, real scanning speeds achieved in engineering mechanical systems, such as in automobile cylinders, typically operate at scanning speeds on the order of m/s. Therefore, the results of fundamental scientific models of friction derived from AFM experiments have limited applicability to the greater engineering community unless experiments can replicate conditions closer to these real mechanical systems. Second, varying the temperature is important for the examination of dry sliding under extreme environments, such as in aerospace or vehicle applications. It also opens a greater parameter space to examine the influence of thermal activation than can be achieved solely by varying the scanning speed. Further discussion on the temperature dependence of friction in Section 6.3. The following section presents the details regarding work performed in order to close the scanning speed gap between AFM experiments and simulations for the first time.

6.2.1: Experimental Details

6.2.1.1: Preparation of Gold Samples and Experimental Conditions

Polycrystalline gold samples were used in the speed dependence experiments. Following the deposition methodology pioneered by Nogues *et al*., [29], gold samples were prepared by thermal evaporation of bulk gold (purity 99.99%, Kurt Lesker Inc., Pittsburgh, PA, USA), onto freshly cleaved muscovite mica (SPI Supplies Inc.). The main evaporator chamber (Kurt Lesker PVD 75) was operated at a pressure of ~10^{-7} Torr. The nominal thickness of the gold layer is approximately 300 nm. A representative as-deposited gold sample is shown in Figure 6.1 (a). The reason that muscovite mica is chosen is that an atomically clean and flat substrate can be easily prepared by cleaving immediately before inserting into the deposition machine. After the deposition, the gold surface has many grains with an average grain size of ~100 nm, as shown in Figure 6.1 (b). The next step is to perform flame annealing shortly before inserting to the AFM chamber using a hydrogen torch to heat the sample such that it glowed for about 30 sec. As a result of hydrogen flame annealing, the gold surface formed atomically flat terraces several 10's or even 100's of nm wide (and running for many micrometers or more in length) separated by monatomic steps, as shown in Figure 6.1 (c). Next, the sample was loaded into the fast entry lock of the AFM system and subsequently pumped down to high vacuum. While pumping down, the fast entry lock was baked at 160 °C for 8 hours to reduce the adsorbed water vapor on the sample and sample holder (as well as on all surfaces of the load lock itself). Subsequently, the sample was inserted in the main AFM chamber (base pressure ~6×10^{-10} Torr), and then annealed *in vacuo* to ~450 °C for ~1

hour to desorb any remaining surface contaminants from the gold. Following this last annealing stage, the sample was left in the chamber for 3-5 hours to thermally equilibrate with the surrounding microscope.

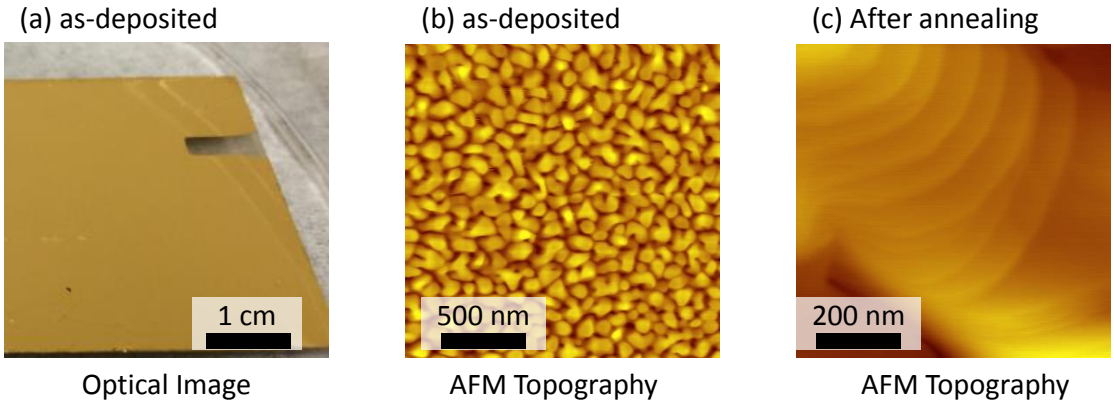

Figure 6.1: Gold samples prepared through thermal evaporation onto freshly-cleaved muscovite mica. The nominal thickness of the gold layer is 300 nm. (a) Optical camera image of the as-deposited sample; (b) AFM topography image, as-deposited; grains with an average size of ~100 nm are visible. (c) AFM topography, after annealing, showing many atomically flat terraces.

6.2.1.2: Experimental Protocol for Friction Measurements

All experiments were conducted in the RHK 750 AFM at room temperature (RT) and in an ultra-high vacuum (UHV) environment, where the base pressure was maintained at approximately 6×10^{-10} Torr. Single crystal silicon contact-mode cantilever probes with integrated tips (Mikromash CSC 38) were used throughout the experiments; the silicon surface has a native silicon oxide layer. The rectangular AFM cantilever's force constants were calibrated using the beam geometry method [30] by determining the thickness of the cantilever by measuring the first normal resonance and optically measuring the cantilever length and width. The optical sensitivity of the PSD was

assumed to be the same in both lateral and normal directions. Calibration of output volts from the PSD to nanometers was achieved by acquiring normal force versus *z*-displacement curves and determining the slope of the resulting data. The lateral force, or the twisting signal of the cantilever measured at every position, is differentiated from the friction force, which is the half the calculated average force of the difference in the lateral force in the forwards and reverse scanning directions (deliberately excluding the sticking portion of the friction loop). Note that this mean value is different than the maximum value due to the amplitude of the stick-slip fluctuations; a statistical average of the maximum value is truly representative of the lateral force at which slip occurs, but is subject to larger error than the mean value since one must identify the small number of points where slip occurs. In practice, we have found that using the mean value provides a robust comparison with MD simulations with a significantly reduced uncertainty [1, 3]. The error bars given in the normal and friction force represent the standard deviation in the calculated mean. Only areas of the sample containing large terraces of more than 100 nm^2 in lateral dimension were examined. All data was acquired at an applied load of 0±0.2 nN. The scan rate was varied randomly with ten cycles per scanning speed.

Before performing the friction experiment, TEM (JEOL 2100, JEOL Inc.) images of the tip apex were acquired first to determine the work of adhesion between the SiO_2 and the gold sample. The procedure is as follow. A new AFM tip was used to measure the pull-off force by averaging 25 pull-off measurements on the gold sample, subsequently TEM images of the tip apex were acquired to calculate the tip radius *R*. Using the DMT model (Equation 2.8), the work of adhesion W_{12} was determined to be 0.05±0.03 J/m^2.

In order to justify the use of the DMT model, the Tabor's parameter, μ_T, was calculated from this number for the work of adhesion. μ_T is a transition parameter that is used to determine the contact regime and if defined according to Equation 6.1 [31]. It ranges from <<1 for DMT regime [32] to >5 for JKR regime [33]

$$\mu_T = \left(\frac{16RW_{12}{}^2}{9E_c^2 z_0^3}\right)^{1/3} \tag{6.1}$$

where R is the tip radius, W_{12} the work of adhesion, E_c the composite elastic modulus, as defined in Section 2.1.2, and finally z_0 is the equilibrium separation distance [32]. The z_0 is assumed to have a lower-bound value 0.1 nm [34].The following elastic constants were used: E = 78 GPa and ν = 0.44 for gold [35], and E = 55.6 GPa and ν = 0.16 for SiO_2 [36], resulting in a combined modulus of E_c ~ 36 GPa. For the tips used for friction experiments, an upper-bound value of μ_T was found to be 0.29 from Equation 6.1, much lower than 1, thus indicating that the DMT model is indeed suitable. (Due to the similarity between the tips, others tips used in this study can also be assumed to follow the DMT model.)

For the radii of the tips used for experiments, TEM images of the tip apex were acquired before and after the experiments to check for changes to the tip during the experiment. Since it can be difficult to determine the tip radius even from *post-mortem* TEM imaging of the tip apex, pull-off force measurements were used to estimate the tip radius using the DMT model [32].

6.2.1.3: Design of a High-Speed Piezo Scanner

This section outlines the improvements made to the AFM apparatus to obtain significantly higher experimental scanning speeds than those achieved in the AFM study published in Ref. [3], which was ~1 μm/s. Design parameters for this improved experimental apparatus can be estimated as follows. Given the lattice periodicity of gold (~0.288 nm) and the desired scanning speed, the average rate the tip would traverse the lattice is approximately 347 kHz. To resolve atomic stick-slip motion, one would need approximately 10 data points per stick-slip event. Thus, it is necessary to measure at a rate of approximately 3.5 MHz or higher to observe atomic stick-slip while coinciding with the scanning speeds attainable in MD simulations.

To record the lateral force signal at the desired speed, high speed electronic acquisition hardware was required to measure stick-slip behavior at MHz sampling rates. The acquisition rate is normally determined by the bandwidth of the data module of the instrument (SPM 100/PLLPro, RHK Technologies Inc.), which is around 125 kHz. Although this bandwidth is sufficient for obtaining clear atomic stick-slip friction at scan speeds in reasonable scan amplitudes (~10 nm), the speed is limited to the range of ~1 nm/s to ~1 μm/s. At higher speeds (10 - 100 μm/s), the limited bandwidth of the controller is not sufficient to observe the atomic lattice. A second challenge is the inherent resonance frequency of the AFM scanning head: in our case, it is in the range of ~1.5 kHz [37]. This can cause significant ringing of the scan piezo at the turning points of scans, as well as a variation of the scan speed during a single friction loop, both occurring when the speed is sufficiently high. Therefore, at higher speeds, these problems can distort images and cause problems in determining the exact scanning speed. To

summarize, both the low bandwidth of the acquisition hardware and a low resonance frequency of the scanner limit the speeds attainable where clear atomic stick-slip friction can be measured. We will discuss solutions to each of these problems in the following paragraphs.

To measure atomic stick-slip at high scanning speeds, an external National Instruments (NI) data acquisition device (USB-BNC 6125, 16 bits A/D conversion, National Instruments Inc., Austin, TX, USA) having a sampling frequency of 1.25 MHz will be used. The USB-BNC 6125 is shown in Figure 6.2. It provides enough bandwidth to achieve scanning speeds up to ~40 μm/s (as a reference, conventional MD simulations are typically performed at 0.1 m/s scanning speeds or higher). This maximum scanning speed was determined by assuming ten points per sticking phase when resolving stick-slip was desired. Given the sampling rate (1.25 MHz) of the acquisition device and the size of the atomic lattice (0.288 nm [3]), the maximum scanning speed can be determined. Using the combination of the RHK controller with the NI acquisition device, the lateral signal was recorded sufficiently fast to see stick-slip with the NI data acquisition device while recording the normal force and other channels at a slower sampling rate with the controller. The average friction forces to be reported *vs.* scanning speed were determined using the lateral forces recorded by the RHK controller, whereas lateral forces showing stick-slip resolution were always acquired from the NI device.

Figure 6.2: NI USB-BNS 6125, with a data sampling rate of 1.25 MHz. Only one analogue input channel is connected to the lateral signal channel output from the AFM controller.

The second challenge is the low resonance frequency of the scan head. To overcome this, a new home-built sample holder was designed and constructed. This sample holder lowered the mass of the sample that must be moved when measuring atomic stick-slip by only translating the sample itself, rather than the entire AFM scan head. To achieve this, the sample was mounted atop a small, high-frequency shear piezo (EBL#2, EBL Inc., East Hartford, CT, USA). The intrinsic resonance frequency of the shear piezo was ~1.5 MHz, as calculated from the manufacturer's specifications. This frequency was expected to be affected slightly by the additional mass of the sample after mounting onto it, but was estimated to be still $\gtrsim$ 1 MHz, and therefore was still much higher than the above mentioned resonance frequency of the AFM scan head since the total mass is still far less, and the structural stiffness much higher, than that of the AFM head.

Figure 6.3 (a) and (b) show the completed sample holder. Figure 6.3 (c) shows a schematic cross-sectional view of the sample holder when glued (H61, Epoxy

Technology Inc., Billerica, MA, USA) onto the shear piezo. Additionally, the sample holder was equipped with a tungsten filament at the bottom of the holder, allowing for *in situ* annealing to a temperature up to ~600° C. Much lower temperatures were typically used, considering the maximum allowed temperature of the piezo elements and the epoxy that was applied in the holder. A K-type thermocouple was mounted near the sample surface to monitor the temperature while annealing. Figure 6.3 (d) and (e) show the new sample holder inside the AFM chamber. Since the sample is mounted atop a steel wedge and the AFM scanner rested on the flat top assembly of the sample holder, the tip approached the sample surface by walking the entire scanner the left side.

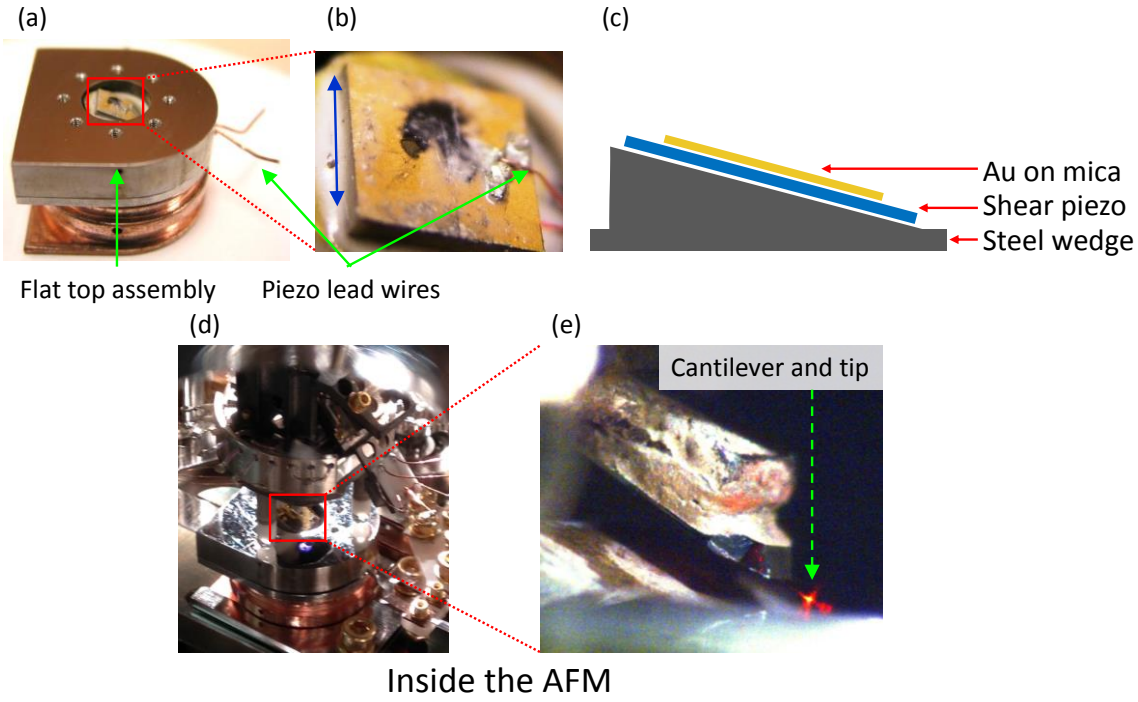

Figure 6.3: (a): Photographs of the newly designed sample holder. The green arrow indicates the flat top assembly of the new sample holder. (b) A close-up photograph shows the shear piezo mounted on a ramp. The blue arrow indicates the direction of shearing. The green arrows indicate the lead wires supplying voltage to the shear piezo. (c) Schematic cross-sectional view of the sample when mounted onto the shear piezo and a steel wedge. The steel wedge is has an angle of 5° to compensate the intrinsic tilt angle of the AFM yet allowing the tip to approach. (d) The new sample holder mounted into the AFM chamber. (e) AFM cantilever and a gold sample. Due to the steel wedge, the tip can be brought into contact by walking the AFM scanner laterally to the left.

After the entire setup was completed and tested, a function generator (Agilent 33250A, Agilent Inc., Santa Clara, CA, USA) combined with a voltage amplifier (NF HSA 4101, NF Corporation Inc., Yokohama, Japan) were used to supply a triangular signal of 100 peak-to-peak volt, allowing for sample translation through the shear piezo

at various frequencies. In all experiments, the normal applied load was zero and the scanning speed was varied by altering the frequency of the shear piezo, which could range from 30 mHz to 10 kHz, far below the piezo assembly's resonance frequency. The scan size of the shear piezo was determined by calibrating the shear piezo by averaging the number of stick-slip events and using the nearest-neighbor lattice spacing of the Au(111) surface [3].

6.2.2: MD Simulations Protocol

Complementary simulations, performed through collaboration by the Martini group at the University of California Merced, consisted of the apex of an amorphous SiO_2 AFM tip scanning over a Au(111) surface. The gold substrate had dimensions of $10\times10\times5$ nm^3 (length × width × thickness). The atoms in the bottom 1 nm of the substrate were fixed and the positions of the rest of the atoms in the substrate were unconstrained. The AFM tip was modeled as a truncated cone with a top surface diameter of 3 nm, bottom surface diameter of 2 nm, and 3 nm height. Amorphous SiO_2 was obtained by quenching a block of crystalline SiO_2 and then cutting the desired tip shape from the block. MD simulation model is shown in Figure 6.4. The topmost atoms in the tip were treated as a rigid body that was subject to a 0 nN external normal load and connected by a harmonic spring to a support that moves laterally at a constant speed. A Langevin thermostat was applied to the free atoms maintained a temperature of 300 K.

Parallel replica dynamics (PRD) was used to accelerate the simulations [38]. The number of parallel replicas was determined by the target scanning speed. For the slowest scanning speeds (v = 25 μm/s), there were 200 replicas running in parallel on 200

processors. In this case, the simulation job took 516 hours and mean time between slip events was approximately 7000 ps while the time for an uncorrelated slip event was less than 50 ps.

In all simulations (MD and PRD), the inter-atomic interactions within the tip and substrate were described via the Tersoff [39] and Embedded-Atom Method (EAM) [40] potentials, respectively, and the long range interactions between tip and substrate were modeled using the Lennard-Jones (LJ) potential. The LJ parameters are Si-Au: ε=0.0047 eV and σ=3.38 Å, O-Au: ε=0.0033 eV and σ=3.04 Å obtained using the standard mixing rules for dissimilar elements [16, 17]. The validity of these parameters was confirmed by comparing the work of adhesion predicted in the simulation to that measured experimentally. The work of adhesion (0.042 J/m^2) calculated from the simulation was consistent with the value of 0.05±0.03 J/m^2 measured in experiment. All simulations were performed using LAMMPS simulation software [41].

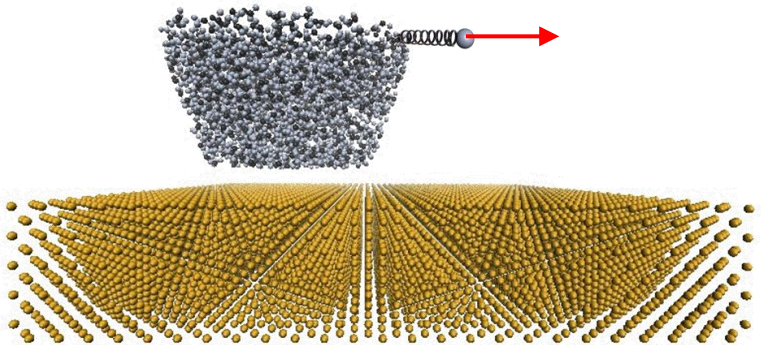

Figure 6.4: MD model of the SiO_2 tip scanning across the Au(111) substrate. Gold-colored spheres represent gold atoms. Black-grey particles represent SiO_2. The red arrows indicate the direction of the normal load.

6.2.3: Experimental Results

AFM friction experiments are performed on gold samples containing atomic steps. The samples are prepared according to the methodology described in Section 6.2.1.2. Figure 6.5 shows a high-purity Au(111) sample after annealing inside the AFM chamber. The integrity and cleanliness are demonstrated by the presence of herringbone surface reconstruction and stick-slip friction. The herringbone surface reconstruction on gold has previously been reported by Harten *et al*. [42] and by Narasimhan *et al*. [43], among others. Due to the reconstruction, the Au(111) surface exhibits a large scale periodic transition between face-centered cubic (fcc) and hexagonal close packed (hcp) hollow site locations. According to those previous reports, the reconstruction is known to originate from two competing energetic aspects: (a) the surface atoms have a preferential bond length shorter than that in bulk due to their lower coordination number; and (b) the surface atoms are confined by the atoms below, where they prefer to sit on local potential minima (hollow sites).

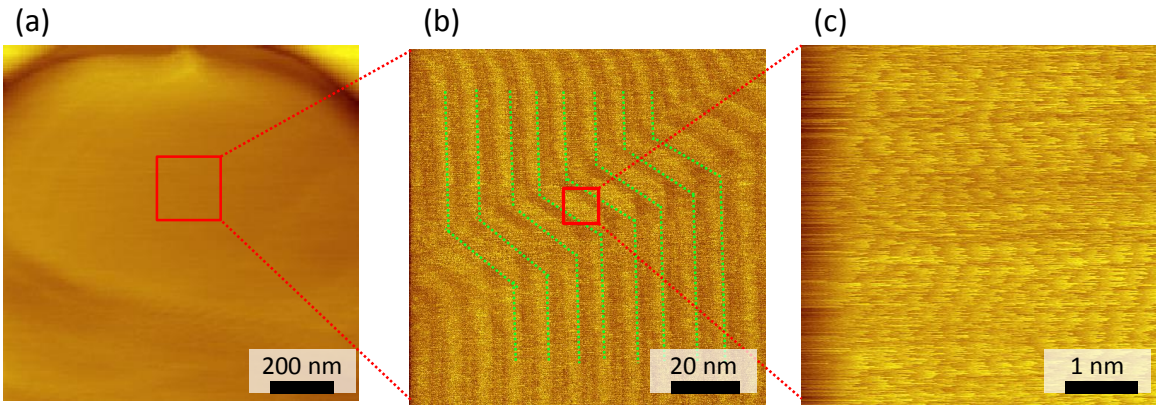

Figure 6.5: (a) Topographic image shows large terraces (> 100 nm^2) are observed on the Au(111) surface. The quality of the surface preparation was verified by the presence of herringbone surface reconstruction (shown in (b)) and the stick-slip pattern in the friction signal (shown in (c)).

Li *et al*. has reported that the herringbone reconstruction has only a minor effect on the net frictional dissipation [44]. In this study, for simplicity, only fcc areas were selected for friction experiments. Two different silicon contact-mode probes (Mikromash CSC 38, Mikromasch Inc.) were used (called Tips 1 and 2 subsequently), as shown in Figure 6.6. From the pull-off force and the value for work of adhesion of 0.05±0.03 J/m^2 obtained earlier, a value for the tip radius of 30±20 nm and 9±6 nm for Tips 1 and 2 were obtained, respectively, giving a contact radius of 2±1 nm and 0.8±0.5 nm for Tips 1 and 2, respectively. As discussed in Section 3.1.2 and evident by Equation 3.2, the total lateral stiffness, k_{tot} (which includes the contributions of the lateral stiffness of the contact, cantilever, and the tip) is an important test parameter for matching experiments with simulations. It can be directly determined since it corresponds to the slope of the friction trace during the "stick" phase. For Tips 1 and 2, k_{tot} was determined to be 5.4±0.7 N/m

and 5.5±0.9 N/m, respectively. The mean value of the two was subsequently used to match the total lateral stiffness obtained in the MD.

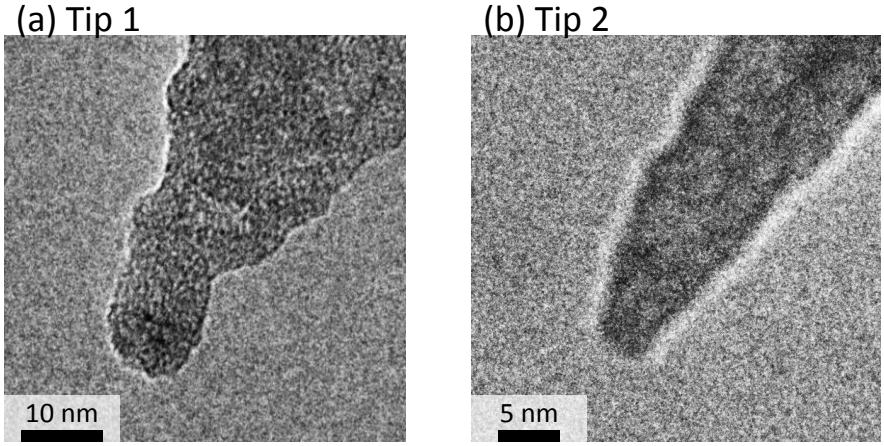

Figure 6.6: *Pre-mortem* TEM images of Tips 1 and 2 used for data acquisition. The initial tip radius for Tip 1 is 4.9 nm and 3.6 nm for Tip 2.

A representative lateral force data set is shown at a shear frequency of 300 Hz, acquired from the NI data acquisition device that is controlled by a custom-written LabVIEW script[4]. At this shear frequency, ten sliding cycles occur in ~33.3 ms. Data were collected for 1 sec at the maximum bandwidth of the acquisition device, resulting in 1.25×10^6 data points. A MATLAB script[5] was then used to analyze this data string. The entire data string is plotted *vs.* sliding time and shown in Figure 6.7 along with the specific steps within the algorithm of the script. Next, each individual lateral force trace

[4] LabVIEW programming was developed in collaboration with Mr. Travis Hunt (an undergraduate student the Department of Physics and Astronomy, University of Pennsylvania), and Mr. Qizhan Tam (an undergraduate student the Department of Mechanical Engineering and Applied Mechanics, University of Pennsylvania).

[5] MATLAB programming was developed in collaboration with Mr. James Hilbert (PhD Candidate, Department of Mechanical Engineering and Applied Mechanics, University of Pennsylvania) and Mr. Qizhan Tam (an undergraduate student the Department of Mechanical Engineering and Applied Mechanics, University of Pennsylvania).

in the forward and reverse direction were identified, and plotted *vs*. time. Finally, since the shear piezo was pre-calibrated, the lateral signal can be plotted *vs*. sliding distance, from which average friction force is calculated. Figure 6.7 (d) shows that the friction loop is tilted. This was attributed to the fact that the shear piezo also deformed in the out-of-plane direction. The change in normal force has two effects. First, it changes the friction force. This would cause a change in the width of the friction loop, but this is not observed. According to the deviation in normal force signals, the out-of-plane deformation is ~10% of the shear deformation, resulting in a variation of <10% in the total applied load (when shearing at low rates, this deformation is compensated by the AFM feedback control, as evident from the small error bars in the normal force). We conclude this effect is negligible. Second, a small portion of the normal force signal may be coupled in to the lateral force signal (this can be due to rotational misalignment of the PSD or other misalignment in the AFM [45]). This would cause the lateral force to have an offset that varies with the lateral position, leading to a tilting of the friction loop. This is exactly what we observe. Thus, we conclude that the effect is due to normal-lateral instrumental coupling. This small variation in the sample *z*-position during scanning had a negligible effect on the experiment.

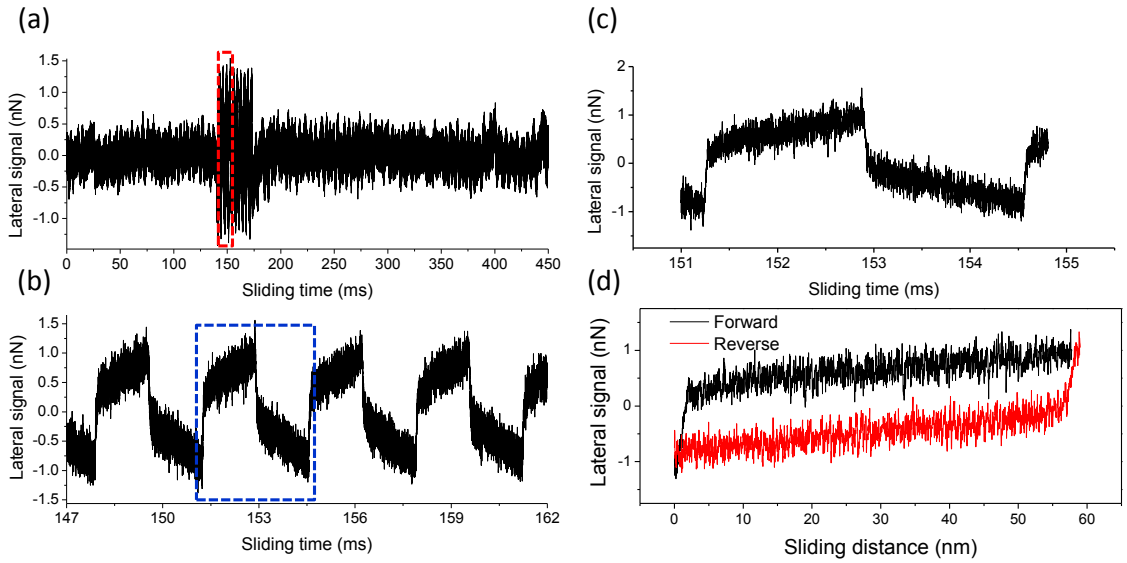

Figure 6.7: Step-by-step schematic illustration of the analysis method using custom-written MATLAB script. The algorithm is used to extract individual friction loops in the string of data collected at each frequency. (a) A representative friction *vs.* time data acquired at 300 Hz with Tip 1. At sliding time ~150 ms the shear piezo was actuated for 10 cycles and stopped immediately, at sliding time ~175 ms; given the frequency, 10 cycles lasted for ~33.3 ms. (b) A zoomed-in plot of the individual sliding cycles at the red dashed box in (a). MATLAB script is then used to identify forward and reverse scan directions, and plotted *vs*. sliding distance in (d). From (d), fiction force is calculated.

Figure 6.8 shows the experimentally measured friction force as a function of scanning speed for the two different tips. Single atomic stick-slip was resolved up to speeds of >10 μm/s, after which an insufficient number of data points per stick-slip event could be recorded. The typical logarithmic increase in friction force is observed starting from the minimum scanning speed, approximately 1 nm/s, until a plateau was observed at a speed between 1-10 μm/s in both cases. To interpret these results, the data were fitted to the PTT model [4, 8] using the following equation:

$$\frac{1}{\beta k_B T}(F_c - F_L)^{3/2} = \ln\frac{v_0}{v} - \frac{1}{2}\ln\left(1 - \frac{F_L}{F_c}\right) \quad (6.2)$$

where F_L is the mean friction to be measured and v the speed that is varied during the experiment. T is the temperature, k_B is Boltzmann's constant, F_c the mean friction force at zero Kelvin (athermal friction), β is a parameter related to the shape of the lateral potential profile and describes the rate of increase of friction with speeds at low speeds, and v_0 is a characteristic speed given by

$$v_0 = \frac{2f_0\beta k_B T}{3k_{tot}\sqrt{F_c}}, \quad (6.3)$$

where f_0 is the characteristic attempt frequency, and k_{tot} the total lateral stiffness [2, 4]. For a sinusoidal potential with periodicity a and barrier height E_0,

$$F_c = \pi E_0/a \quad (6.4)$$

and

$$\beta = 3\pi\sqrt{F_c}/\left(2\sqrt{2}a\right). \quad (6.5)$$

Combining Equations 6.3 and 6.5 gives a new expression for and v_0:

$$v_0 = \frac{\pi f_0 k_B T}{\sqrt{2}ak_{tot}} \approx af_0\frac{k_B T}{a^2 k_{tot}}, \quad (6.6)$$

where the pre-factor (af_0) can be considered as the undamped slip speed scaled by the ratio between the thermal energy ($k_B T$) and energy associated with elastically deforming by 1 lattice site ($a^2 k_{tot}$). Therefore, higher attempt frequency, higher temperature, and a more compliant system all contribute to a greater v_0.

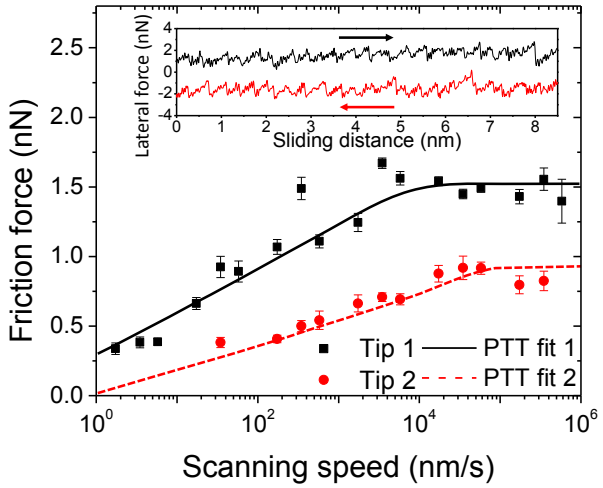

Figure 6.8: Friction force *vs*. scanning speed for Tip 1 (black squares) and 2 (red circles). The solid line (Tip 1) and dashed line (Tip 2) are fits of the PTT model to the data, which yield, for Tip 1: F_c= 1.5±0.2 nN, β = (4.8 ± 2.0)×10^5 $N^{3/2}$/J, and f_0 = 108±42 kHz; and for Tip 2: F_c = 0.9±0.2 nN, β = (2.5±0.3)×10^5 $N^{3/2}$/J, and f_0 = 700±200 kHz. The normal applied force is 0.0±0.2 nN in both data sets. Error bars represent the standard deviation in the calculated mean friction force. Top-left inset shows a friction loop acquired with Tip 1 at ~5.8 μm/s; an atomic stick-slip pattern can be clearly resolved corresponding to scanning along the [110] direction.

The three fitting parameters, β, f_0, and F_c can now aid in distinguishing variations between the two measurements. Given the plateau in the friction measurements at high scanning speeds, the F_c had to be determined first, as an average of the data points in the plateau, and used in the PTT fit at lower scanning speeds, where β and f_0 were extracted. In both experiments, the values of β are similar to within a factor of 2, which is to be expected as β describes the shape of the potential energy corrugation of the surface and should similar in both cases since the same materials are involved and both tips are roughly the same size; the only difference would be in the atomic structure of the

amorphous silica-terminated tip and possibly in the nanoscale roughness of each tip. Thus, it is reasonable for β to be comparable for both cases. Similarly, F_c does not vary significantly between the two tips, which is also to be expected as F_c describes the magnitude of the friction force when it is not influenced by thermal energy, which should be the same for identical materials and tip geometries; different contact areas due to different atomic-scale structural features of the tip could cause F_c to vary somewhat. Finally, the discrepancy between the values of f_0 of the two tips is relatively large. However, both values are within the same range as other AFM experiments reported before [2-4], and given the difference in the effective mass between the two tip apices (as the estimated tip radii are different), the difference in the coupling from the instrument noise to the tip, and the large experimental uncertainty, this difference in attempt frequency is not surprising.

6.2.4: MD Simulations Results

The simulation-predicted mean friction force is shown in Figure 6.9. Significantly, the slowest scanning speed obtained from PRD simulations (25 μm/s) is smaller than the fastest speed of experiments (~580 μm/s), and is also approximately three orders of magnitude slower than previously achieved scanning speeds in MD. Overlapping datapoints at 0.1, 0.2, and 0.5 m/s from MD and PRD validate the PRD simluations. Achieving this overlap is a primary point of novelty for the work in this thesis as well as the MD simluations.

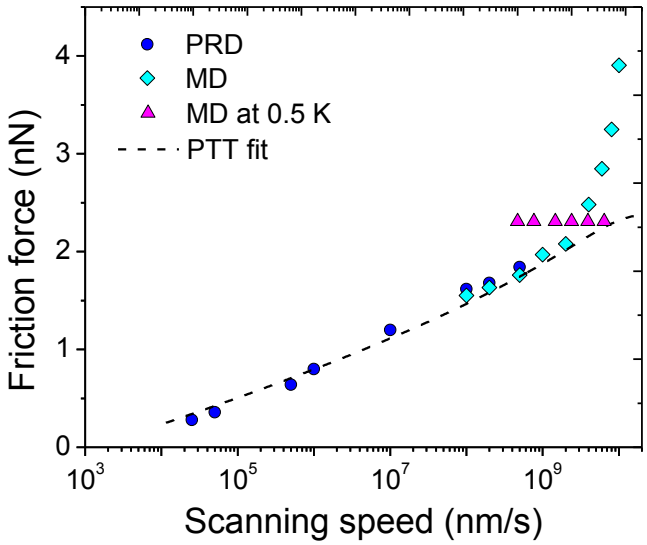

Figure 6.9: Friction force as a function of scanning speed from MD at 300 K (cyan diamonds) and 0.5 K (purple triangles), and PRD (blue circles) at 300 K. Dashed lines indicate fits of the PRD data to the PTT model using a value of F_c of 2.56±0.02 nN from the simulations run at 0.5 K, yielding β=(2.9±0.2)×105 $N^{3/2}$/J and f_0=120±30 GHz.

MD simulations were run at 0.5 K to mimic sliding friction without thermal activation; the resulting constant friction force plateau at 2.56±0.02 nN was then used as the value of F_c in the PTT model fit. Above scanning speeds of 4 m/s, friction increased rapidly with speed, deviating from the plateau predicted by the PTT model. The unphysically high friction at high speeds is consistent with previous observations, although no physical explantation was provided [3]. The present simluations reveal that it is associated with surface wear, quantified empirically by measuring the root mean square surface roughness, which was observed to increase dramatically at these speeds due to irreversible displacements of atoms. The high speed data was excluded from subsequent analyses, enabling isolation of friction from wear and subsequent fits of the

data to the wearless PTT model. Fitting the 300 K simulation data up to 1 m/s then yields $\beta = (2.9\pm0.2)\times10^5$ $N^{3/2}/J$, and $f_0 = 120\pm30$ GHz for the simluations.

6.2.5: Discussion

For the combined AFM and MD study, we observed single stick-slip events across 10 orders of magnitude of speed. In the AFM data, for the two tips used in experiments, β agreed to within a factor of 2, being $(4.8 \pm 2.0)\times10^5$ $N^{3/2}/J$ and $(2.5\pm0.3)\times10^5$ $N^{3/2}/J$ for Tips 1 and 2 respectively. At mentioned previously, the discrepancy between these two values is reasonable. Although the tip and sample materials are the same for both measurements, the sliding direction for both tips was the [110] direction, the calculated contact radii for the two tips differ by a ratio of approximately 1.5, leading to different values of β. Furthermore, given that it is not possible to observe the tip apex in contact with the surface during sliding in the experiments, the atomic structure at the end of each tip could differ, contributing the variation in β we observed. This suggests that either the interfacial potential is not strongly dependent on the details of the amorphous tip's surface atomic structure, or the tip structures are relatively similar. Similarly, the F_c values agree within a factor of 1.7, being 1.5±0.2 nN and 0.9±0.2 nN for Tips 1 and 2 respectively. The larger tip produced the larger value of F_c. This difference is consistent with theoretical predictions that F_c increases with the contact area, resulting from the fact that more atoms at the interface contribute to friction [26, 46, 47]. The greatest discrepancy between fits of the PTT to the friction data acquired from the two tips is the 6.5 times difference between the two f_0 values, being 108±42 kHz and 700±200 kHz for Tips 1 and 2 respectively. While they

are both in the range of previously-reported AFM experiments [2-4], the difference suggests that either the effective mass of the two tip apices are rather different (potentially this arises from their different size and shape) or the coupling of instrument noise to the tip in each experiment was different [48].

To better compare experiment and simulation, the AFM data from Figure 6.8 and the MD/PRD data from Figure 6.9 are plotted together in Figure 6.10 allowing further analysis. Figure 6.10 clearly shows that the speed gap between simulations and experiment has been closed. However, there is a significant difference between the measured and predicted friction force, despite matching the conditions as closely as possible. We can understand this difference by comparing the three fitting parameters, β, F_c, and f_0, extracted from the fits of the PTT model to the experimental and simulation data. The lateral potential shape (β) can be directly fit to both experiment and simulation data; these values are consistent (2.9×10^5 $N^{3/2}/J$ from simulation, and 4.8×10^5 $N^{3/2}/J$ and 2.5×10^5 $N^{3/2}/J$ from experiments). This indicates that the shape characteristics of the energetic landscape for the experiments and simulation are comparable. The mean athermal friction force (F_c) of 2.56 nN, fit to the simulations run at 0.5 K, is somewhat larger than the two experimental values (0.85±0.18 and 1.5±0.2 nN), but it is of the same order of magnitude. The attempt frequency (f_0) from the simulation of 120±30 GHz is several orders of magnitude larger than those from the experiments (108±42 kHz and 700±200 kHz). The remainder of this section examines the root causes of the differences in F_c and f_0, which may explain the difference in the predicted and measured friction.

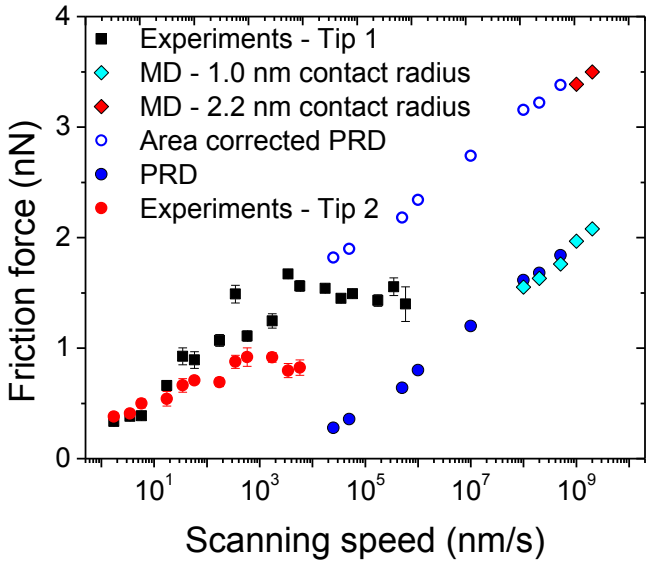

Figure 6.10: MD (cyan and red solid diamonds), PRD (blue solid circles), and experimental results from Tip 1 (black squares) and Tip 2 (red solid circles) plotted together. MD predictions are reported for 1.0 nm (cyan diamonds) and 2.2 nm (red diamonds) contact radii, r_c, where the latter is consistent with an extrapolation of the low-speed friction trend observed for Tip 1. The relationship between F_c and contact size is also used to extrapolate the PRD data to a 2.2 nm contact radius (blue hollow circles).

The discrepancy in F_c may have three origins: differences in tip shape, scanning direction, and contact area. First, a truncated cone-shaped model tip was used for the PRD simulations; this differs from the approximately hemispherical experimental tip shapes indicated by TEM images (Figure 6.6). Additional MD tests were performed to investigate the influence of tip geometry by simulating a hemispherical tip with the same approximate contact radius as that of the truncated cone. The change to a hemispherical model tip increased friction only by ~6% (data not shown), which is within the

uncertainty of the contact mechanics calculations, indicating that geometry cannot explain the experiment-simulation difference in F_c.

Second, the scanning direction was [110] in the experiments and [100] in the simulations. However, MD simulations run over a range of scanning directions produced only a ~4% change in mean friction force (data not shown). Therefore, scanning direction also cannot explain the discrepancy.

Finally, the effect of contact area is considered. Recall that the simulation contact area was designed to match a value estimated from experiments, where that estimate was based on a continuum contact mechanics model, a limitation imposed by being unable to directly measure contact area experimentally [32]. To test the sensitivity of F_c to the contact area, simulations of truncated cone-shaped tips with different circular contact radii were conducted. Friction increased linearly with contact area (data not shown), consistent with previous simulation [26] and experimental results [46, 47]. Based on the linear relationship between friction and contact area, increasing the model simulation contact radius from 1.0 nm to 2.2 nm would lead to MD results that, when extrapolated to low speeds (below ~10^4 nm/s), agree well with the low-speed experimental results (Figure 6.10: MD simulation data, red diamonds; extrapolated PRD data, hollow blue circles). This contact radius (2.2 nm) is consistent with the experimental estimation, and is reasonable given the limitations of using a continuum model to describe nanoscale contact [49, 50] and the significant uncertainty associated with determining the tip radius. This suggests that the contact area may contribute to the observed difference in friction between experiment and simulation. However, such a shift will not resolve the large disagreement in the onset speed of the plateau.

The experiment-simulation discrepancy can only be fully resolved by addressing the difference in attempt frequency, f_0. Mass (inertia) may be one cause of this difference, as discussed previously [3]. However, unlike the previous study, here no extrapolation of the data to fit the PTT model was necessary. Furthermore, the possibility of effects due to surface contamination can be excluded since the experiments were performed in UHV. We therefore can compare the results with confidence. In analyzing the tip masses, the tip apex in MD/PRD simulation is only comprised of a few thousand atoms, significantly smaller than the AFM tip or the cantilever, both of which exhibit thermal vibrations that can produce slip attempts. For a harmonic system, the attempt frequency will be related to the structure's effective mass, *m*, by

$$f_0 \approx \frac{1}{2\pi}\sqrt{\frac{k}{m}}, \tag{6.7}$$

where *k* is the spring stiffness. This expression, with the fit values of f_0 from experiment and simulation and the known simulation tip mass, predicts an effective experimental tip mass of m_{exp}~10^{-11} kg, corresponding to a volume of ~4×10^{-15} m^3 (assuming a density of 2.6 g/cm^3 [51]). While it is not exactly known how much of the tip actually contributes to thermally activated friction, the calculated volume is consistent with that of a real AFM tip, estimated to be ~7×10^{-16} m^3 based on the TEM tip images and the use of a method of disks from the tip profile [52]. This range of masses cannot be directly tested using MD simulations given the size-scale limitations of the MD method due to computational constraints. However, simulations of tips scanning at 1 m/s with artificially increased atomic masses showed that friction increased with mass (data not shown), consistent with our numerical solutions of the PTT model (higher mass reduces f_0; fewer slip attempts per

unit time lead to higher mean friction, similar to the effect of scanning faster). Thus, the small tip mass in the MD provides one explanation for the difference between simulation and experiment. In other words, a larger tip mass in the simulations would shift v_0 and the onset of the plateau to lower values.

Within the range of contact areas, tip masses, and scanning speeds explored in the simulations, the experimentally observed friction plateau is not reproduced. Physically, the plateau represents attaining a high enough scanning speed that available vibrations of the atoms at the end of the tip apex no longer have enough time assist in overcoming the local interfacial potential energy barriers [53]. In the PTT model, only those thermal vibrations of the tip apex are considered. However, other thermal noise sources, such as thermally induced vibrations of the cantilever, or athermal instrument noise, such as mechanical vibrations of the AFM apparatus and electronic 60 Hz noise, are not included despite the fact that they too can lower the activation barrier to slip by adding energy into the contact [48, 53]. Both athermal and thermal noise sources are inherent in every experiment, but are not captured in simulations. By applying the master equation method [54], the influence of both athermal and thermal noise sources can be captured simultaneously via numerical modeling. In this approach, both noise sources are specified in the model, with the magnitude of the athermal noise vibration to be modeled determined by calibrating its amplitude in the experiment with respect to the amplitude of the cantilever's thermal noise (as determined in a power spectrum of the cantilever signal). This analysis indicates that two transition points can occur: a plateau-like reduction in slope at low speed determined by low frequency instrument noise, and a plateau at high speed due to higher frequency thermal noise [48], as shown in Figure

6.11. The master equation method was applied (details in Ref. [1]) assuming thermally or athermally excited vibration of the cantilever at 200 kHz and an amplitude of 0.20 nm. This amplitude corresponds to an effective temperature of 1800 K based on the equipartition theorem [55], thus, the noise observed in the experiment is likely a combination of the thermal noise from the AFM cantilever oscillating at its first lateral resonance and athermal noise associated with the mechanical vibrations of the AFM apparatus. This modeling is the only current mechanism by which the low-speed friction plateau observed in experiments and the high-speed friction plateau observed in simulations can be linked.

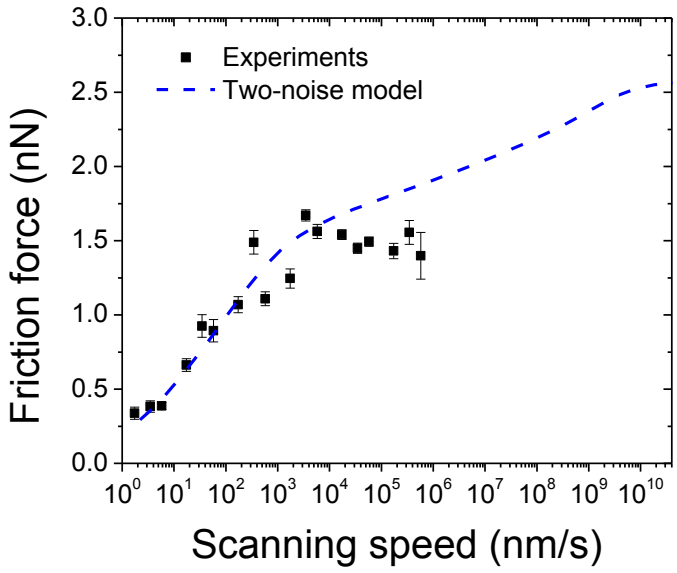

Figure 6.11: Master equation method (two-noise model) fit to experimental data. One can observe that due to the instrument noise, it is possible to reproduce two transitions in friction *vs.* speed data.

In Figure 6.11, there are two transition points. One transition point occurs at approximately $v = 10^4$ nm/s (F = 1.5 nN), which results from the instrument noise. The second transition point occurs at $v = 8\times10^9$ nm/s (F = 2.56 nN) originating from thermal noise. In the low speed regime before the first transition point, the two-noise model fits the experimental data well. After the first transition point, the fitting curve enters a lower slope regime, which is not the same as the plateau in the experiment. The difference between the fit and the experimental data points can be rationalized by the following two mechanisms. First, the instrument noise was assumed to be independent of scanning speed. Given the complexity in the experimental setup, the additional shear piezo used to scan the sample at the high speeds, and the sensitive electronics that are used in measuring atomic stick-slip at high scanning speeds, it is possible that a speed dependent noise source is captured in the experimental data. More specifically, if the instrument noise amplitude varies with scanning speed, it is possible that the friction force can be further suppressed at the first plateau regime. Second, the parameters for thermal noise, specifically the attempt frequency, are adopted from the simulations. It was previously demonstrated that MD simulation significantly underestimates the effective mass of tip apex, thus overestimating the attempt frequency. In combination with a larger effective mass of tip apex, the two slope fit, resulting from instrumental noise, would be able to better fit the experiment measurements, especially at the higher speed regime. More discussion on this can be found in [1] and [48, 53].

6.3: Temperature Dependence of Friction

Next, friction properties as a function of temperature were explored. The goal of this study was to understand the atomistic mechanisms that govern the temperature dependence of nanoscale friction. Greater understanding of the temperature dependence of friction will directly benefit a wide range of engineering applications as well as provide fundamental insight. More specifically, there are a variety of devices with tribological interfaces that need to operate at elevated temperature environments, *e.g.*, sensors in combustion systems [56] or in power plants [57], as well as next-generation hard drives which incorporate the heat-assisted magnetic recording (HAMR) technology [58]. In HAMR technology, there are high-temperature components for which tribological issues are major challenges [58]. Additionally, the temperature dependence of friction is relevant in aerospace applications, including satellites and spacecraft, which are constantly exposed to harsh conditions such as temperatures ranging from below 4 Kelvin to several hundred degrees Kelvin.

Several recent studies have reported a strong reduction of friction with increasing temperature, an effect termed thermolubricity [10, 13]. According to the PTT model, low friction at elevated temperatures is explained by the fact that atoms at the interface benefit from thermal excitations which provide energy to help overcome local energy barrier and enable tip atoms to slip. Experimental studies at the nanoscale have observed friction being reduced at elevated temperatures [5, 11, 12, 14]. Specifically, Zhao *et al.* studied friction between silicon nitride (Si_3N_4) tips and HOPG surfaces in UHV for temperatures between 140-750 K, and found that friction decreased with temperature in a

nearly exponential fashion [11]. Schirmeisen *et al.* studied Si tips sliding on a silicon surface (with native oxide) and observed a similar trend above 100 K. However, from 50 to 100 K, friction increased with temperature, thus producing a maximum friction force near 100 K [5]. Barel *et al.* used a simple multi-bond model of the interface and explained that this peak at 100 K was due to the competition between thermally activated interfacial bond rupture and bond formation processes, which were assumed to have different activation energies [15]. However, the nature of these bonds is not specified, and thus it is not possible to predict the temperature dependence of friction for other materials based on this model alone.

In this part of the study, AFM experiments and MD simulations are closely matched to examine the temperature dependence of atomic-scale friction. Specifically, the sample temperature is controlled across a wide range of temperatures during scanning and MD simulations over the same range are conducted. Experimental parameters, namely environment, sample material, contact area, normal and lateral stiffnesses, and load, were also matched as closely as possible in the MD simulations. MD provides access to the atomistic details of the contact interface, and provides valuable insight into topics such as interfacial bond formation and rupture as considered in the model of Barel *et al.*, for example. Since this is an ongoing project, this Section only presents preliminary experimental and simulation data.

6.3.1: Experimental Details

A bulk MoS_2 sample (SPI Supplies Inc.) was cleaved *ex situ* in laboratory air (RH ~30-60%) to expose the (0001) surface, and then immediately introduced into the fast

entry lock of the RHK 750 AFM system, which was then evacuated. The fast entry lock was then baked at 140 °C for 12 hours. Subsequently, the sample was inserted in the main AFM chamber, and then annealed *in-situ* at ~200° C for ~1 hour to desorb surface contaminants, after which the sample was left in the chamber for 3-5 hours to equilibrate with the chamber environment. The base pressure of the main chamber was maintained at ~1×10^{-9} Torr. A single crystal Si contact-mode AFM cantilever probe with an integrated tip (CSC 38, Mikromasch Inc.) terminated by its native oxide was used throughout the experiments. The cantilevers were calibrated in the manner discussed in Section 6.2.1.2. Error bars given in the friction force represent the standard deviation in the calculated mean. All data were acquired at a nominal applied load of ~0 nN in the presence of adhesion which is discussed below.

The sample temperature was varied by heating or cooling the sample and the stage that holds it. The temperature was measured from a K-type thermocouple that was mounted directly underneath the sample. Although the AFM tip temperature was not directly varied, according to earlier studies one can assume that the tip, given its small thermal mass, will quickly reach a steady state at a temperature close to that of the sample through radiative and conductive heat transfer [5, 11]. Due to the long thermal time constant (in the order of tens of minutes) associated with the large sample holder and the bulk sample, for elevated temperatures, the temperature was ramped up from RT with an increment of ~30 K until reaching ~480 K. For low temperatures, it was cooled from RT in decrements of ~10 K until reaching the minimum temperature achievable with liquid nitrogen, corresponding to approximately 115 K. Since each scan took

approximately five minutes to complete, a small thermal fluctuation in the sample (approximately 2-3 K) was inevitable during the measurement. In between each friction scan at a given temperature, pull-off forces were also measured.

6.3.2: MD Simulations Protocol

Complementary simulations were performed by the Martini group at the University of California Merced. The simulation model consists of an apex of a diamond AFM tip with hydrogen termination scanning over a MoS_2(0001) surface. The MoS_2 substrate was modeled as a two-layer thick system with lateral dimensions of 18×16 nm^2 (length × width). The tip had a spherical shape with a radius of 2.5 nm. The topmost atoms in the tip are treated as a rigid body subject to a 0 nN external normal load, and connected by a harmonic spring to a support that moves laterally at a constant speed. A Langevin thermostat applied to the free atoms maintained the desired temperature. In all simulations, the inter-atomic interactions between the tip and hydrogen are described via the AIREBO potential [59], the interactions within the substrate are described via the REBO potential [60], and finally the long range interactions between tip and substrate are modeled using the LJ potential. All simulations are performed using LAMMPS simulation software [41].

6.3.3: Results and Discussion

Figure 6.12 shows the pull-off force measured over a range of sample temperatures. The mean pull-off force was ~7.3±1.8 nN, and a nearly constant trend was observed as a function of temperature, consistent with the Zhao *et al.*'s results for Si_3N_4

tips in contact with both HOPG and MoS_2 [11, 12]. Importantly, this suggests that surface contaminants, whose population on the surface of either the substrate or the tip can vary strongly as a function of temperature, are not present in an amount that alters adhesion.

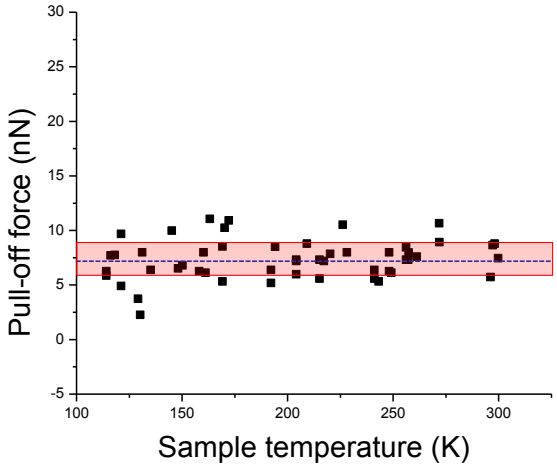

Figure 6.12: Pull-off force acquired as a function of sample temperature, ranging from ~115 – 300 K. A systematic variation of the pull-off force with temperature was not observed. The blue dash line represents the mean value (~7.3 nN) of the data set and the red box indicates the range of the standard deviation of the mean.

Figure 6.13 (a) and (b) show representative lateral force images acquired during friction measurements at T = 290 K and T = 391 K, respectively. A clear stick-slip pattern with the periodicity of the MoS_2(0001) surface lattice was observed near RT. However, as the temperature was increased, the periodicity of stick-slip pattern changed drastically, resulting in a much shorter periodicity (a factor of 2-3) compared to the pattern obtained at RT. While this effect could be attributed to thermal fluctuation, more systemic study is needed to uncover the mechanism. It was once again recovered when the temperature was

lowered back to near RT. Figure 6.13 (c) shows the friction force *vs.* sample temperature acquired at scanning speed of ~17 nm/s. A clear decreasing trend can be observed as temperature increased from 115 – 300K, after which the friction force was extremely low (0.21 ± 0.11 nN averaged over the temperature range of 300-480 K). Given that adhesion was temperature-independent and the friction forces reproducible when the temperature was brought back to RT (the order of temperature variation was RT to cryogenic temperatures and back to RT), a change in the tip shape or chemistry can be ruled out as a possible mechanism for the change in friction. Note that above RT, the error bars are smaller than the size of the data point. However, at cryogenic temperatures, the size of the error bars increase significantly as a result of more tilted friction loops due to the increase of friction.

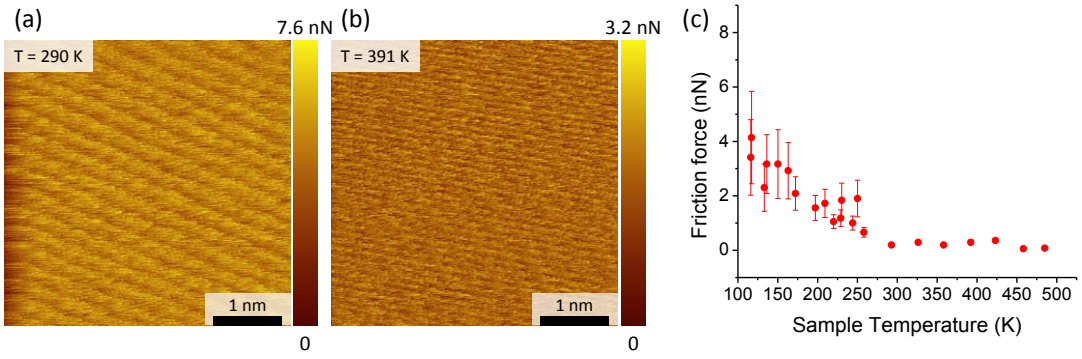

Figure 6.13: Stick-slip friction is clearly observed for scans performed near RT (a), however, as the temperatures increases (b), the pattern significantly decreased compared the one obtained at RT shown in (a). These images were used for calculating friction forces. (c) Friction *vs.* sample temperature varied from ~115 – 480 K, a strong decrease in friction was observed, data acquired at a 17 nm/s scan speed.

Next, the scan speed was varied across three different scan speeds, 17 nm/s, 34 nm/s, and 67 nm/s. The results are plotted together allowing us to better compare the effect of speed across this range of temperatures. Figure 6.14 (a) shows that, for all three speeds, friction dropped rapidly as a function of temperature, as predicted by thermolubricity. Above RT, friction remained fairly insensitive to temperature. Note here again that the sequence of temperature variation was RT to high temperature, then cooled down to RT, then from RT to cryogenic temperatures and back to RT. Figure 6.14 (a) inset plots friction *vs.* temperatures from ~115-180 K, and shows that, in addition to the decrease of friction with increasing temperature, the difference between friction forces as a function of speed increases with a decreasing temperature. This is roughly indicated by the straight lines, which are drawn simply to indicate the trend and are not fits to any model. More specifically, the absolute slope of the straight lines increases with decreasing temperatures, indicating that at low temperatures, friction is more sensitive to speeds than above ~180 K. This speed-dependent friction at a particular temperature has not been reported yet in the literature.

MD simulations were performed by closely matching the experimental parameters as described above. These results are plotted in Figure 6.14 (b). A decreasing trend in friction force as a function of temperature is observed, although this trend is less pronounced in comparison to the experiments. This can be explained by the differences in contact size, tip material, and scanning speeds. Additionally, a speed dependence of friction can also be observed from the simulations, as shown in Figure 6.14 (b) inset. However, the trend shows that the speed dependence of friction changes modestly due to the temperature. This trend is significantly less strong compared to the trend observed in

the present experiments and also to the results reported by Perez *et al.*'s from their MD study on Cu/Cu contact [54]. The cause of the disagreement could be related to the exact details of the simulation and the difference in materials studied by Perez *et al*. More studies are required to investigate this discrepancy.

Currently no experimental data is available yet below ~115 K in this study. According to a recent review paper by Krylov and Frenken [18], as temperature approaches to the absolute zero, it is expected that friction will approach a constant maximum force regardless of the scanning speed. This prediction is also consistent with the PTT model, suggesting that at 0 K, friction enters an athermal regime where the maximum friction force is related to the F_c.

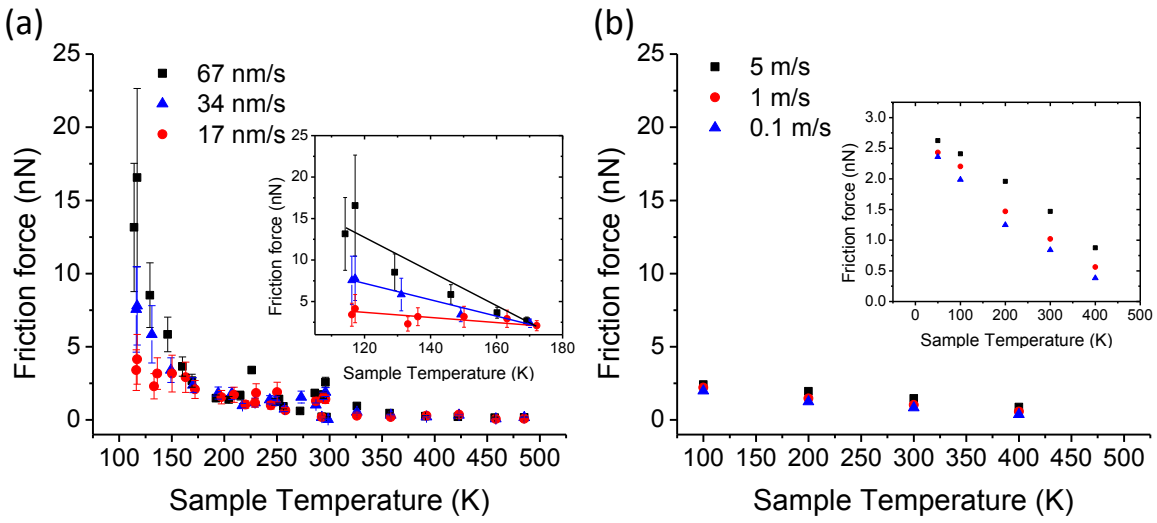

Figure 6.14: (a) Friction *vs.* temperature data acquired at three different speeds. For all three speeds, friction drops rapidly as a function of temperature up to RT, at which point friction remains fairly insensitive to temperature. Inset: At cryogenic temperatures, a trend of speed-dependent friction at a particular temperature is visible, indicating that at those temperatures, friction is more sensitive to speeds than above ~180 K. Straight lines are drawn simply to indicate the trend. (b) MD simulation results from studies at a comparable temperature range after closely matching the test parameters, plotted for the same axis ranges as (a). Similar friction behavior is observed, although the dependence is far less strong compared to the experiments. The inset shows that the friction forces are also slightly affected by the scanning speed, with higher scanning speeds leading to higher friction, as seen previously for studies at room temperature.

In our experiments, adhesion and friction were measured at a sample temperature between ~115 and ~480 K. While no significant variation in adhesion was observed as a function of sample temperature, friction exhibited a strong dependence on temperature. The friction dependence is qualitatively consistent with the effect of thermolubricity. A friction peak at cryogenic temperatures was absent, in contrast with Schirmeisen *et al.*'s

report for a Si/Si interface [5]. Since the peak was related to bond formation and breakage between the tip and sample, and thus highly dependent on the material properties of the two, it is possible that for Si/MoS_2 interface this peak is located at below ~115 K, or is even absent. Additionally, comparing to Zhao *et al*., [12], the rapid increase of friction as the temperature is reduced occurs at ~120 K as opposed to ~220 K in Zhao *et al.* [12]. This could also be rationalized by the fact that the tip material, Si_3N_4, is different in Zhao's experiment than silicon which is used here. Further experiments at lower temperatures are necessary to fully understand the origins of this behavior. Finally, the observed speed dependence of friction was also in accordance with Sang's calculations for friction as a function of temperature and speed [8].

6.4: Summary

In the first part of the study, the speed dependence of atomic friction between AFM tips and atomically-flat gold surfaces was studied using matched AFM experiments and MD simulations. For the first time, AFM experiments and MD simulation results were reported with an overlapping range of scanning speeds for the same material system and with optimally matched conditions. Despite the efforts to match conditions, there remained a discrepancy between the measured and modeled friction force. This discrepancy was explored using the PTT model to fit the experimental and simulation data separately. This analysis suggested that the difference in the magnitude of the friction from experiment and simulation may originate from the attempt frequency and the mean athermal friction force. These parameters were associated with reasonable differences in experimental and simulation contact area and tip effective mass.

Furthermore, the low speed friction plateau observed only in the experiment was explained in terms of system vibrations and instrument noise. These finding suggested that some or all of these factors may still preclude direct matching of experimentally-measured and simulation-predicted atomic-scale friction. Further study is needed to isolate the role of each factor and then potentially address the issue in simulations. However, awareness of the limitations of atomistic simulations to fully or accurately capture the contact area, tip effective mass, or instrument noise in an AFM experiment helps us better understand the predictions of such models and in turn use the information they provide to complement measurements and ultimately fundamentally understand atomic-scale friction.

Friction between a Si tip (with native oxide) and a MoS_2 sample were also performed at various temperatures ranging from ~115-480 K. For adhesion, no temperature dependence was observed, consistent with prior reports. However, friction experiments showed a strong temperature effect that is consistent with the concept of thermolubricity. Specifically, starting from cryogenic temperatures (~115 K), friction initially had fairly large forces and was quickly reduced as temperature increases. Beyond RT and up to ~480 K, friction was almost insensitive to temperature. Additionally, from ~115 K to ~180 K, speed-dependent friction at a particular temperature was observed as a function of speed: for the same temperature, friction force was increased at higher scanning speed than at lower speeds, indicating that at the cryogenic temperatures, speed has a more pronounced effect on friction, as also predicted by the PTT model. A similar trend was observed in the MD simulations, although the strength of the temperature dependence was less strong in comparison to the experiments, which could be related to

the various differences in test parameters. Lastly, speed-dependent friction at a particular temperature was also observed from the simulations; however, currently disagreement exists between the trends in MD in comparison to the AFM. More studies are required to investigate these discrepancies.

In summary, we observed that both speed and temperature have a significant effect on atomic-scale friction, and that both parameters are related, as predicted by the PTT model. For the first part of the study, the speed gap between experiments and simulation was closed by a coordinated approach involving increasing the scanning speed in AFM and slowing down the scan speed in MD simulations. A friction plateau is observed at an ultra-high scanning speed, as predicted by the PTT model. However, such a trend was not observed in the closely matched MD simulations. Additional analysis suggested that this friction plateau could be induced by the larger inertia in the experiments, or by thermal or athermal noise of the AFM which could not be captured by the present simulations. For the temperature dependence study, AFM friction tests were performed as a function of temperature and a strong decrease of friction with increasing temperature was observed, in accordance with the PTT model and more recently also predicted by the thermolubricity effect. In short, both studies suggested that the interfacial shear strength can be well controlled and predicted by altering the scanning speed and the system temperature, providing pathways to tailor frictional properties of interfaces.

6.5: References

1. X.-Z. Liu, Z. Ye, Y. Dong, P. Egberts, R.W. Carpick, and A. Martini, Dynamics of atomic stick-slip friction examined with atomic force microscopy and atomistic simulations at overlapping speeds. *Physical Review Letters* **2015**, 114(14), 146102.
2. E. Gnecco, R. Bennewitz, T. Gyalog, C. Loppacher, M. Bammerlin, E. Meyer, and H. Güntherodt, Velocity dependence of atomic friction. *Physical Review Letters* **2000**, 84(6), 1172-1175.
3. Q. Li, Y. Dong, D. Perez, A. Martini, and R.W. Carpick, Speed dependence of atomic stick-slip friction in optimally matched experiments and molecular dynamics simulations. *Physical Review Letters* **2011**, 106(12), 126101.
4. E. Riedo, E. Gnecco, R. Bennewitz, E. Meyer, and H. Brune, Interaction potential and hopping dynamics governing sliding friction. *Physical Review Letters* **2003**, 91(8), 84502.
5. A. Schirmeisen, L. Jansen, H. Hölscher, and H. Fuchs, Temperature dependence of point contact friction on silicon. *Applied Physics Letters* **2006**, 88, 123108.
6. J. Chen, I. Ratera, J. Park, and M. Salmeron, Velocity dependence of friction and hydrogen bonding effects. *Physical Review Letters* **2006**, 96(23), 236102.
7. N.S. Tambe and B. Bhushan, A new atomic force microscopy based technique for studying nanoscale friction at high sliding velocities. *Journal of Physics D: Applied Physics* **2005**, 38(5), 764-773.
8. Y. Sang, M. Dubé, and M. Grant, Thermal effects on atomic friction. *Physical Review Letters* **2001**, 87(17), 174301.
9. O. Zwörner, H. Hölscher, U. Schwarz, and R. Wiesendanger, The velocity dependence of frictional forces in point-contact friction. *Applied Physics A: Materials Science & Processing* **1998**, 66, S263-S267.
10. S.Y. Krylov, K.B. Jinesh, H. Valk, M. Dienwiebel, and J.W.M. Frenken, Thermally induced suppression of friction at the atomic scale. *Physical Review E* **2005**, 71(6), 065101.
11. X. Zhao, M. Hamilton, W.G. Sawyer, and S.S. Perry, Thermally activated friction. *Tribology Letters* **2007**, 27(1), 113-117.

12. X. Zhao, S.R. Phillpot, W.G. Sawyer, S.B. Sinnott, and S.S. Perry, Transition from thermal to athermal friction under cryogenic conditions. *Physical Review Letters* **2009**, 102(18), 186102.
13. K.B. Jinesh, S.Y. Krylov, H. Valk, M. Dienwiebel, and J.W.M. Frenken, Thermolubricity in atomic-scale friction. *Physical Review B* **2008**, 78(15), 155440.
14. L. Jansen, H. Hölscher, H. Fuchs, and A. Schirmeisen, Temperature dependence of atomic-scale stick-slip friction. *Physical Review Letters* **2010**, 104(25), 256101.
15. I. Barel, M. Urbakh, L. Jansen, and A. Schirmeisen, Multibond dynamics of nanoscale friction: The role of temperature. *Physical Review Letters* **2010**, 104(6), 066104.
16. T. Bouhacina, J.P. Aimé, S. Gauthier, D. Michel, and V. Heroguez, Tribological behavior of a polymer grafted on silanized silica probed with a nanotip. *Physical Review B* **1997**, 56(12), 7694-7703.
17. A. Socoliuc, E. Gnecco, S. Maier, O. Pfeiffer, A. Baratoff, R. Bennewitz, and E. Meyer, Atomic-scale control of friction by actuation of nanometer-sized contacts. *Science* **2006**, 313(5784), 207-10.
18. S.Y. Krylov and J.W.M. Frenken, The physics of atomic-scale friction: Basic considerations and open questions. *Physica Status Solidi (b)* **2014**, 251(4), 711-736.
19. S. Morita, S. Fujisawa, and Y. Sugawara, Spatially quantized friction with a lattice periodicity. *Surface Science Reports* **1996**, 23(1), 1-41.
20. C.M. Mate, G.M. McClelland, R. Erlandsson, and S. Chiang, Atomic-scale friction of a tungsten tip on a graphite surface. *Physical Review Letters* **1987**, 59(17), 1942-1945.
21. L. Prandtl, Ein Gedankenmodell zur kinetischen Theorie der festen Körper. *Zeitschrift für Angewandte Mathematik und Mechanik* **1928**, 8(2), 85-106.
22. G.A. Tomlinson, A molecular theory of friction. *Philosophical Magazine* **1929**, 7(46), 905-939.
23. S. Medyanik, W. Liu, I.-H. Sung, and R.W. Carpick, Predictions and observations of multiple slip modes in atomic-scale friction. *Physical Review Letters* **2006**, 97(13), 136106.
24. R. Roth, T. Glatzel, P. Steiner, E. Gnecco, A. Baratoff, and E. Meyer, Multiple slips in atomic-scale friction: An indicator for the lateral contact damping. *Tribology Letters* **2010**, 39(1), 63-69.

25. Y. Dong, Q. Li, and A. Martini, Molecular dynamics simulation of atomic friction: A review and guide. *Journal of Vacuum Science & Technology A: Vacuum, Surfaces, and Films* **2013**, 31(3), 030801.
26. I. Szlufarska, M. Chandross, and R.W. Carpick, Recent advances in single-asperity nanotribology. *Journal of Physics D: Applied Physics* **2008**, 41(12), 123001.
27. B. Bhushan, Nanotribology and nanomechanics of MEMS/NEMS and BioMEMS/BioNEMS materials and devices. *Microelectronic Engineering* **2007**, 84(3), 387-412.
28. C.M. Mate, *Tribology on the Small Scale: A Bottom Up Approach to Friction, Lubrication, and Wear*; Oxford University Press: Oxford, UK, 2008.
29. C. Nogues and M. Wanunu, A rapid approach to reproducible, atomically flat gold films on mica. *Surface Science* **2004**, 573(3), 383-389.
30. E. Meyer, H.J. Hug, and R. Bennewitz, *Scanning Probe Microscopy: The Lab on a Tip*; Springer Verlag & Business Media: Heidelberg, 2004.
31. R.W. Carpick, D.F. Ogletree, and M. Salmeron, A general equation for fitting contact area and friction vs load measurements. *Journal of Colloid and Interface Science* **1999**, 211(2), 395-400.
32. B. Derjaguin, V. Müller, and Y.P. Toporov, Effect of contact deformations on the adhesion of particles. *Journal of Colloid and Interface Science* **1975**, 53(2), 314-326.
33. K.L. Johnson, K. Kendall, and A.D. Roberts, Surface energy and the contact of elastic solids. *Proceedings of the Royal Society of London A* **1971**, 324(1558), 301-313.
34. D. Grierson, E. Flater, and R. Carpick, Accounting for the JKR-DMT transition in adhesion and friction measurements with atomic force microscopy. *Journal of Adhesion Science and Technology*, *19* **2005**, 3(5), 291-311.
35. J.D. Kiely and J.E. Houston, Nanomechanical properties of Au (111), (001), and (110) surfaces. *Physical Review B* **1998**, 57(19), 12588-12594.
36. C.-L. Dai and Y.-M. Chang, A resonant method for determining mechanical properties of Si3N4 and SiO2 thin films. *Materials Letters* **2007**, 61(14-15), 3089-3092.
37. M.J. Brukman and R.W. Carpick, Vibrations of the “beetle” scanning probe microscope: Identification of a new mode, generalized analysis, and characterization methodology. *Review of Scientific Instruments* **2006**, 77(3), 033706.
38. A.F. Voter, Parallel replica method for dynamics of infrequent events. *Physical Review B* **1998**, 57(22), R13985-R13988.

39. J. Tersoff, Empirical interatomic potential for silicon with improved elastic properties. *Physical Review B* **1988**, 38(14), 9902-9905.
40. M.S. Daw and M.I. Baskes, Semiempirical, quantum mechanical calculation of hydrogen embrittlement in metals. *Physical Review Letters* **1983**, 50(17), 1285-1288.
41. M.S. Daw and M.I. Baskes, Embedded-atom method: Derivation and application to impurities, surfaces, and other defects in metals. *Physical Review B* **1984**, 29(12), 6443-6453.
42. U. Harten, A. Lahee, J. Toennies, and C. Wöll, Observation of a soliton reconstruction of Au(111) by high-resolution helium-atom diffraction. *Physical Review Letters* **1985**, 54(24), 2619-2622.
43. S. Narasimhan and D. Vanderbilt, Elastic stress domains and the herringbone reconstruction on Au(111). *Physical Review Letters* **1992**, 69(10), 1564-1567.
44. Q. Li, Y. Dong, A. Martini, and R.W. Carpick, Atomic friction modulation on the reconstructed Au (111) surface. *Tribology Letters* **2011**, 369.
45. H.S. Khare and D.L. Burris, The extended wedge method: Atomic force microscope friction calibration for improved tolerance to instrument misalignments, tip offset, and blunt probes. *Review of Scientific Instruments* **2013**, 84(5), 055108.
46. M. Enachescu, R.J.A. van den Oetelaar, R.W. Carpick, D.F. Ogletree, C.F.J. Flipse, and M. Salmeron, Observation of proportionality between friction and contact area at the nanometer scale. *Tribology Letters* **1999**, 7(2-3), 73-78.
47. M.A. Lantz, S.J. O'Shea, M.E. Welland, and K.L. Johnson, Atomic-force-microscope study of contact area and friction on NbSe_{2}. *Physical Review B* **1997**, 55(16), 10776-10785.
48. Y. Dong, H. Gao, A. Martini, and P. Egberts, Reinterpretation of velocity-dependent atomic friction: Influence of the inherent instrumental noise in friction force microscopes. *Physical Review E* **2014**, 90(1), 012125.
49. Y. Mo, K.T. Turner, and I. Szlufarska, Friction laws at the nanoscale. *Nature* **2009**, 457(7233), 1116-9.
50. B. Luan and M.O. Robbins, The breakdown of continuum models for mechanical contacts. *Nature* **2005**, 435(7044), 929-932.
51. D.R. Lide, *CRC Handbook of Chemistry and Physics*; CRC Press, Boca Raton, FL: 2004.
52. T.D.B. Jacobs and R.W. Carpick, Nanoscale wear as a stress-assisted chemical reaction. *Nature Nanotechnology* **2013**, 8(2), 108-112.

53. A. Labuda, M. Lysy, W. Paul, Y. Miyahara, P. Grütter, R. Bennewitz, and M. Sutton, Stochastic noise in atomic force microscopy. *Physical Review E* **2012**, 86(3), 031104.
54. D. Perez, Y. Dong, A. Martini, and A.F. Voter, Rate theory description of atomic stick-slip friction. *Physical Review B* **2010**, 81(24), 245415.
55. J.L. Hutter and J. Bechhoefer, Calibration of atomic force microscope tips. *Review of Scientific Instruments* **1993**, 64, 1868.
56. S. Tung and M. McMillan, Automotive tribology overview of current advances and challenges for the future. *Tribology International* **2004**, 37(7), 517-536.
57. D.O. Moumakwa and K. Marcus, Tribology in coal-fired power plants. *Tribology International* **2005**, 38(9), 805-811.
58. M.H. Kryder, E.C. Gage, T.W. McDaniel, W.A. Challener, R.E. Rottmayer, J. Ganping, Y.-T. Hsia, and M.F. Erden, Heat assisted magnetic recording. *Proceedings of the IEEE* **2008**, 96(11), 1810-1835.
59. S.J. Stuart, A.B. Tutein, and J.A. Harrison, A reactive potential for hydrocarbons with intermolecular interactions. *The Journal of chemical physics* **2000**, 112(14), 6472-6486.
60. J.A. Harrison, C.T. White, R.J. Colton, and D.W. Brenner, Molecular-dynamics simulations of atomic-scale friction of diamond surfaces. *Physical Review B* **1992**, 46, 9700.

Chapter 7: Concluding Remarks and Future Work

The majority of the content of this thesis is a result of the research conducted during my Ph.D. studies and has already been published in peer-reviewed manuscripts [1-3]. However, there are open questions and future research directions, which will be outlined in this Chapter. This Chapter consists of four sections; the first three will summarize and discuss the conclusions of studies of the adhesion properties of graphene (Chapter 4), of the friction properties of fluorinated graphene (Chapter 5), and of thermally-activated friction processes (Chapter 6). In each section, following summaries and conclusions, open questions will be outlined, and planned experiments and future work will be discussed. Finally, an overall outlook will be provided covering all the work presented.

7.1: Adhesion Properties of Graphene and Other 2-D Films

Adhesion properties of graphene and graphite were investigated with AFM and FD spectroscopy. For aged graphene, a sliding-history dependence of adhesion was found, *i.e.*, upon exposure to dry nitrogen or ambient environment, the pull-off force is transiently increased after the tip has pre-slid over the surface[1]. This effect is also observed on aged graphite, and on aged graphene, provided it is loosely adhered to its underlying substrate, such as SiO_2. These findings indicate that aging of graphite and graphene films results in the strengthening of adhesive interaction between a silicon tip and the topmost layer of the sample. This effect is also seen to occur in closely matched FEM simulations. Based on results from the literature [4], the aging process involves oxidation of the top-layer of graphene, causing it to interact more strongly with the native

oxide of the silicon AFM tip. When the interaction between the tip and the topmost layer of graphene/graphite is further strengthened by sliding, the tip-graphene interfacial configuration is substantially altered such that topmost layer locally delaminates under tensile loading, leading to an enhanced adhesion force upon pulling off the AFM tip. Subsequent pull-off measurements show a rather steady value. The effect is suppressed when graphene is strongly adhered, such as on muscovite mica, due to the strong interaction energy between the mica and the graphene, preventing local delamination of the graphene from the mica substrate. The observation of a sliding history-dependent pull-off force demonstrates the importance of the three interfaces (tip/sample; sample/graphene; graphene/tip) when measuring adhesion forces on 2-D materials. It also shows that adhesion forces on graphene-terminated surfaces that will be exposed to oxygen-containing atmospheres can be minimized by using one or at most a few layers that are strongly adhered to their substrate. This study, combined with the results thickness-dependence of friction as published in Ref. [5], demonstrates that contact area is strongly affected by the number of layers of 2-D films, as evidenced by the puckering effect for friction and by enhanced adhesion forces upon pre-sliding of aged graphene surfaces. Therefore, arranging the number of layers for 2-D films offers a pathway to alter the contact area during sliding while the interfacial shear strength remains constant.

While the proposed mechanism can explain our experimental observations, there are a number of unknowns and unresolved issues. These open questions need to be answered through further studies to more fully understand the governing mechanisms. In the following, a list of recommended studies is presented to extend this work.

1. Uncovering atomistic mechanisms of this observed effect is challenging as it is difficult to model surfaces that are less than ideal, for example, oxidized samples. The next step in this project would be to carry out similar pre-sliding experiments in UHV on clean graphene surfaces. Under these vacuum conditions, the surfaces will not be oxidized if they are prepared (*i.e.,* cleaved) *in situ*; or if they can be treated in such a way that they will not be oxidized, so that pristine surface chemistry can be maintained. In addition, the ability to reverse the oxidation process, for example by *in situ* vacuum annealing to substantially reduce or eliminate any oxidization on the sample, would help to verify the proposed model. Given the inherent environmental similarity of UHV AFM experiments and MD simulations, performing tests inside the UHV AFM provides one with the ability to match experimental and simulation conditions, allowing reliable comparisons between the two.

2. We observed that for direct pull-off measurements, pull-off forces remain constant, and the proposed mechanism is that adhesion forces are primarily dominated by the surface interactions between the AFM tip and the graphene surface of the top layer. However, the detailed atomistic mechanism and how that picture might fit in the continuum mechanics remain presently unclear.

3. It was also found that that if one imposes a strong adhesive interaction between a graphene sample and the substrate, for example by examining graphene exfoliated onto freshly-cleaved muscovite mica, the transient increase of adhesion force after scanning is eliminated. Indeed, mica is known for its high surface energy and thus is capable of strongly adhering to single or possibly few layer graphene. Indeed, it is known to prevent graphene from puckering during sliding [5]. The fact that the transient adhesion effect

was suppressed for up to 3 layers of graphene suggests that the interaction between graphene and muscovite mica extends at least 1 nm (approximately the thickness of 3 graphene layers). Recently, Tsoi *et al.* reported that few-layer graphene is able to screen van der Waals forces from an underlying SiO_2 substrate [6]. This seems somewhat contradictory to our results, since we observed an absence of sliding history-dependent of adhesion on tri-layer graphene deposited on muscovite mica. Therefore, a systematic experiment (and also combined with simulations) to study the pre-sliding effect as a function of number of graphene layers deposited on mica is warranted.

4. As shown by Lee *et al.*, layer-dependent friction is observed not only for graphene but also for three other exfoliated 2-D films: MoS_2, BN, and $NbSe_2$ [5]. Studying the pre-sliding adhesion experiments on these other 2-D films will elucidate the hypothesis that the adhesion enhancement effect is more general.

5. As an extension of the experiment on layer-dependent friction, it would be valuable to investigate and quantify the effect of normal load, temperature, and scanning speed on the frictional behavior of graphene and other 2-D materials, which again will provide insight into the mechanism of the puckering effect, and possibly uncover other mechanisms controlling atomic friction. Specifically, recent MD simulations on friction as a function of load showed a monotonically increasing trend for supported graphene, and on suspended graphene friction is observed to first increase and then decrease with increasing load [7].

7.2: Friction Properties of Fluorinated Graphene and the Influence of Other Chemical Functionalization

In the second study, it was observed that friction on fluorinated graphene is strongly affected by the degree of fluorination, which is controlled by the exposure time of the graphene film to the XeF_2 gas. With increasing fluorination time, a corresponding friction ratio of >11x higher than on pristine graphene was observed. This strong dependence is attributed to the fact that attachment of fluorine atoms to the graphene scaffold greatly enhances the local energy barrier for sliding and thereby significantly alters the energy landscape experienced by the tip apex. These results provide new insights into the atomic-scale effects of functionalization on friction properties of graphene; and in addition, they suggest an approach to sensitively probe the local chemistry and structure of functionalized graphene. Collectively, these results provide important new insights into the atomic-scale effects of functionalization on graphene, showing how the structure, chemistry, electronic behavior, and frictional behavior are coupled together. They also demonstrate how atomic-scale friction is a sensitive probe of the local chemistry and structure of functionalized graphene. Lastly, it is demonstrated that surface functionalization offers a way to tailor the potential energy landscape of thin films, which in turn allows friction to be tuned according to specific needs in applications.

There still exist several open questions, which are desirable to address through experiments and simulations. Below, a list of recommended studies to extend this work is presented.

1. Present studies only focused on systems of single layer graphene and FG. It remains unclear how friction on multi-layer FG and graphene behaves at the highest degree of fluorination, and as a function of the number of layers of graphene and FG. For example, it would be interesting to see if the layer-dependent friction observed on graphene [ref] extends to its chemically modified relatives. The aim then would be to gain further insight into the mechanism of the influence of fluorination and the degree of fluorination on friction as a function of the film thickness.

2. From the MD results on ordered C_2F, we found that the potential energy surface (PES) experienced by the tip apex is decreased in corrugation compared to that of C_4F, although the values for both the PES and friction coefficient are still much greater than those for pristine graphene. We explained this by hypothesizing that greater coverage of fluorine atoms is approaching the limit where a dense fluorine layer is covers the graphene, therefore maximally screening the carbon energy landscape, resulting in a flatter PES. However, more studied should be devoted to fully understand the mechanism. Additionally, Dong *et al.* predicted that friction between a diamond tip and hydrogenated graphene will initially increase with increasing degree of hydrogenation, and then decrease again when approaching a fully hydrogenated state [8]. Given that there are similarities between FG and hydrogenated graphene, it is worth investigating whether this prediction also holds for fully fluorinated graphene.

3. According to our proposed mechanism, the attachment of fluorine atoms to graphene greatly increases the local energy barrier for sliding and alters the PES experienced by the tip apex. For the particular system that examined, the specific distribution fluorine is unknown, although fluorination occurs nominally on the top

surface only. However, at extended fluorination times, it is possible that fluorine also penetrates to the bottom surface. Therefore, it remains extremely interesting to intentionally fluorinate both top and bottom surface and compare friction properties to those of top side fluorinated graphene.

7.3: Thermally-Activated of Atomic-Scale Friction

In the study of the speed dependence of atomic friction, our collaborators were able to significantly reduce MD simulation scanning speeds by using accelerated MD, and we were able to significantly increase experimental scanning speeds by improving the AFM apparatus, while resolving stick-slip behavior in both. This led, for the first time, to obtaining experimental and simulation results with an overlapping range of scanning speeds. Other parameters, namely environment (vacuum), materials (a SiO_2 tip on a gold sample), contact area, temperature, normal and lateral stiffnesses, and load were also matched as closely as possible. Using the PTT model to compare and contrast experiment and simulation data, we made the first experimental observation of the saturation of the friction force above a critical scanning speed, as predicted by the PTT model. However, friction in experiments was larger than in simulations. PTT energetic parameters for the two were comparable, with minor differences attributable to the contact area's influence on the barrier to slip. Recognizing that the attempt frequency may be determined by thermal vibrations of the larger AFM tip mass or instrument noise allows the discrepancy to be fully resolved. Thus, atomic stick-slip friction is well described by the PTT model if sources of slip-assisting energy are accounted for.

In the study on temperature dependence of atomic friction, the influence of temperature on friction between a Si AFM tip (with native oxide) and MoS_2 samples was investigated using both AFM experiments and MD simulations. From the preliminary AFM results, elevated sample temperatures were achieved by resistive heating of the sample until ~480 K; for low temperatures, liquid nitrogen was used in the low temperature cryostat to cool down the sample temperature until ~110 K. In MD, the test parameters were matched as closely as possible, including the materials, environment (vacuum), temperatures, materials, contact area, normal and lateral stiffnesses, and load. Our preliminary data revealed that, in general agreement with the PTT model and with the concept of thermolubricity, friction decreases significantly as the system temperature increases. This phenomenon can be understood by considering that tip atoms, when stuck, are sitting in a minimum of the interfacial potential energy. The higher the temperature, the more thermal energy will assist the tip to transit to the next energy minimum, resulting in lower static friction. Conversely, at lower temperatures, there are fewer thermal excitations to assist the tip to overcome an energy barrier, thus increasing friction.

While the same trend was observed in the MD, the temperature dependence was much less strong than what was observed in experiments. Additionally, as shown in Section 6.3.3, under cryogenic temperatures in AFM, speed-dependent friction at a particular temperature was also observed. Specifically, for the speed range examined (from 17 nm/s to 67 nm/s), in the temperature range of ~115 K to ~170 K, friction was more sensitive to the scanning speed at a lower temperature than at a higher temperature. Although friction did vary as a function of temperature, it was found that adhesion did

not change across the temperature range between ~115 K to ~300 K. Therefore, adhesion is not the cause of the temperature dependence of friction. In summary, from both studies, we concluded that both scanning speed and temperature will affect friction and thus are possible ways to alter the interfacial shear strength. In particular, temperature plays a significant role in determining the magnitude of static friction.

Despite these findings which strongly support the hypothesis that atomic stick-slip friction is a thermally activated process, there are remaining open questions and more areas that worth exploring. Below is a partial list.

1. To date, much effort has been devoted to explore scanning speed and temperature, although the latter is preliminary, including the studies described in Chapter 6 of this thesis. However, the correlation between the temperature and the scanning speed would become more clear if the influence of both was examined in the same experiment, *i.e.*, changing the scanning speed across ~6 decades of speeds at different temperatures. Specifically, one could utilize the custom-designed high-speed shear piezo scanner from Chapter 6 combined with the full capabilities of the liquid helium cryostat. Obtaining friction *vs*. speed data sets at various temperatures would allow us to explore each of the fitting parameters in the PTT models as a function of time. First, although β in Eq. (2) in Chapter 6 is related to the shape of the potential energy corrugation (and can be extracted from the slope of the friction *vs.* speed data prior to reaching the high speed plateau), it does not explicitly depend on temperature. While this parameter has been found to be in the same order of magnitude for both SiO_2/Au and Pt/Au contacts, and good agreement was found between AFM and MD, does this mean that one can expect the slope is invariant with temperature and materials at the interface? Second, F_c was extracted as the

value at the plateau of the AFM friction data, which by itself represents attaining a high enough scanning speed that available thermal vibrations of the atoms at the end of the tip apex no longer have enough time to assist in overcoming the local interfacial potential energy barriers. According to the PTT model, this is equivalent to the friction at zero K, or the athermal regime. Will changing the system temperature shift the plateau, and if so, by what amount? Specifically, one can expect that decreasing the temperature will shift the plateau upward, since then thermal vibrations of the tip atoms will already be significantly less than at room temperature or even higher. Conversely, does higher temperatures cause a downshift of the plateau? If so, theoretically it would be possible to result in speed-invariant friction force starting from low speeds.

2. Extending the above study simultaneously varying both the scanning speed and system temperature also allows one to investigate speed-dependent friction at a particular temperature that was observed in the preliminary temperature dependence data. Specifically, at ~115 K, if varying the speed by a factor of 4 results in a difference of 3 times in friction, then changing the speed by a few orders of magnitude will drastically results in more than 10 times difference in friction. Additionally, lowering the temperature to ~40 K will only strengthen the trend of this gap, but to an extent that is not known. Lastly, the preliminary data showed that the speed dependence of friction increases with a decreasing temperature, will this mean that near zero K the friction difference will be spread maximum? However, this prediction has to contradict the PT model, which predicts that in the athermal regime the speed does not affect friction since due to the F_c asymptote. This paradox could be solved by considering Krylov and Frenken's theoretical prediction is correct that all friction forces will become a step

function at zero K [9], in other words, friction will then reach a constant value (F_c) regardless of the scanning speed. Experimentally, to fully resolve the trend near the zero K regime, one must dramatically improve the cryostat performance, which requires a significant amount of effort.

3. Extending the speed and temperature dependence studies on other materials, including graphene, will also provide insight into atomic-scale friction of 2-D materials, and prove or disprove existing literature examining temperature dependence of friction for both suspended and supported graphene [10], and the role of intrinsic wrinkles in graphene [11].

4. Finally, experiments at elevated temperatures for temperature dependence of friction can be improved by utilizing novel heated AFM probes, as first developed by Lee *et al.* [12]. Those heated AFM probes are capable of achieving localized heating at the interface, and has a few advantages over radiative heating using a tungsten filament mounted right underneath the specimen, which is the case in the present study. Currently, during scanning at elevated temperatures, thermal drift needs to be minimized by allowing sufficient time, which is on the order of tens of minutes. Despite this additional effort, the temperature fluctuation during a single scan still remains 1-2 °C. Given the small thermal mass of the heated probes, extremely short heating and cooling times (in the order of 50 μs) can be achieved, significantly shortening the time of required for reaching steady-state, thus improving the efficiency of data acquisition. Another important advantage of the heated probes is that they can operate under humid or controlled environment [13], whereas the conventional method of heating the entire

sample requires vacuum conditions in order to avoid oxidation due to heating. While the latter is beneficial for purposes of comparison to present MD studies, being able to perform temperature dependence studies at humid environment opens door to testing influences of meniscus effects [14] and adsorbates [15]. Those studies are valuable since both humidity and adsorbates are more realistic conditions under which real engineering devices operate, and therefore will improve our understanding of the role of contaminants and humidity in frictional processes.

7.4: Overall Outlook

This thesis presented three nanotribological studies investigating various ways of tuning friction, *i.e.* both *decreasing* and *increasing* it. We observed that besides varying the surface commensurability [16], surface termination [17], potential [18], and vibrating the cantilever at a certain frequency [19], temperature can also play a significant role, as predicted by thermolubricity, We also observed that besides tuning the band gap of graphene, different degrees of fluorination of graphene allows one to tune friction. Furthermore, desired friction properties can be achieved by properly choosing the thickness of graphene as a result of the puckering effect of 2-D materials. With regard to the adhesion properties of graphene, we observed that when no tip sliding has occurred, adhesion force is rather low and reproducible, suggesting that when graphene is applied as thin protective coating where no robbing contacts are involved, adhesion is less crucial. However, due to aging of graphene, enhanced adhesion cannot be ignored for sliding interfaces; therefore one must be cautious in designing graphene-based M-/NEMS by considering the influence of surface aging along with the puckering effect of 2-D

materials. Despite the abovementioned and other tremendous advancements in nanotribology over the last few decades, there is space for further explorations and improvements, including the ones listed above. Fortunately, one of the most exciting advancements that modern technologies bring us is the powerful combination of the improvement of instrumentation and the tremendously increasing computing power, enabling more precise experiments and more reliable atomistic simulations of larger systems. Ultimately, this all allows us to see a real buried interface more clearly and accurately, and to discover more fundamental physical laws of tribology.

7.5: References

1. X.-Z. Liu, Q. Li, P. Egberts, and R.W. Carpick, Nanoscale adhesive properties of graphene: The effect of sliding history. *Advanced Materials Interfaces* **2014**, 1-9.
2. Q. Li, X.Z. Liu, S.P. Kim, V.B. Shenoy, P.E. Sheehan, J.T. Robinson, and R.W. Carpick, Fluorination of graphene enhances friction due to increased corrugation. *Nano Letters* **2014**, 14(9), 5212-7.
3. X.-Z. Liu, Z. Ye, Y. Dong, P. Egberts, R.W. Carpick, and A. Martini, Dynamics of atomic stick-slip friction examined with atomic force microscopy and atomistic simulations at overlapping speeds. *Physical Review Letters* **2015**, 114(14), 146102.
4. Z. Deng, A. Smolyanitsky, Q. Li, X.Q. Feng, and R.J. Cannara, Adhesion-dependent negative friction coefficient on chemically modified graphite at the nanoscale. *Nature Materials* **2012**, 11(12), 1032-1037.
5. C. Lee, Q. Li, W. Kalb, X.-Z. Liu, H. Berger, R.W. Carpick, and J. Hone, Frictional characteristics of atomically thin sheets. *Science* **2010**, 328(5974), 76.
6. S. Tsoi, P. Dev, A.L. Friedman, R. Stine, J.T. Robinson, T.L. Reinecke, and P.E. Sheehan, van der Waals screening by single-layer graphene and molybdenum disulfide. *ACS Nano* **2014**, 8(12), 12410-12417.
7. Z. Ye and A. Martini, Atomistic simulation of the load dependence of nanoscale friction on suspended and supported graphene. *Langmuir* **2014**, 30(49), 14707-14711.

8. Y. Dong, X. Wu, and A. Martini, Atomic roughness enhanced friction on hydrogenated graphene. *Nanotechnology* **2013**, 24(37), 375701.
9. S.Y. Krylov and J.W.M. Frenken, The physics of atomic-scale friction: Basic considerations and open questions. *Physica Status Solidi (b)* **2014**, 251(4), 711-736.
10. A. Smolyanitsky, Effects of thermal rippling on the frictional properties of free-standing graphene. *RSC Advances* **2015**, 5(37), 29179-29184.
11. W. Bao, F. Miao, Z. Chen, H. Zhang, W. Jang, C. Dames, and C.N. Lau, Controlled ripple texturing of suspended graphene and ultrathin graphite membranes. *Nature Nanotechnology* **2009**, 4(9), 562-566.
12. J. Lee, T. Beechem, T.L. Wright, B.A. Nelson, S. Graham, and W.P. King, Electrical, thermal, and mechanical characterization of silicon microcantilever heaters. *Journal of Microelectromechanical Systems* **2006**, 15(6), 1644-1655.
13. C. Greiner, J.R. Felts, Z. Dai, W.P. King, and R.W. Carpick, Local nanoscale heating modulates single-asperity friction. *Nano Letters* **2010**, 10(11), 4640-5.
14. C. Greiner, J.R. Felts, Z. Dai, W.P. King, and R.W. Carpick, Controlling nanoscale friction through the competition between capillary adsorption and thermally-activated sliding. *ACS Nano* **2012**, 4305-4313.
15. I. Szlufarska, M. Chandross, and R.W. Carpick, Recent advances in single-asperity nanotribology. *Journal of Physics D: Applied Physics* **2008**, 41(12), 123001.
16. M. Dienwiebel, G. Verhoeven, N. Pradeep, J. Frenken, J. Heimberg, and H. Zandbergen, Superlubricity of graphite. *Physical Review Letters* **2004**, 92(12), 126101.
17. R.J. Cannara, M.J. Brukman, K. Cimatu, A.V. Sumant, S. Baldelli, and R.W. Carpick, Nanoscale friction varied by isotopic shifting of surface vibrational frequencies. *Science* **2007**, 318(5851), 780-3.
18. J.Y. Park, D. Ogletree, P. Thiel, and M. Salmeron, Electronic control of friction in silicon pn junctions. *Science* **2006**, 313(5784), 186.
19. A. Socoliuc, E. Gnecco, S. Maier, O. Pfeiffer, A. Baratoff, R. Bennewitz, and E. Meyer, Atomic-scale control of friction by actuation of nanometer-sized contacts. *Science* **2006**, 313(5784), 207-10.